Electrical Inversion and Characterisation Methods in Geophysics

Jonathan Howard Saunders

Department of Earth Science & Engineering,

Exhibition Road, Imperial College London,

South Kensington Campus,

London SW7 2AZ, UK

Submitted for the degree of Doctor of Philosophy

December 2004

Abstract

Four electrical methods for characterisation of fluid-bearing rock formations are presented. The electrical properties of formations are principally governed by the saturating fluid. This work therefore has application in both hydrology and the hydrocarbon industry. Modelling of the methods is achieved using a numerical, finite-element technique. A method for improving the accuracy and geophysical coherence of anisotropic resistivity inversion using seismic data is developed. Comparison is made with previous inversions of synthetic data and field data, showing the advantages of the constraints and the improved conductivity models resulting from the structurally constrained inversion. The feasibility of using permanently deployed downhole electrical sensors to monitor the advance of the water front during oil production is investigated, using a synthetic model and a reservoir model reconstructed from an outcrop analogue. Measurements are made in which the electrical potentials arise due to electrokinetic coupling, and a second experiment involving current injection is also described. It is found that both methods may be useful in monitoring the fluid distributions in the reservoir, and in forecasting breakthrough at the production well. A field case study is conducted in the East Yorkshire (UK) chalk aquifer, to measure electrokinetic potentials in the field and make an estimate of the electrokinetic coupling coefficient in this environment. In a fourth method, the propagation of seismic waves in and around a borehole due to excitation by an acoustic source, and the electrical potentials generated through electrokinetic coupling in the surrounding formation are modelled for the purpose of determining rock properties, in particular permeability. It is found that the amplitude of the Stoneley-related electric field normalised by the Stoneley-related pressure is indicative of formation permeability. Formation layering, mudcake and fractures are modelled, and a field experiment is conducted to validate the modelling.

Acknowledgements

My greatest thanks must go to my supervisors Prof. Michael Worthington, Dr Chris Pain and Dr Cassiano de Oliveira, first of all for getting me involved in this work which has absorbed me for 3 years, and second for indispensible support, advice, criticism and encouragement throughout. The work presented here owes much to their enthusiasm for geophysics and computational physics, but probably reflects only a part of what I have learned from them in these, and other fields since I was a recently-graduated astrophysicist back in November 2001.

Thanks to the many other people with whom I've worked, especially Dr Jörg Herwanger, Julian Singer and Dr Matthew Jackson of whose experience and time I've been a grateful beneficiary, and to the other members of the AMCG for being a great team, especially Gerard Gorman, 'Dr' Matthew Eaton and Adrian Umpleby for such patience with those of us still learning the intricacies of LINUX. Also Dr André Revil for valuable input on all aspects of electrokinesis, Lee Holloway, Guy Mason and all at Sondex Wireline Ltd, Prof. Tony Goddard, Simon Payne at Oxford University for his company on the field trip to Yorkshire, Dr Noelle Odling, Dr Jared West and Silke Hartmann at Leeds University for their help in carrying out and interpreting the experiments at Wilfholme Landing, Dr Insa Neuweiler and Dr Oleg Demin for lunch-time respite and coffee at the RSA, and Claud in the RSM café for selling the finest doughnuts around. My thanks also to Prof. Nafi Toksöz for kind permission to reproduce Fig. 5.3b in this thesis.

I would like to thank ABB Offshore Systems for sponsorship of the first year of this project. Sondex Wireline Ltd have funded the second portion, with financial support from the Directorate-General for Energy and Transport of the European Commission under the Growth Programme, research project EKLTOOL (Electrokinetic Logging Tool Development for Enabling more Efficient Production from Hydrocarbon-bearing Formations and Groundwater Aquifers), contract number NNE5/2001/679. My thanks to Sondex for this funding, and also for their personal interest in the project over and above the commercial viability of the methods investigated.

Finally I would like to dedicate this thesis to my beautiful wife Allison, whose love and encouragement has spurred me on through these past three years, and whose unreasonable dedication to my well-being has made me a happier and prouder person at its completion.

Contents

List of Figures

List of Tables

Chapter 1

Electrical Inversion and Characterisation Methods in Geophysics

1.1 Introduction

Electrical methods offer the geophysicist a unique set of tools for investigating the Earth. Ranging from large-scale resistivity measurements over hundreds of metres, to pore-scale measurements of excess ions on a mineral surface, the non-invasive nature of electrical surveying makes it ideal with both active experiments using injected current completed in a fraction of a second, and passive experiments in which naturally occurring electric fields are monitored for days, months or even years on end. Applications include archaeology and pollution monitoring as well as near-surface hydrology, cave and fracture detection, and hydrocarbon reservoir management. This work aims to bring electrical methods further into the mainstream field of the hydrocarbon industry and reservoir management, and to show that such techniques can lead to a better understanding of the Earth where other methods may be reaching some limit in their development.

The environmental benefits of using electrical methods for sub-surface characterisation are several. In the light of recent concern over the impact of seismic surveying on marine wildlife, the importance of using a more localised method for reservoir characterisation whenever possible is all the greater. Again in the reservoir environment, improved knowledge of the reservoir flow properties, in particular permeability, may result in fewer boreholes needing to be drilled, and can increase the efficiency of production as the hydrocarbon/water ratio in the produced fluid is increased. Such improvements will be vital in the coming decades, as restrictions on carbon pollution are increased and hydrocarbon resources further dwindle. Without these advancements the hydrocarbon industry, which will inevitably continue to underpin the global economy, will be increasingly under pressure as new, carbon-free energy technologies are developed.

1.2 Outline of thesis

In this examination of electrical methods, chapter 2 contains a discussion of the simplest form of electrical experimentation, namely measurement of resistivity. Here the technique of using seismic data to constrain anisotropic resistivity inversion is investigated, with the aim of producing an electrical model with both reduced susceptibility to non-uniqueness problems and improved geophysical credibility. The equations governing this problem and the discretisation of these equations into finite-element form are presented, followed by a description of the means by which the seismic data may be used to construct constraints for the electrical problem. A method for facilitating the calculation of appropriate constraint magnitudes for any given resistivity inversion problem is discussed. This simple procedure reduces the need for an exhaustive search for the correct values for the constraints, which may encompass many orders of magnitude. Results from inversion of synthetic and field data are given.

The properties of steady-state fluid flow in the context of hydrocarbon production are explored in chapter 3. In this chapter the concept of electrokinesis is introduced and, using a finite-element model, an investigation is made of whether or not electrokinetics and/or a current-injection resistivity method could be used as part of an 'Intelligent Well Technology' deployment. Again, the governing equations and discretisation of both the fluid dynamical and electrical equations are presented first. A passive experiment, in which streaming potentials due to fluid flow are measured, is discussed in relation to an idealised synthetic reservoir and a 'realistic' reservoir reconstructed from outcrop data. A second experiment which involves injection of current at an electrode positioned in the borehole is also described.

A field experiment at Wilfholme Landing, Yorkshire, UK is the subject of chapter 4, during which self-potentials associated with electrokinesis were recorded. This work follows on from the previous chapter, and provides an opportunity to measure electrokinetic potentials in the field, and to examine the applicability of the current theory to this environment. The site location and geology are described, and the results of the experiments presented. An interpretation of the results follows, including modelling of the experiment and a discussion of the dependence of the results on fluid conductivity and the zeta potential.

Chapters 5-8 are concerned with a more complex electrical method, that of borehole electroseismics, in which steady-state flow is replaced with low-frequency oscillations. The theory of acoustic wave propagation due to Biot (1956) is presented, the coupling between the acoustic and electrical parameters is discussed, and the discretisation of the equations and related computational issues are described. Examples showing the performance of the method are shown. In chapter 6 the viability of the method as a means for in-situ diagnosis of formation permeability in homogeneous formations is explored. Methods by which formation permeability may be inferred are described, along with some discussion of the dependence of the data on physical parameters such as the borehole radius. The necessary modelling considerations for representation of features such as formation layering, mudcake and fractures are discussed in chapter 7, along with the various

constraints that these features place on the results presented in chapter 6. The results from a field experiment and from subsequent modelling are given in chapter 8. The field site and geology, the experimental set up and the data acquisition system are described, followed by a presentation of the acoustic and electrical data recorded and an initial interpretation of the results in the light of the previous chapters. Results from modelling of the field experiment confirm that the values of parameters used in the electrical equations for modelling are appropriate, and also suggest that the formation at the site may be significantly fractured in particular zones.

Each chapter begins with a review of the relevant literature, and ends with a discussion of the findings presented and conclusions which may be drawn. Chapters 2-4 are self-contained, while in chapters 5-8 a progression is followed, from a description of the finite-element model through an increasingly complex borehole-formation model to the presentation of field data. In chapter 9 a summary of all of the findings presented in the thesis is given, and suggestions for further research are made.

Chapter 2

Constraining Structure in Electrical Resistivity Inversion

2.1 Introduction

Inversion of geophysical data is usually non-unique and ambiguous. Using a suite of different geophysical techniques and finding subsurface models compatible with data from all employed techniques reduces the ambiguity of inversion models (Jupp & Vozoff, 1975; Lines et al., 1988). Several methods for constraining inversion of a data set using information from another set have been suggested. Perhaps the most familiar technique is joint inversion, for example used by Haber & Oldenburg (1997) to invert seismic and gravity data. Musil et al. (2003) have used *a priori* information to limit the scope of their inversion results, with variable success. Structurally constrained inversions (Kaipio et al., 1999; Pinheiro et al., 1997) use constraints based on the gradient or curvature of a known data set, and it is this technique which is developed here since the correlation between seismic velocity and electrical resistivity may be positive or negative dependent on the degree of consolidation (Meju et al., 2003). In two previous papers the results of a seismic tomography study (Herwanger et al., 2004a) and an electric tomography study (Herwanger et al., 2004b) using cross-well data from the Reskajeage test site in Cornwall, SW-England, were presented. Both the seismic and electric datasets were separately inverted to obtain anisotropic velocity tomograms and anisotropic conductivity tomograms, respectively. Seismic and electric tomograms show strongly inhomogeneous distributions of their respective physical properties. Seismic velocity ranges from 3.5km/s to 6km/s and observed electric conductivity varies between 1mS/m to 3.3mS/m, corresponding to a resistivity range of 300 to 1000Ωm. Besides being strongly inhomogeneous, observed velocity and resistivity are markedly anisotropic. Seismic anisotropy (measured by Thomsen (1986)) ranges from 0 to 40% and resistivity anisotropy of up to 300% is observed.

When comparing (anisotropic) seismic and electric tomograms a broad correlation between the two images is easily identified: high velocity regions coincide with resistive bodies and regions of large seismic anisotropy also display large electric anisotropy. It is believed that seismic and electric properties correlate even better than the tomographic images suggest. This belief is based mostly on two observations. First, velocity profiles along the boreholes from VSP-measurements and downhole Wenner electric profiles show a very definite correlation of seismic and electric properties (Herwanger, 2001). Whenever a sharp change in (vertical) seismic velocity occurs, the observed electric resistivity displays a jump as well. Seismically homogeneous areas are also electrically homogeneous. The magnitude of the change is not as easily quantified or correlated. Second, some of the differences in structure between seismic and electric tomograms can be directly attributed to differences in resolution between the two methods and differences in the behaviour of the inversion process. For example, experiments on synthetic electric data have shown that resistive bodies are hard to image, since current is channelled around them, with the result that the image of the resistive bodies is too thin (e.g. Herwanger et al. (2004b)). A similar problem can occur in seismic cross-well imaging, where high-velocity zones channel seismic energy. However, experience has shown this problem to be a lot less severe in seismic tomography compared with electric tomography.

Considerable work (Herwanger et al., 2004a,b; Pain et al., 2003) with seismic and electrical inversion allows the following two conclusions. Sharp lithological interfaces are marked more crisply by seismic tomography than by electric tomography. Also, the locations of interfaces derived from seismic images correspond better with interfaces observed in the borehole than interfaces interpreted from electric images, due to physical limitations inherent in electrical imaging.

In this chapter, therefore, a methodology is presented and applied that uses the superior structural information of a known data set to inform inversion of another set, which may have poorer spatial resolution. To illustrate the method the seismic images obtained from Reskajeage are used to create better-focused electrical images. This is achieved by imposing spatially varying smoothness constraints, derived from seismics, on the inversion of the electrical data. The inversion algorithm for electric data is described in detail in Pain et al. (2003), and a description of the experiment and inversion of the field data is given in Herwanger et al. (2004b). A spatially and directionally varying operator is introduced, and it is shown that using this operator can result in improved electric inversion models.

In section 2.2 the governing equations for this method are briefly summarised and the functionals which are to be minimised are described. It is then shown how to construct the smoothness constraints (Sec. 2.3). There are two key requirements on the definition of structure. First, the directional behaviour of structure needs to be addressed properly. For example, a simple inclined boundary between two rock layers is smooth along the layer boundary and rough across the layer boundary. The result is an anisotropic structural operator. Second, even though changes in seismic and electric properties are expected to occur at the same places, the magnitude of change may not be well correlated (Zhang & Morgan, 1997). Therefore an operator is required

which allows changes at a pre-determined location but is independent of sign and magnitude at this specific location. Subsequently it is demonstrated how the magnitude of the required smoothness constraints may be determined using non-dimensional functions of the physical properties in the domain of interest. This method can reduce the need for lengthy searches for the optimum levels of structural and anisotropy constraints, and so significantly reduce the overall time taken to perform a successful inversion. In section 2.5 the performance of inversions using homogeneous smoothness constraints versus spatially varying structural constraints are compared, using synthetic data from a model built to resemble the Reskajeage model. Finally an inversion of the field data using spatially varying smoothness constraints is carried out (Sec. 2.6), again comparing these results to previous inversions (using constant smoothness constraints) of the same data.

2.2 Governing equations

In this section a summary of the most relevant equations used to solve the inverse DC-electrical problem is presented, providing a basis for the work in the rest of the chapter. For a complete description of the theory, discretisation and implementation see Pain et al. (2002), Pain et al. (2003) and Herwanger et al. (2004b).

Given a domain $\Omega \subset \Re^n$ with conductivity distribution $\boldsymbol{\sigma} = \boldsymbol{\sigma}(\mathbf{x})$, injection of a current $I_s\delta(\mathbf{x} - \mathbf{x}_s)$ at a source centred at position $\mathbf{x}_s \in \Omega$ results in a potential $\psi_s = \psi_s(\mathbf{x})$ according to:

$$\nabla.\boldsymbol{\sigma}(\mathbf{x})\nabla\psi_s = I_s\delta(\mathbf{x} - \mathbf{x}_s), \quad \mathbf{x} \in \Omega. \tag{2.1}$$

The method is fully generalised for one, two or three-dimensional problems, i.e. $n = 1, 2, 3$. In practice three dimensions are usual, although two-dimensional synthetic examples may be informative. However the description of the method is not restricted to either case at this point. The current injection experiment is generally repeated for a large number of source locations, $s \in \{1, 2, ...S\}$. A finite-element (FE) approximation $\phi_s \approx \psi_s$ is constructed by multiplying Eq. 2.1 by the FE basis functions Q_i leading to the matrix equations:

$$\mathbf{A}\boldsymbol{\Phi}_s = \mathbf{b}_s, \quad \forall s \in \{1, 2, \ldots, S\}. \tag{2.2}$$

Here the elements of the system matrix are calculated by $\mathbf{A}_{ij} = -\int_\Omega \nabla Q_i \boldsymbol{\sigma} \nabla Q_j d\mathbf{x}$, the source vector on the right hand side is given by $\mathbf{b}_{si} = \int Q_i C_s d\mathbf{x}$, $\boldsymbol{\sigma} = \sum_{j=1}^{N} Q_j \boldsymbol{\sigma}_j$, and the delta function source is approximated by C_s and $\int_\Omega C_s d\mathbf{x} = I_s$. The solution vector $\boldsymbol{\Phi}_s$ gives the potential at each node of the FE mesh. The number of basis functions Q_i is equal to the number of nodes in the FE mesh, both being equal to N.

Homogeneous Neumann and Dirichlet boundary conditions are applied at the boundary of the modelling domain such that the normal derivative of the potential

$$\frac{\partial \phi_s}{\partial \hat{n}} \mid_{\Gamma_{surf}} = 0 \tag{2.3a}$$

at the Earth surface Γ_{surf}, and the potential

$$\phi_s \mid_{(\Gamma - \Gamma_{surf})} = 0 \tag{2.3b}$$

at the remainder of the boundary of the modelling domain.

A physical experiment can be simulated by superposition of two solutions of Eq. 2.2, with source currents of equal strength but opposite polarity. Potential differences between two receiver locations can now be predicted for an arbitrary conductivity distribution $\boldsymbol{\sigma}(\mathbf{x})$. The data predicted in this manner for all source and receiver combinations of a field experiment can be grouped into a single vector $\mathbf{d}^{pre}$.

2.2.1 The Functional

The functional to be optimised to obtain a solution to the inverse problem is

$$F = F_d + F_r^k + F_r^a + F_r^l. \tag{2.4}$$

Here F_d is a measure of the data misfit between observed data and predicted data. F_r^k, F_r^a and F_r^l are regularisation terms containing measures of model structure, anisotropy and deviation from a starting model (steplength damping) respectively. After FE-discretisation, Eq. 2.4 can be written in matrix notation:

$$\begin{aligned} F &= \tfrac{1}{2}(\mathbf{d}^{obs} - \mathbf{d}^{pre})^T \mathbf{W} (\mathbf{d}^{obs} - \mathbf{d}^{pre}) \\ &+ \tfrac{1}{2}\mathbf{m}^T \mathbf{K} \mathbf{m} \\ &+ \tfrac{1}{2}\mathbf{m}^T \mathbf{A} \mathbf{m} \\ &+ \tfrac{1}{2}(\mathbf{m} - \mathbf{m}_{old})^T \mathbf{M} (\mathbf{m} - \mathbf{m}_{old}). \end{aligned} \tag{2.5}$$

where $\mathbf{d}^{obs}$ and $\mathbf{d}^{pre}$ are the observed and predicted data, respectively, and $\mathbf{W}$ is a diagonal data covariance matrix containing weights associated with each datum. The spatial regularisation matrix $\mathbf{K}_{ij}^{\mu\mu} = \int_\Omega \nabla Q_i \boldsymbol{k}^\mu \nabla Q_j d\mathbf{x}$ ($\mu = 1, \ldots, 6$) where $\boldsymbol{k}^\mu = \boldsymbol{k}^\mu(\Omega)$ are positive definite tensors, called diffusion tensors, which can be both inhomogeneous and anisotropic, and which are in general defined with the use of a rotational matrix $\mathbf{R}$ and diagonal matrices $\boldsymbol{\Lambda}^\mu$ by $\boldsymbol{k}^\mu = \mathbf{R}^T \boldsymbol{\Lambda}^\mu \mathbf{R}$ to enable regularisation in arbitrary directions. The current aim is to investigate ways in which prior information can be included into $\mathbf{K}$. In section 2.3 it is shown how to discretise a known structure and assemble bfK. It should be noted that $\mathbf{K}$ is constructed as a second order tensor with dimensions $Nn \times Nn$, where N is the number of nodes in the FE mesh and n is the number of spatial dimensions in the problem. For example, in $\Re^3$, $\mathbf{K}$ looks like a 3×3 block-diagonal matrix with submatrices of dimension $N \times N$ as each of the 9 entries. The matrix $\mathbf{A}$ is based on a discretised Laplacian and penalises anisotropy by making the conductivity eigenvalues $m^\mu(\mu = 1, \ldots, n)$ (see Sec. 2.2.2) equal. The final term contains the material properties $\mathbf{m}_{old}$ of a reference model (e.g. a starting model). Minimising this term reduces the deviation from this reference model.

2.2.2 Material properties

The conductivity tensor $\boldsymbol{\sigma}$ can be described by its eigenvalues $\hat{\sigma}^1$, $\hat{\sigma}^2$ and $\hat{\sigma}^3$, also known as the principal conductivities, and the Euler angles α, β and γ, also called the anisotropy strike, anisotropy dip and anisotropy

slant. The composite rotation is defined by the product:

$$\mathbf{R}(\alpha,\beta,\gamma) = \mathbf{R}_z(\gamma)\mathbf{R}_y(\beta)\mathbf{R}_z(\alpha)$$
$$= \begin{pmatrix} \cos\gamma\cos\beta\cos\alpha - \sin\gamma\sin\alpha & -\sin\gamma\cos\beta\cos\alpha - \cos\gamma\sin\alpha & \sin\beta\cos\alpha \\ \cos\gamma\cos\beta\sin\alpha + \sin\gamma\cos\alpha & -\sin\gamma\cos\beta\sin\alpha + \cos\gamma\cos\alpha & \sin\beta\sin\alpha \\ -\cos\gamma\sin\beta & \sin\gamma\sin\beta & \cos\beta \end{pmatrix}$$

and describes individual rotations of angle α about the z-axis, angle β about the y-axis and angle γ about the rotated z-axis, respectively (Arfken & Weber, 1995). The conductivity tensor can therefore be defined as:

$$\boldsymbol{\sigma} = \mathbf{R}^T\hat{\boldsymbol{\sigma}}\mathbf{R} \tag{2.6}$$

in which

$$\hat{\boldsymbol{\sigma}} = \begin{pmatrix} \hat{\sigma}^1 & 0 & 0 \\ 0 & \hat{\sigma}^2 & 0 \\ 0 & 0 & \hat{\sigma}^3 \end{pmatrix}. \tag{2.7}$$

The inversion variables are the logarithms of the eigenvalues to take account of the fact that they may range over many orders of magnitude, and so the material properties are defined as:

$$m^\mu = \begin{cases} \alpha & \text{if } \mu = 1; \\ \beta & \text{if } \mu = 2; \\ \gamma & \text{if } \mu = 3. \\ \ln(\hat{\sigma}^{\mu-3}) & \text{if } \mu \geq 4; \end{cases} \tag{2.8}$$

The eigenvalues $\hat{\sigma}^{\mu-3} = \exp(m^\mu), \forall\mu \in \{4,5,6\}$ are guaranteed to be positive, because the positive quantities $m^\mu = \ln\hat{\sigma}^{\mu-3}, \forall\mu \in \{4,5,6\}$ are used in the inversion.

2.3 Calculating constraints - Model covariance with structure

In this section the method of incorporating structural constraints based on given structural information into the inversion framework is described. This amounts to calculating the regularisation tensor $\mathbf{k}^\mu$ at each node point of the FE mesh and assembling the matrix $\mathbf{K}$ of Eq. 2.5.

The regularisation tensor $\boldsymbol{k}$ is obtained from the curvature of the known non-dimensional structure $S = \frac{c}{c_0}$, in which c might for example be a seismic velocity field and c_o the average seismic velocity. The idea is to apply small regularisation in the direction and areas where there is large curvature in the structural field S, thus allowing changes in electrical properties. Similarly, large regularisation is to be applied in directions and areas where the known structure S is smooth. To this end the Hessian of S is used.

The scaled Hessian, for a field $S(\Omega)$, in 2D is

$$H = \frac{1}{\overline{|S|}} \begin{pmatrix} \frac{\partial^2 S}{\partial x^2} & \frac{\partial^2 S}{\partial x \partial y} \\ \frac{\partial^2 S}{\partial y \partial x} & \frac{\partial^2 S}{\partial y^2} \end{pmatrix} \tag{2.9}$$

and similarly in higher dimensions, $H = \frac{1}{|S|}\nabla^T\nabla S$. In 1-D the length scale h over which the regularisation acts is such that $\left|\frac{\partial^2 S}{\partial x^2}\right| = \frac{|S|}{h^2}$. In multi-dimensions it is necessary to consider the eigenvalues and eigenvectors of H to determine appropriate length scales and directions over which regularisation acts. H is thus decomposed into its eigenstructure:

$$H = V^T\hat{\Gamma}V. \tag{2.10}$$

An appropriate regularisation tensor would therefore be

$$\mathcal{M} = V^T\left|\hat{\Gamma}^{-1}\right|V \equiv V^T\left|\Gamma\right|V. \tag{2.11}$$

However, there may be a number of fields which can provide different structural information on which constraints can be based. These differing structures can incorporated by superimposing the tensors (metrics) associated with each field.

Suppose the metrics $\mathcal{M}_1$, $\mathcal{M}_2$ are to be superimposed. The distortion D of each metric must first be calculated and is given by

$$D = \frac{\max\{h_i\}}{\min\{h_i\}} \tag{2.12}$$

where the h_i are the eigenvalues of the metric. Suppose then that $\mathcal{M}_1$ is the least distorted and $\mathcal{M}_1 = \mathcal{V}_1^T\Lambda_1\mathcal{V}_1$, $\mathcal{M}_2 = \mathcal{V}_2^T\Lambda_2\mathcal{V}_2$. $\mathcal{M}_2$ is mapped to a space in which $\mathcal{M}_1$ is represented by a unit sphere and so becomes

$$\hat{\mathcal{M}}_2 = \Lambda_1^{-\frac{1}{2}}\mathcal{V}_1\mathcal{M}_2\mathcal{V}_1^T\Lambda_1^{-\frac{1}{2}} = \mathcal{Q}^T\Lambda\mathcal{Q}, \tag{2.13}$$

in which $\mathcal{Q}$ and Λ are the eigenvectors and eigenvalues of $\hat{\mathcal{M}}_2$ respectively. Now the eigenvalues Λ (or $\lambda_i, \forall i \in \{1,2,3\}$) are limited using $\hat{\lambda}_i = \min\{1, \lambda_i\}, \forall i$ and the resulting metric $\hat{\mathcal{M}}$ (with eigenvalues $\hat{\Lambda}$ or $\hat{\lambda}_i, \forall i \in \{1,2,3\}$) is transformed back to the original space to obtain the final metric:

$$\tilde{\mathcal{M}} = \mathcal{V}_1^T\Lambda_1^{\frac{1}{2}}\hat{\mathcal{M}}\Lambda_1^{\frac{1}{2}}\mathcal{V}_1. \tag{2.14}$$

The metric $\tilde{\mathcal{M}}$ represents the maximal inner ellipsoid of the metrics $\mathcal{M}_1$ and $\mathcal{M}_2$, depicted in Fig. 2.1.

Superimposing $n > 2$ metrics is performed by repeating the above procedure, $G(\mathcal{M}_1, \mathcal{M}_2)$, for each additional metric: $\tilde{\mathcal{M}} = G(\ldots G(G(\mathcal{M}_1, \mathcal{M}_2), \mathcal{M}_3)\ldots\mathcal{M}_n)$.

Having formed the metric $\tilde{\mathcal{M}}$ at each node point, the elements of $\tilde{\mathcal{M}}$ are then mapped to the appropriate member of $\boldsymbol{\nu}^\mu$ or $\mathbf{k}^\mu$ which contains the regularisations throughout the whole FE-mesh.

2.3.1 Restricting the magnitude of the regularisation (metric)

It can be the case that in forming the metric as described above by taking the inverse of the curvature that one is left with mostly small values with occasional spikes where the curvature is near zero. This is undesirable since the detail in the areas of small values is lost. To overcome this the eigenvalues of $\tilde{\mathcal{M}}$ are limited to some value which is typical of the rest of the domain values. $\tilde{\mathcal{M}}$ in Eq. 2.14 is further decomposed

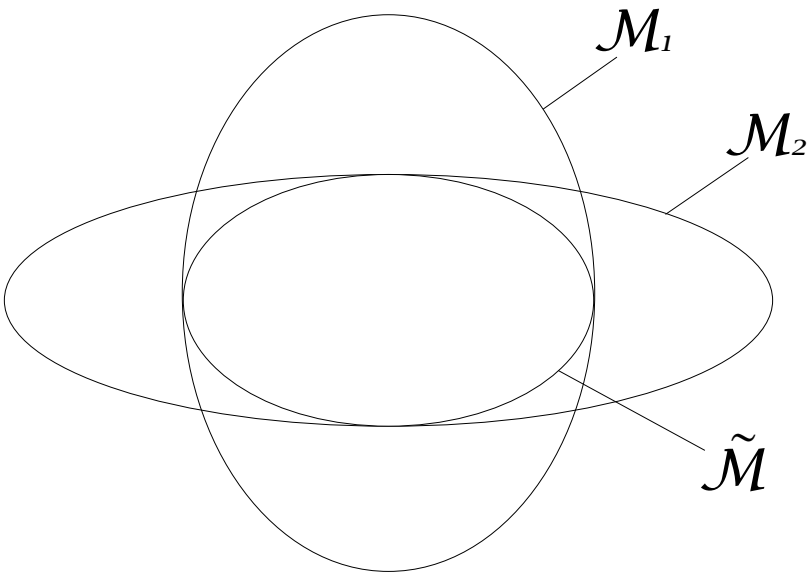

Figure 2.1: Superimposing metrics. Metrics $\mathcal{M}_1$ and $\mathcal{M}_2$ are superimposed on to their maximal inner ellipsoid $\tilde{\mathcal{M}}$.

into its eigenvalues and eigenvectors $\tilde{\mathcal{M}} = \tilde{\mathcal{V}}^T \tilde{\Lambda} \tilde{\mathcal{V}}$ and the magnitudes of the eigenvalues $\tilde{\lambda}_i$ in $\tilde{\Lambda}$ are limited according to $\lambda_i = \min\{a_{max}, \max(a_{min}, \tilde{\lambda}_i)\}, \forall i \in \{1, 2, 3\}$, in which a_{max} and a_{min} are appropriate upper and lower bounds for the eigenvalues throughout the majority of the domain. For simplicity here $a_{min} = 0$. This eigenvalue limiting procedure is demonstrated in the field example described below.

2.4 Scaling constraints - Non-dimensional functions

A major problem in performing constrained inversion is the sensitivity of the inversion model to the size, or strength, of the constraints. A model which is largely smooth can be inverted successfully with strong smoothness constraints. Contrast this with a highly inhomogeneous model with quickly varying properties over short distances. In this case, both the strength of the constraints and the relevant length scale would have to be very different in order to achieve a satisfactory inversion result. In previous work (Herwanger, 2001; Pain et al., 2003; Herwanger et al., 2004b) a large number of inversions were performed, each with a different set of penalty parameters, in order to find optimum constraint levels. While this approach works well, it can be very time-consuming since a large number of inversions are run. The use of non-dimensional variables scales different inversion problems in such a way that penalty parameters of the same magnitude apply independently of the specific details of the inversion problem. This allows exploitation of the experience gained in choosing the magnitude of regularisations to other inversion problems.

Consider the functional F (see Eq. 2.4) given by

$$\begin{aligned} F &= \tfrac{1}{2}\sum_{s=1}^{S}\sum_{r=1}^{R} w_s^r (d_{rs}^{obs} - d_s^r)^2 \\ &+ \tfrac{1}{2}\sum_{\mu=1}^{3} \lambda_\mu^\nu \int \nabla m^\mu \boldsymbol{\nu}^\mu \nabla m^\mu \, dV \\ &+ \tfrac{1}{2}\sum_{\mu=4}^{6} \lambda_\mu^k \int \nabla m^\mu \boldsymbol{k}^{\mu-3} \nabla m^\mu \, dV \\ &+ \tfrac{1}{2}\lambda^a \int (m^1 \; m^2 \; m^3)\mathcal{A}(m^1 \; m^2 \; m^3)^T \, dV \end{aligned} \tag{2.15}$$

where $\boldsymbol{\nu}^\mu \forall \mu \in \{1,2,3\}$ is the smoothness tensor for Euler rotations (material properties m^1, m^2, m^3), and $\boldsymbol{k}^\mu \forall \mu \in \{1,2,3\}$ is the smoothness tensor for conductivity eigenvalues (material properties m^4, m^5, m^6). Note that the second and third terms of F above both relate to F_r^k: the contributions from the conductivity eigenvalues and the Euler rotations have been separated. λ^ν and λ^k are the penalty parameters (smoothness constraints) for Euler rotations and conductivity eigenvalues respectively. The anisotropy penalty, λ^a, is applied equally across all nodes. The step-length damping term F_r^l in Eq. 2.4 has not been included as it is not used in the problems discussed here. The important variables are non-dimensionalised by means of introducing values specific to the situation. The aim is thus to find appropriate non-dimensional variables λ^{k*}, $\lambda^{\nu*}$ and λ^{a*}, given by $\lambda^k \mathbf{k} = \lambda^{k*} K \mathbf{k}^*$, $\lambda^\nu \boldsymbol{\nu} = \lambda^{\nu*} N \boldsymbol{\nu}^*$ and $\lambda^a \mathcal{A} = \lambda^{a*} A \mathcal{A}^*$. The values of the tensors $\boldsymbol{\nu}$ and $\mathbf{k}$ do not change when they are starred, as they are made up from the metrics appropriate to each node. However, a non-dimensional product is made by multiplying them together with characteristic values specific to the individual problem. These are composed of combinations of measurable properties of the problem with the appropriate dimensions: a characteristic length scale (i.e. the distance between boreholes or the size of the domain) L, the natural logarithm of the estimated average conductivity of the domain M, the average of observed voltages or resistances D, and the average rotation of the conductivity tensor Θ, as well as non-dimensional values such as the number of sources S and receivers R used in the inversion problem. Using these new starred variables the term relating to eigenvalue smoothness (the third member on the right hand side of Eq. 2.15) becomes $\frac{1}{2}\frac{M^2L^3}{L^2}\sum_{\mu=4}^{6}\int \nabla^* m^{*\mu} \boldsymbol{k}^{*\mu-3} \nabla^* m^{*\mu} \, dV^*$ where the coordinate transformation $(x,y,z) = L(x^*,y^*,z^*)$ has also been made. Therefore, if we also multiply by SRD^2:

$$\lambda^k \mathbf{k} = \lambda^{k*} \frac{SR}{M^2 L} D^2 \mathbf{k}^*, \tag{2.16}$$

i.e. $K = \frac{SR}{M^2 L} D^2$. Similarly for the Euler rotation smoothness:

$$\lambda^\nu \boldsymbol{\nu} = \lambda^{\nu*} \frac{SR}{\Theta^2 L} D^2 \boldsymbol{\nu}^*, \tag{2.17}$$

and so $N = \frac{SR}{\Theta^2 L} D^2$. For the anisotropy penalty term, $\lambda^a L^3 M^2 \int (m^{*1} \; m^{*2} \; m^{*3})\mathcal{A}^*(m^{*1} \; m^{*2} \; m^{*3})^T \, dV^*$. Therefore:

$$\lambda^a \mathcal{A} = \lambda^{a*} \frac{SR}{L^3 M^2} D^2 \mathcal{A}^*, \tag{2.18}$$

i.e. $A = \frac{SR}{L^3 M^2} D^2$.

After substituting all of the variables in Eq. 2.15 for their non-dimensional equivalents:

$$\begin{aligned} F &= \tfrac{1}{2}D^2 \textstyle\sum_{s=1}^{S} \sum_{r=1}^{R} w_s^r (d_{sr}^{obs*} - d_{sr}^{pre*} - d_s^{r*})^2 \\ &+ \tfrac{1}{2}SRD^2 \textstyle\sum_{\mu=1}^{3} \lambda_\mu^{\nu*} \int \nabla^* m^{*\mu} \boldsymbol{\nu}^{*\mu} \nabla^* m^{*\mu} \, dV^* \\ &+ \tfrac{1}{2}SRD^2 \textstyle\sum_{\mu=4}^{6} \lambda_\mu^{k*} \int \nabla^* m^{*\mu} \boldsymbol{k}^{*\mu-3} \nabla^* m^{*\mu} \, dV^* \\ &+ \tfrac{1}{2}SRD^2 \lambda^{a*} \int (m^{*1} \; m^{*2} \; m^{*3}) \mathcal{A}^* (m^{*1} \; m^{*2} \; m^{*3})^T \, dV^*. \end{aligned} \tag{2.19}$$

Values of the scaling coefficients for three contrasting data sets are shown later, in Table 2.2. All three dimensionless penalty parameters, λ^{k*}, $\lambda^{\nu*}$ and λ^{a*}, lie within approximately one order of magnitude of 10^{-7} for each test, whether it be 2D synthetic, 3D synthetic or 3D field data. They may, therefore, be a useful guide for setting penalty parameters in a wide range of scenarios. With regard to M and Θ which may not be known, it is recommended that a value of unity is of the correct order of magnitude for M, and that $\frac{\pi}{4}$ is a good average value for Θ. Bearing in mind the uncertainties involved in resistivity inversion, this is a significant step forward.

2.5 Inversion of a simplified synthetic model

Here a constrained inversion is performed on synthetic data to show how the constraints are constructed, and to show the benefit of using non-uniform smoothness constraints. The subsurface model used (Fig. 2.2) is identical to that used in Herwanger et al. (2004b), and is based on the geometry of the Reskajeage Quarry borehole site (see Sec. 2.6).

The material properties are summarised in Table 2.1. Average conductivity in Fig. 2.2 is calculated as the arithmetic average of the three conductivity eigenvalues at each node. Anisotropy is given as a percentage and is calculated from the sum of the squared differences of the conductivity eigenvalues divided by the average conductivity, multiplied by 100%. In Fig. 2.2a ellipses are used to depict the conductivity tensor in the $x-z$ plane. Principal conductivities $\hat{\sigma}^1$ and $\hat{\sigma}^3$ are proportional to the major and minor axes, and the tilt angle of the ellipse with respect to the z-axis is equal to Euler angle β. The domain is mostly anisotropic with a left-to-right dip (Euler angle β) of 15^o near the surface and a dip of 7.5^o below 65m. This is punctuated by two narrow isotropic layers, the first a conductive zone lying between 75 and 80m depth, the second a resistive zone between 60 and 70m depth, rising to 50m depth at the left edge of the domain.

First an inversion is shown with uniform constraints across the whole domain. The maximum roughness penalty $\lambda^{k*} = 10^{-5}$, with an anisotropy penalty $\lambda^{a*} = 10^{-6}$. These are the optimum parameters determined in Herwanger et al. (2004b). The result of this inversion after 20 iterations is shown in Fig. 2.3. A resistive region at around 60m depth can be identified, and a more conductive region between 70 and 85m depth. The top 30-40m is seen to be more anisotropic than the lower region, with an area of very low anisotropy between 60 and 80m. However, the coherence of the conductivity field, particularly in the top region, is poor, as is the definition of the thin strip between 75 and 80m in both the conductivity and anisotropy images.

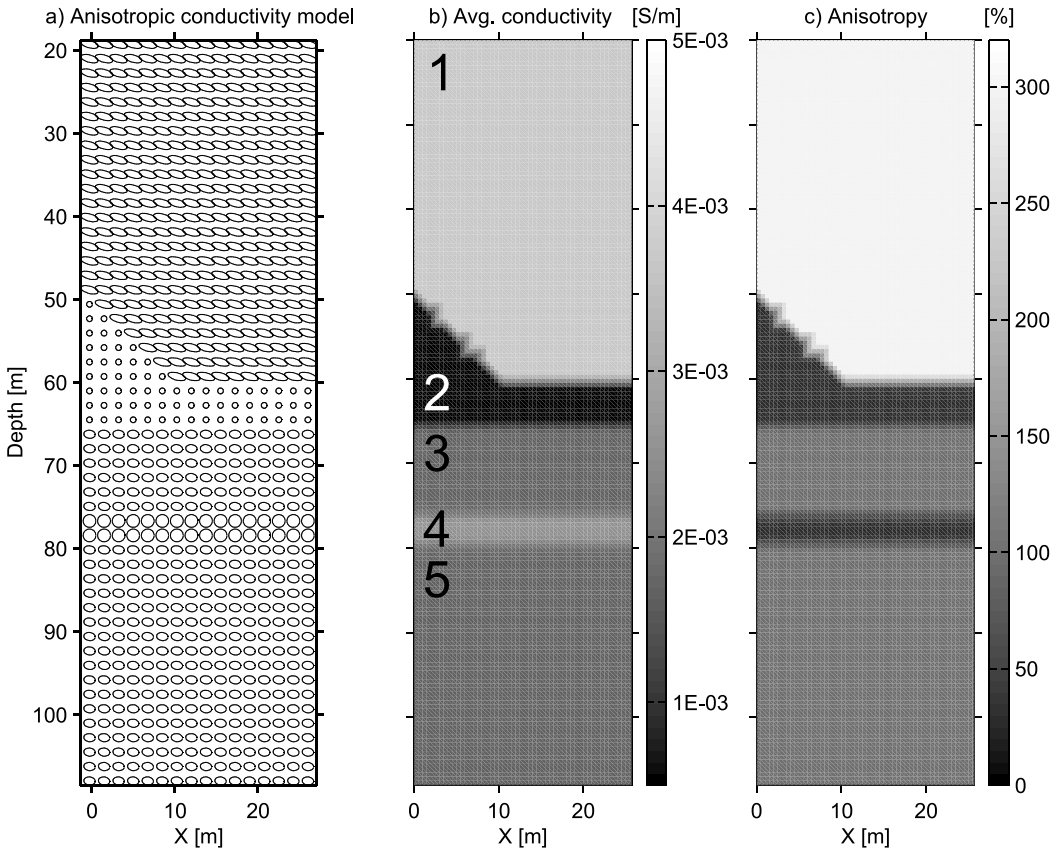

Figure 2.2: The forward model for the synthetic example. (a) The conductivity tensor depicted using ellipses. Conductivity eigenvalues are proportional to the major and minor axes of the ellipses, and tilt angle with respect to the vertical is equal to Euler angle β. (b) and (c) Average conductivity and anisotropy models, respectively. Average conductivity is the arithmetic mean of the conductivity eigenvalues, and anisotropy is calculated by the sum of the squared differences between conductivity eigenvalues divided by the average conductivity. The material properties of each of the five regions numbered in b) are described in Table 2.1.

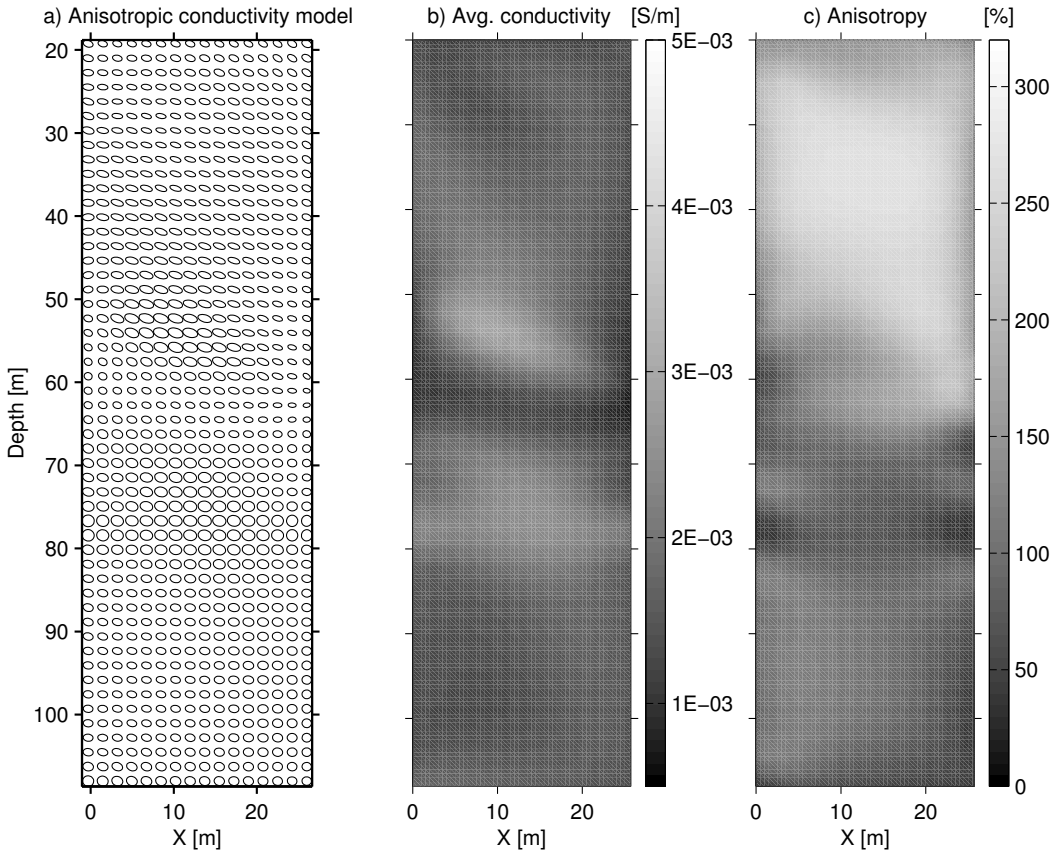

Figure 2.3: The result from inversion using uniform constraints as applied in Herwanger et al. (2004b). The boundaries between the contrasting regions are poorly defined and the horizontal coherence does not adequately reflect the layering of the forward model.

Region	Bounds of regions	Parameters
1	$z < 60.0, z < 60.0 - 10 + x$	$\beta = -15^o$ $\sigma^1 = \sigma^2 = 0.005\ S/m$ $\sigma^3 = 0.0008\ S/m$
2	$65.0 > z > \begin{cases} 60.0 - 10 + x & x < 10 \\ 60 & x > 10 \end{cases}$	$\beta = 0^o$ $\sigma^i = 0.0005\ S/m\ \forall i$
3	$65.0 < z < 75.0$	$\beta = -7.5^o$ $\sigma^1 = \sigma^2 = 0.002\ S/m$ $\sigma^3 = 0.001\ S/m$
4	$75.0 < z < 80.0$	$\beta = 0^o$ $\sigma^i = 0.0025\ S/m\ \forall i$
5	$z > 80.0$	$\beta = -7.5^o$ $\sigma^1 = \sigma^2 = 0.002\ S/m$ $\sigma^3 = 0.001\ S/m$

Table 2.1: Material properties for layered three-dimensional synthetic model.

Next structural constraints are calculated from the known structure of the true model. Large penalty values are used in regions where the model is known to be flat, while the penalty is reduced where changes in material properties occur. Further, the constraint tensors can be anisotropic to enforce smoothness along an interface while allowing changes in material properties across it. Fig. 2.4 shows the constraint tensor components throughout the domain. The horizontal and vertical components of the metric $\mathcal{M}^{11}$ and $\mathcal{M}^{33}$ are large in the majority of the domain, reflecting the large homogeneous regions in the model. The metric, and therefore the corresponding smoothness constraint, is only reduced in the vicinity of the boundaries between layers. For example, the horizontal smoothness penalty (Fig. 2.4a) is only reduced on the diagonal edge of the resistive isotropic region. By contrast the vertical constraints (Fig. 2.4c) are more varied as there are several changes in conductivity from the top to the bottom of the domain. These vertical constraints are scaled according to the magnitude of the curvature at each point. On this uniform mesh the interfaces with the highest conductivity contrast have the smallest constraints, and vice versa. Fig. 2.4b shows the diagonal component of the metric $\mathcal{M}^{13}$ which is zero across most of the domain, but is non-zero along the diagonal edge of the resistive isotropic region. This enforces smoothness along the tilted interface and allows a change in material properties across the interface. To illustrate the different values of the metric throughout the domain its value is shown at the three locations marked in Fig. 2.4, T1 (on the diagonal edge of the resistive isotropic region), T2 (on the lower

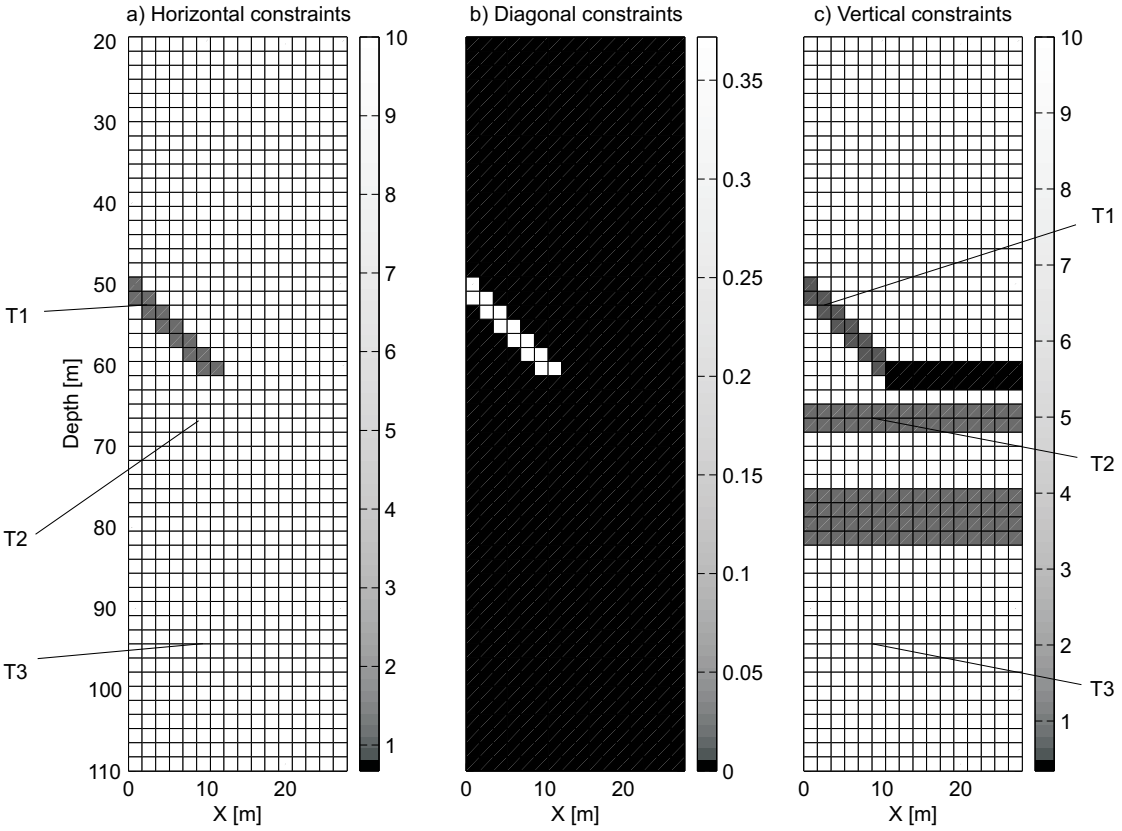

Figure 2.4: The horizontal, diagonal and vertical components of the regularisation tensor at each node point calculated from the known structure in Fig. 2.2. The full tensors at three locations in the domain, T1, T2 and T3, (marking an inclined plane, a horizontal interface and a homogeneous region, respectively) are shown in Eqs. 2.20, 2.21 and 2.22.

edge of the same region) and T3 (in the flat lower part of the domain):

$$\mathcal{M}_{T1} = \begin{pmatrix} 0.673 & 0 & 0.327 \\ 0 & 10^6 & 0 \\ 0.327 & 0 & 0.673 \end{pmatrix}, \tag{2.20}$$

$$\mathcal{M}_{T2} = \begin{pmatrix} 10 & 0 & 0 \\ 0 & 10^6 & 0 \\ 0 & 0 & 0.95 \end{pmatrix}, \tag{2.21}$$

$$\mathcal{M}_{T3} = \begin{pmatrix} 10 & 0 & 0 \\ 0 & 10^6 & 0 \\ 0 & 0 & 10 \end{pmatrix}. \tag{2.22}$$

The value of 10^6 applied as a smoothness constraint in the second horizontal direction (out of the page, in Fig. 2.4) ensures that the model is effectively two-dimensional (see Sec. 2.6). The remaining values have been normalised by the value at the smoothest interface, which in this model is the boundary between the isotropic layer at 75-80m depth and the enclosing regions. This means that the constraints on the interfaces are initially in the range $[0, 1]$. Constraints in the flat regions are larger, and so enforce more smoothness. In this example the constraints in the flat regions of the model have been set to be an order of magnitude larger than anywhere else (see values of 10 in the above tensors). The tensors are then multiplied by the penalty parameter λ^k appropriate to the model. Here this parameter is 10^{-5}, as used in the previous inversion using uniform constraints. Thus knowledge of structure of the domain is used both to increase and decrease the constraints around the optimum value.

The results of structurally constrained inversion for this problem are shown in Fig. 2.5. It is immediately apparent that this inversion is a great improvement compared to the inversion in Fig. 2.3 using uniform constraints. The average conductivity model in particular is very similar to the forward model. The anisotropy values are generally well recovered, except in the resistive region between 50 and 70m depth. The poor reconstruction can be explained by the general difficulty in imaging resistive regions. Current is channelled around resistive regions into nearby conductive paths. Little current passes through the resistive body and the directional effects have only marginal influence on the data. In contrast, the lower conductive isotropic layer is well depicted, as is the anisotropy in the upper and lower parts of the domain.

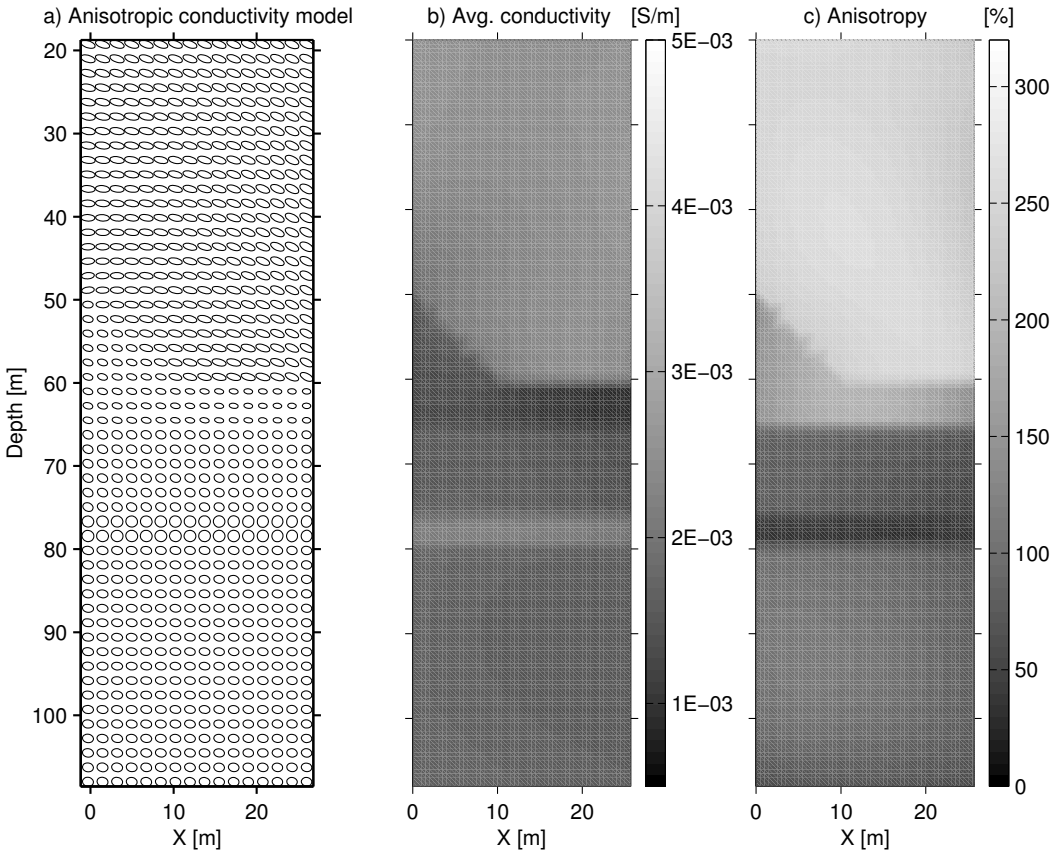

Figure 2.5: The inversion model using the structural constraints in Fig. 2.4. The boundaries between contrasting regions are sharp and well defined. Note the marked improvement of this inversion model compared to the inversion model using uniform smoothness constraints in Fig. 2.3. See text for a detailed description.

2.6 Inversion of field data

2.6.1 Description of site and previous inversions

The Reskajeage Quarry research site is located in West Cornwall, UK, in Devonian metasediments. The rocks are extensively fractured and hydraulic tests have revealed variable degrees of fracture permeability. Two deep boreholes drilled to a depth of 250m span a plane perpendicular to the predominant strike direction of both the fracture planes and the layering of the sediments. Therefore a two-dimensional geometry can be assumed. Herwanger et al. (2004a) describe the seismic data tomography experiment from this site and Herwanger et al. (2004b) carry out anisotropic resistivity inversion using uniform constraints across the domain. The results of these inversions are shown in Fig. 2.6. Fig. 2.6a shows a seismic tomogram, depicting directionally averaged seismic velocity and Fig. 2.6b depicts average conductivity. The two tomograms show many similarities, especially toward the lower half of the model, where higher seismic velocities (red) correspond to lower conductivities (also red). In the upper part of the model, above 50m depth, the correlation is a lot less clear. In particular the clear boundary in the seismic image from 30m depth on the left edge down to 43m on the right edge is not present in the conductivity model. Note also that the electrical image is not coherent between the boreholes - shown most clearly by the blue-green conductive region between 70 and 80m depth, which does not extend to the edges of the domain, unlike the mid-low velocity region in the corresponding part of the seismic image. This behaviour has been noted in inversion of synthetic data and can suggest a shortcoming of the imaging method. Alternatively it could be caused by the proximity of the sources and receivers in the borehole, and the large sensitivity to data error in this region.

2.6.2 Formulation of constraints

To improve on the result obtained by using uniform constraints for all regions of the domain, the constraints are now based on the known seismic structure. While increases in seismic velocity do not necessarily correspond to increases in electrical resistivity, it is believed that the structure of the model as defined by its curvature is likely to be similar for both properties (Haber & Oldenburg, 1997). For example, although a region containing many fluid-filled fractures may have both a low seismic velocity (caused by compliant fractures) and a low resistivity due to the presence of conductive fluid, the magnitude of change in these physical properties might not be easily quantified. By using the curvature, where seismic velocities change resistivities will be able to change also. Therefore, by allowing the regions with high frequency changes in velocity as shown in the seismic images to develop roughness in the electrical model and forcing the homogeneous regions to stay homogeneous, the inversion is given valuable additional information.

The application of constraints based on seismic data cannot be an entirely automatic procedure - areas with near-zero curvature will have very large constraints and areas with unusually large curvature will have very

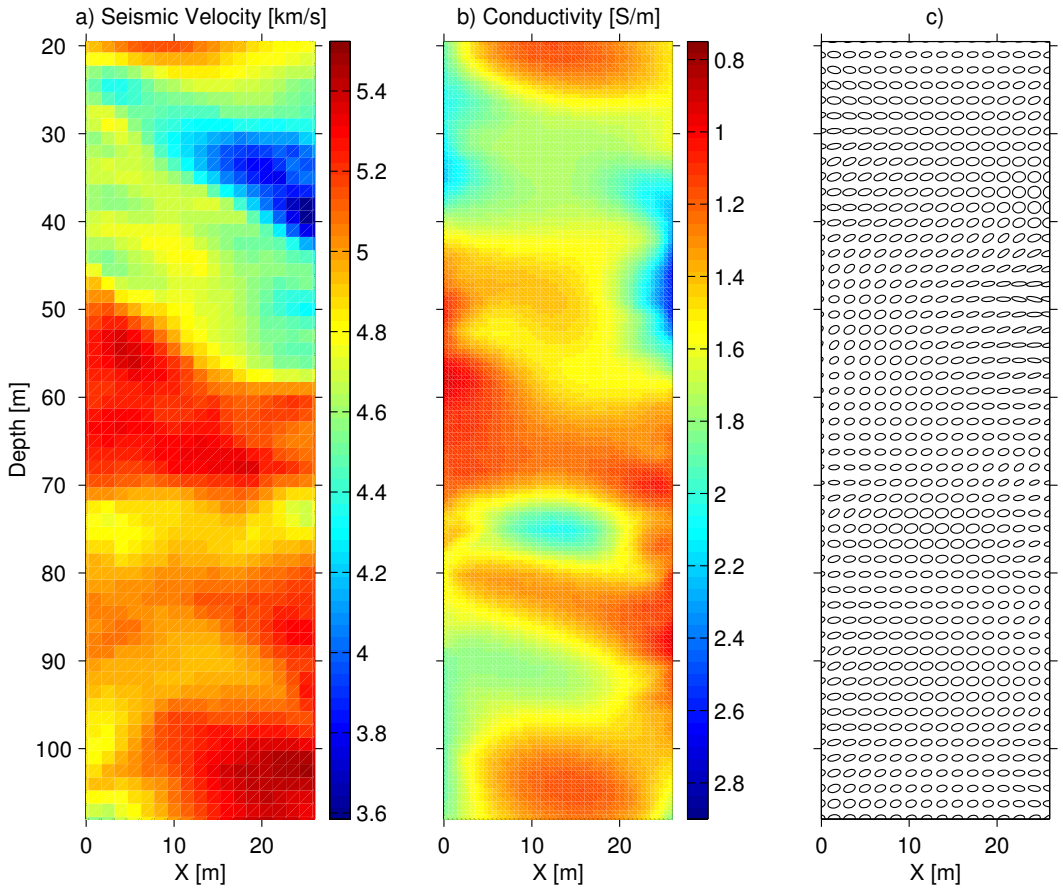

Figure 2.6: Comparison of independent seismic and electric inversion from Herwanger et al. (2004b). (a) Average seismic velocity and (b) average electrical conductivity. Note the broad correlation between the images, with regions of high seismic velocity corresponding to regions of low electrical conductivity, and regions of low seismic velocity corresponding to regions of high electrical conductivity. (c) The conductivity tensors showing the anisotropy of the conductivity model.

small constraints applied. It is up to the skill of the user to construct constraints in such a way as to distinguish adequately between these two extremes while producing enough detail and contrast in between. This may be achieved in a variety of ways. Here, the magnitude of the inverse of the eigenvalues is restricted as described in section 2.3.1, then normalised across the whole domain so that the range of values lies between 0 and 1. This allows the constraints to be easily scaled according to the non-dimensional functions, so that they are appropriate for the inversion. However, in this inversion it is desired both to allow more roughness and also to enforce more smoothness than in the uniformly constrained inversion, as was done in the previous synthetic example but now according to the seismic data. Therefore the new eigenvalues are multiplied by a factor of 10 in those regions where the eigenvalues had to be restricted previously, to achieve this extra smoothness.

Characteristic values for this model are shown in Table 2.2 (case 1), along with non-dimensional (starred) variables which are applicable to all problems. In this instance, extensive experimentation has been carried out on the Reskajeage data to determine the most appropriate constraint values for inversion (Herwanger, 2001; Herwanger et al., 2004b), and so these same values are used here to show the effect of adding constraints. The optimum roughness constraint was found to be 10^{-5}, therefore we construct our structural constraints around this value, so that they lie in the range $[0, 1E-4]$. The optimum anisotropy constraint which is constrained homogeneously is $\lambda^a = 10^{-8}$.

2.6.3 Results from inversion with constraints based on seismic data

Fig. 2.7 shows the results of inversion using constraints based on the curvature of the seismic velocity, along with the seismic velocity data itself. The effect of the constraints is evident as the conductivity model (Fig. 2.7b) is quite markedly different to that from the uniformly constrained inversion (Fig. 2.6b). Two areas most clearly show the benefit of the new constraints.

First, the region between 80 and 55m depth, in which a resistive dipping zone overlays a thin horizontal conductive layer. A similar layering is seen in Fig. 2.6b, but the resistive zone is only suggested near the edges of the domain, while the conductive layer has a greater vertical extent. The use of anisotropic constraints based on the seismic data, which correspondingly show a high velocity, laterally coherent zone over a slower, thin layer, has resulted in an improved image. It has been ensured here that changes in conductivity between vertically adjacent nodes are confined to those in which changes in the seismic data appear. This means that the conductive region cannot appear larger than it really is, nor the resistive layer thinner, as would usually be the case. Furthermore, since the seismic data is horizontally smooth and so the horizontally roughness constraints are large, the high resistivities seen around the sources and receivers in Fig. 2.6b are propagated right across the domain.

Second, the region of the domain above 50m depth. The seismic data shows a clear dipping boundary at the bottom of this area, and another contrast around the triangular, low velocity inclusion on the right side. One

Variable	Description	Value		
		Reskajeage Model	2D synthetic	3D synthetic
S	Number of sources	88	18	45
R	Number of receivers	87	18	45
L	Typical distance between sources and receivers (m)	25.7	40	50
M	Natural logarithm of average conductivity	1	1	1
D	Average of observed voltages or resistances	1.04	0.604	0.317
Θ	Average rotation of tensor	$\frac{\pi}{4}$	$\frac{\pi}{4}$	$\frac{\pi}{4}$
λ^k	Eigenvalue roughness penalty	1×10^{-4}	1×10^{-6}	3.1×10^{-5}
λ^ν	Euler rotation roughness penalty	1×10^{-4}	1×10^{-6}	3.1×10^{-5}
λ^a	Anisotropy penalty	1×10^{-8}	$5 \times 10{-}10$	3.1×10^{-9}
λ^{k*}	Dimensionless eigenvalue smoothness penalty	3.1×10^{-7}	3.4×10^{-7}	7.6×10^{-6}
$\lambda^{\nu*}$	Dimensionless Euler rotation smoothness penalty	1.9×10^{-7}	2.1×10^{-7}	4.7×10^{-6}
λ^{a*}	Dimensionless anisotropy penalty	2.0×10^{-8}	2.7×10^{-7}	1.9×10^{-6}

Table 2.2: Parameters relevant to three differing inversions, the Reskajeage field data inversion, and two synthetic models which are not discussed in this chapter. The 2D synthetic model is shown in Fig. 2 of Pain et al. (2003), and the 3D synthetic model is a similar single-prism problem. We see that despite the contrasting physical features of the three problems, the dimensionless penalty values shown are similar for each one.

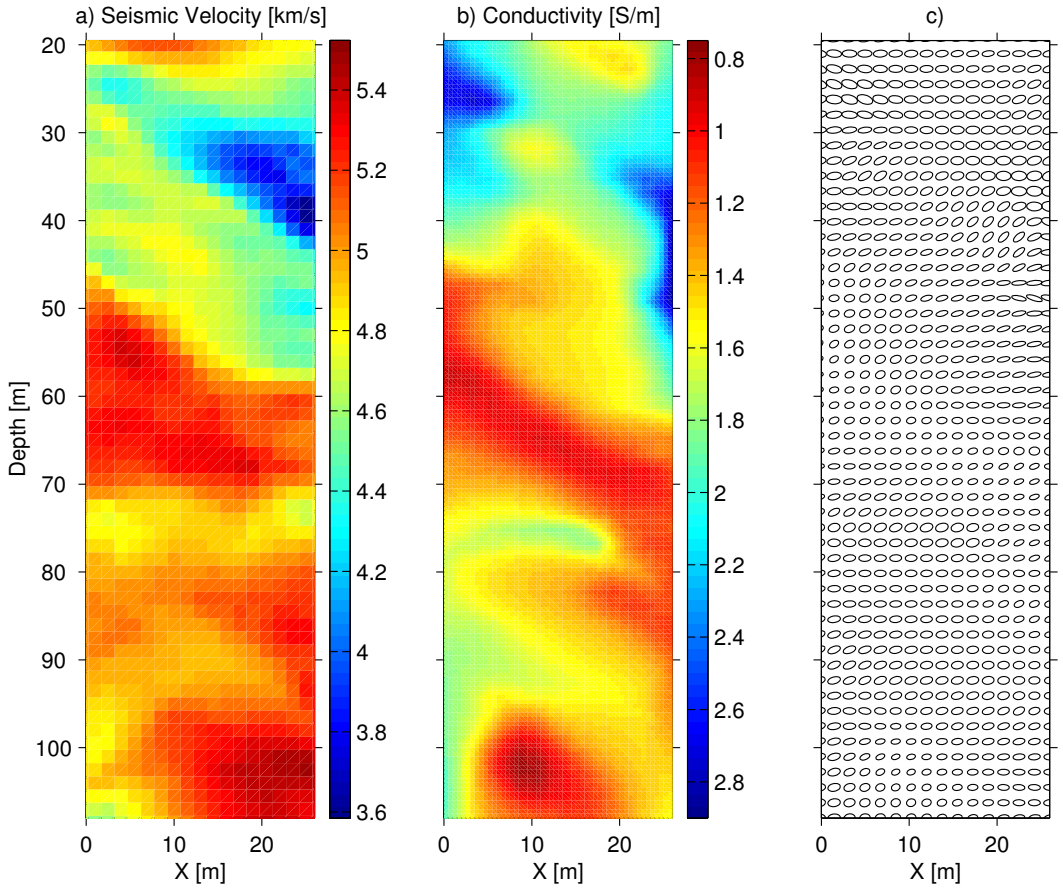

Figure 2.7: Comparison of seismic tomogram with electrical tomogram resulting from inversion using constraints based on the seismic data. (a) Average seismic velocity, (b) average conductivity and (c) the conductivity tensors. Note the improved correlation between (a) and (b) compared with Fig. 2.6.

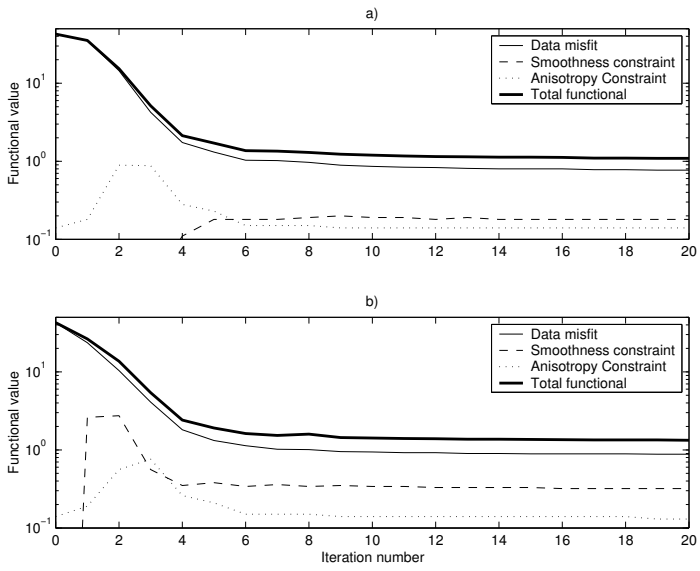

Figure 2.8: Convergence of the data misfit functionals, a) for the uniformly constrained inversion and b) for the inversion using constraints derived from seismic data.

would expect these features to be apparent in the electrical model, especially since this whole upper region is more densely fractured than the lower parts (Herwanger, 2001). Fig. 2.7b does indeed show more similarity in structure to the seismic data than the corresponding model using uniform constraints. The left-to-right dip is more apparent, and a small resistive feature near the middle of the domain at 30m depth can be made out. The location of this feature corresponds to the apex of the low velocity triangular inclusion shown in the seismic model, where the roughness constraints will be low. A similar drop in conductivity can be seen in Fig. 2.6b, but the strong constraints do not allow the feature to develop fully. Also, as in the lower region, the anisotropic nature of the constraints has allowed changes in the conductivity model to occur across horizontal or near-horizontal boundaries while preserving the smoothness across the domain. This allows the conductive areas seen previously only around the very edge in this top region, to appear as more coherent and significant structures within the conductivity model.

Fig. 2.8 shows the convergence of the functionals F_d, F_r^k, F_r^a and the overall functional F (see Eq. 2.4) for a) the uniformly constrained inversion and b) the inversion using constraints from the seismic data. The smoothness constraint is larger overall using constraints from seismic data since we have increased its value in the smoothest regions (of which there are several) and reduced it in the rougher regions (of which there are few). This leads to a slightly increased total functional. On the basis of the data misfit the new model is as good a fit to the data as the previous inversion model, achieving a high level of convergence in relatively few iterations.

2.7 Conclusions

In this chapter a method of adding suitable model covariance for anisotropic resistivity inversion has been presented, along with methods for guiding the magnitude of the model covariance, by making the method easily applicable to a wide range of resistivity inversion problems. The model covariance developed here is used to reduce the ambiguity associated with resistivity inversion and in particular anisotropic resistivity inversion. Anisotropic constraints based on the curvature of the known structure have been used, resulting in a significant increase in inversion accuracy in a synthetic example. These constraints also applied to a field problem where structural information was obtained from an anisotropic seismic velocity field. In this case appropriate constraints were used to regularise both homogeneous coherent regions and highly fractured regions in the domain. Such constraints can help to reduce the effect of two common problems associated with resistivity inversion, source-receiver effects and false imaging of highly resistive/conductive regions. Better correlation in general terms with other geophysical data give increased confidence in the inversion result. In particular, these results provide some evidence that the seismic and electric structures of the subsurface, defined in terms of curvature, coincide and that this property may be used to inform and improve resistivity inversion where seismic data exist.

Chapter 3

Streaming Potentials from Reservoir Fluid Flow

3.1 Introduction

As global hydrocarbon demand continues to increase and supplies in known reservoirs are further depleted, increased importance is placed on the efficiency with which those supplies are produced and on minimising wastage. Where a reservoir is produced by a water injection programme, the breakthrough of the water to the producing well will compromise the subsequent production rate and possibly restrict further production from that well. Intelligent Well Technology (IWT) may be deployed to monitor production and to allow the well operator to control the flow at the available pay zones along the borehole (Armstrong & Jackson, 2001). Ideally, the IWT would signal the imminent arrival of the approaching water front before it reaches the borehole, allowing production to continue uninterrupted. Such technology should not interfere with the ongoing production, and should enable experiments to be performed from which the results can be interpreted quickly and simply. In terms of engineering, the equipment deployed should also be minimal and reliably operable from the Earth surface.

Electrical methods for characterisation are well suited to this environment. Resistivity measurements are non-destructive and can be carried out without interfering with other production-related processes. Electrodes can be fitted to other borehole equipment requiring only a current supply, and the lack of moving parts makes the equipment robust and reliable. The recorded data are easily interpreted and do not require substantial processing, other than removal of noise which may arise from other electrical equipment or from the natural magnetic field. As an alternative to current injection methods, the natural electrical properties of the fluids can also be utilised, in particular electrokinetic phenomena. The electric field generated by ionic fluids moving

through rock has been studied over a number of years and is presently the subject of considerable theoretical (Bernabé, 1998; Revil & Cerepi, 2004) and experimental work (Beamish, 1999; Fagerlund & Heinson, 2003; Jiang et al., 1998; Thompson & Gist, 1993). On the microscopic level, a drag current is caused by the motion of fluid through the pores. This moves excess charge in the electric double layer formed at the fluid/mineral interface. The electrical potential field resulting from this current flow is known as the streaming potential. Electrokinetic phenomena also include the mechanical movement of charged particles in an electric field, known as electro-osmosis. The density of charge in the double layer is dependent on many variables, including the mineral and fluid chemistry, pore fluid pH and salinity and temperature (Revil et al., 1999a), and will be further complicated by multi-phase flow. The ζ- (zeta-) potential, which is roughly equal to the electrical potential at the interface, encapsulates this complexity but has been only occasionally investigated in a controlled environment. Indeed, recent laboratory experiments (Guichet et al., 2003; Revil & Cerepi, 2004) have contradicted the theory (Revil et al., 1999b) of the ζ-potential, and further adjustments to the theory are inevitable as further results taken under varying conditions are obtained. The ζ-potential remains the principal source of uncertainty within the electrokinetic method as a whole. However, using the present best estimates for the value of the ζ-potential, the modelling described here suggests that electrical potentials arising through electrokinetic coupling and measured in the borehole are of the order of millivolts. Random noise in a deep well environment may typically be of the order of 0.1mV (Bryant et al., 2002); thus these streaming potentials may be large enough to be distinguished from background noise.

In this chapter the governing equations for a passive reservoir monitoring experiment are first presented. A description is then given of the synthetic and 'realistic' reservoir models to be used, followed by the results from the passive modelling. The model is validated against results in the literature (Wurmstich & Morgan, 1994) and, using data on the ζ-potential from recent experiments (Revil & Cerepi, 2004), it is found that both the coupling coefficient of the pore fluid and its resistivity are important in governing the potentials measured at the borehole. The active current injection experiment is then described, and it is shown that a change in water content of the near-borehole formation can be detected by this method. Both the active and the passive experiments may therefore be viable tools for use in monitoring fluid distributions in a hydrocarbon reservoir during production, and both methods may be capable of detecting the approaching water front in sufficient time to allow flow control measures to be implemented.

3.2 Governing equations for the passive experiment

To model the flow of fluids in a reservoir with electrokinetic coupling, a series of simple equations are solved, derived from the following pair (Wurmstich & Morgan, 1994):

$$\mathbf{q} = -\frac{k}{\eta}\nabla p, \tag{3.1}$$

$$\mathbf{j} = -C\sigma_r \nabla p - \sigma_r \nabla U. \tag{3.2}$$

The term governing the contribution to fluid velocity $\mathbf{q}$ by the electric potential U is negligible and is omitted from Eq. 3.1 here. This leaves Darcy's Law relating fluid velocity to hydraulic pressure p, via the fluid viscosity η and permeability k. The potential arises through Eq. 3.2 which relates the current density $\mathbf{j}$ to the pressure and potential via the rock conductivity σ_r and the coupling coefficient C. The current density is separated into two parts, $\mathbf{j} = \mathbf{j}_{drag} + \mathbf{j}_{cond}$, where $\mathbf{j}_{drag} = -C\sigma_r \nabla p$ is the drag current caused by the charge moving with the fluid and $\mathbf{j}_{cond} = -\sigma_r \nabla U$ is the conduction current resulting from the established potential. With no external current source $\nabla.\mathbf{j} = 0$ and thus

$$\nabla.\mathbf{j}_{drag} = -\nabla.\mathbf{j}_{cond}. \tag{3.3}$$

A sink term Q is used to simulate production at the borehole at a given rate. This might usually be defined by a Gaussian function in three dimensions, and is related to the velocity field by:

$$\nabla.\mathbf{q} = Q = -Ge^{-r^2/l^2}, \tag{3.4}$$

where the multiplier G is scaled so that the integral of the sink function over the entire domain gives the appropriate fluid volume extraction rate, l is a length scale determining the spatial spread of the sink function over the nodes of the mesh, and r is the distance from the sink centre. The following set of equations allows each of the variables to be determined in turn, beginning with the sink term Q:

$$\nabla.(\frac{k}{\eta}\nabla p) = -Q, \tag{3.5a}$$

$$\mathbf{q} = -\frac{k}{\eta}\nabla p, \tag{3.5b}$$

$$\nabla.\mathbf{j}_{drag} = \nabla.(C\sigma_r \frac{\eta}{k}\mathbf{q}), \tag{3.5c}$$

$$\nabla.(\sigma_r \nabla U) = \nabla.(C\sigma_r \frac{\eta}{k}\mathbf{q}), \tag{3.5d}$$

$$\mathbf{j}_{cond} = -\sigma_r \nabla U. \tag{3.5e}$$

Boundary conditions enforce zero normal flow of fluid or of current at the Earth surface as well as zero potential and zero fluid flow far from the borehole (modelling 'infinity').

3.2.1 Discretisation of variables

To solve these equations numerically a finite-element mesh with $\mathcal{N}$ distinct basis functions N_j and $\mathcal{M}$ distinct basis functions M_j is used. In the examples presented here with the use of an 8-node hexahedral element, N_j represents the bi-linear basis centred on the nodes and M_j is unity across elements and zero

elsewhere. See Zienkiewicz & Taylor (2000) for more information on this element type. The discretised modelling variables are expanded in terms of these bases such that:

$$Q = \sum_{j=1}^{\mathcal{N}} N_j Q_j \tag{3.6a}$$

$$\mathbf{q} = \sum_{j=1}^{\mathcal{N}} N_j \mathbf{q}_j \tag{3.6b}$$

$$\mathbf{j}_{drag} = \sum_{j=1}^{\mathcal{N}} N_j \mathbf{j}_{drag_j} \tag{3.6c}$$

$$\mathbf{j}_{cond} = \sum_{j=1}^{\mathcal{N}} N_j \mathbf{j}_{cond_j} \tag{3.6d}$$

$$p = \sum_{j=1}^{\mathcal{M}} M_j p_j \tag{3.6e}$$

$$U = \sum_{j=1}^{\mathcal{M}} M_j U_j \tag{3.6f}$$

Eqs. 3.5b and 3.5e are multiplied by N_i and integrated over the domain, while Eqs. 3.4 and 3.5c are multiplied by M_i and integrated over the domain. The resulting equations are

$$\mathbf{B}^T \underline{\mathbf{q}} = \mathbf{M} \underline{Q}, \tag{3.7a}$$

$$\mathbf{B} \underline{p} = \mathbf{A}_{\frac{\eta}{k}} \underline{\mathbf{q}}, \tag{3.7b}$$

$$\mathbf{B}^T \underline{\mathbf{j}}_{drag} = \mathbf{D} \underline{\mathbf{q}} \tag{3.7c}$$

and

$$\mathbf{A}_{\frac{1}{\sigma}} \underline{\mathbf{j}}_{cond} = \mathbf{B} \underline{U}, \tag{3.7d}$$

where $\underline{\mathbf{q}}^T = (\mathbf{q}_1, \mathbf{q}_2, \ldots, \mathbf{q}_{\mathcal{N}})$ and similarly for the other vectors $\underline{Q}, \underline{p}, \underline{\mathbf{j}}_{drag}, \underline{\mathbf{j}}_{cond}$ and $\underline{U}$.

The matrices $\mathbf{M}$, $\mathbf{A}$, $\mathbf{B}$ and $\mathbf{D}$ are given by:

$$\mathbf{M} = \int N_i N_j dV, \tag{3.8a}$$

$$A_{\frac{\eta}{k}ij} = \int N_i \frac{\eta}{k} N_j dV, \tag{3.8b}$$

$$A_{\frac{1}{\sigma}ij} = \int N_i \frac{1}{\sigma_r} N_j dV, \tag{3.8c}$$

$$B_{x_{ij}} = \int \frac{dN_i}{dx} M_j dV, \tag{3.8d}$$

$$B_{y_{ij}} = \int \frac{dN_i}{dy} M_j dV, \tag{3.8e}$$

$$B_{z_{ij}} = \int \frac{dN_i}{dz} M_j dV. \tag{3.8f}$$

$$\mathbf{B} = \begin{pmatrix} B_x \\ B_y \\ B_z \end{pmatrix}, \tag{3.8g}$$

and

$$D_{x_{ij}} = \int C\sigma_r \frac{\eta}{k} \frac{dN_i}{dx} M_j dV, \tag{3.8h}$$

$$D_{y_{ij}} = \int C\sigma_r \frac{\eta}{k} \frac{dN_i}{dy} M_j dV, \tag{3.8i}$$

$$D_{z_{ij}} = \int C\sigma_r \frac{\eta}{k} \frac{dN_i}{dz} M_j dV. \tag{3.8j}$$

$$\mathbf{D} = \begin{pmatrix} D_x \\ D_y \\ D_z \end{pmatrix}, \tag{3.8k}$$

The discretised equivalent of Eqs. 3.5a-e is therefore:

$$\mathbf{B}^T \mathbf{A}_{\frac{\eta}{k}}^{-1} \mathbf{B} \underline{p} = \mathbf{M} \underline{Q}, \tag{3.9a}$$

$$\mathbf{A}_{\frac{\eta}{k}} \underline{\mathbf{q}} = \mathbf{B} \underline{p}, \tag{3.9b}$$

$$\mathbf{B}^T \underline{\mathbf{j}}_{drag} = \mathbf{D} \underline{\mathbf{q}}, \tag{3.9c}$$

$$\mathbf{B}^T \mathbf{A}_{\frac{1}{\sigma}}^{-1} \mathbf{B} \underline{U} = \mathbf{D} \underline{\mathbf{q}}, \tag{3.9d}$$

$$\mathbf{A}_{\frac{1}{\sigma}} \underline{\mathbf{j}}_{cond} = \mathbf{B} \underline{U}. \tag{3.9e}$$

In practice Eq. 3.9a is solved for the pressure $\underline{p}$, using a preconditioned conjugate gradient solver, followed by the solution of Eq. 3.9b for $\underline{\mathbf{q}}$. The streaming potential $\underline{U}$ is solved finally, using Eq. 3.9d. Natural boundaries applied during the solution of these equations are zero normal fluid velocity and current flow at the Earth surface, and zero pressure and zero potential at the far-field boundary modelling 'infinity'.

The rock conductivity σ_r for a rock with porosity ϕ is calculated using Archie's Law, and also accounts for the presence of both water and oil in the pore space:

$$\sigma_r = \phi^{1.8}(\sigma_{oil} + S^2(\sigma_{water} - \sigma_{oil})). \tag{3.10}$$

The saturation fraction $S \in [0, 1]$ describes the amount of water in the pore space. If $S < 1$ then the remaining space is assumed to be filled with oil. The conductivity of the rock grains themselves is neglected, as sandstone resistivities are typically of the order of $1E8\Omega$m (Telford et al., 1990).

The electrokinetic term is defined by:

$$L = C\sigma_r = \frac{-\zeta\epsilon}{\eta}\phi^{1.8} \tag{3.11}$$

where ζ is the zeta potential and ϵ is the dielectric permittivity. (The units of L are Volts.Siemens/Pa.m = A/Pa.m). The zeta potential (in Volts) is calculated as follows (Pride & Morgan, 1991):

$$\zeta = -max(0.02, -0.001 * (8 + 26log_{10}(c)) \tag{3.12}$$

where c is the fluid conductivity in units of Mol/L (Wurmstich & Morgan, 1994). In the absence of any experimental data to suggest a functional relationship between water saturation and the electrokinetic coupling term L, a linear interpolation is used for mixed phase flow:

$$L_m = L_{oil} + S^{'}(L_{water} - L_{oil}) \tag{3.13}$$

where $S^{'}$ is the adjusted, or effective saturation which only includes the fluid which is mobile in the pore space.

3.3 Passive monitoring of a simplified reservoir

An idealised synthetic reservoir model is used to show the effect of an approaching water front on the electric potential measured at the borehole, and is based on the model described by Wurmstich & Morgan (1994). The domain measures 2 × 2km centred on the origin and is 1.1km thick. Fig. 3.1 shows the layers in the synthetic formation, which are as follows, starting at the Earth surface: a 100m thick weathered layer ($k = 500$ mD, $\phi = 0.1$, $L_m = 2.49 \times 10^{-10}$ A/Pa.m), a 300m thick sandstone layer ($k = 152$ mD, $\phi = 0.25$, $L_m = 1.30 \times 10^{-9}$ A/Pa.m), a 100m thick bounding shale layer ($k = 2$ mD, $\phi = 0.05$, $L_m = 7.16 \times 10^{-11}$ A/Pa.m) and the reservoir layer ($k = 152$ mD, $\phi = 0.25$) which is also 100m thick. The reservoir is bounded below by another shale layer of 100m thickness and then by sandstone to the base of the domain. Boundary conditions enforce no fluid or current flow normal to the Earth surface.

To verify the model the simulation described by Wurmstich & Morgan (1994) is repeated. As far as possible the same material properties are used throughout the domain, and the same fluid extraction rate (500bbl/day in the half space, 1000bbl/day total). Two fluid compositions are modelled, each filling the entire reservoir layer (between 500 and 600m depth). The first, a 1-phase model, assumes that the only fluid present in the pores is brine, while the second, a 2-phase model, assumes a 70% water saturation with the rest occupied by oil or gas. The streaming potentials measured at three monitoring wells 100, 200 and 1000m from the production well are shown in Fig. 3.2 and are very similar to those given by Wurmstich & Morgan. The higher coupling coefficient and resistivity associated with the 2-phase model increase the potentials measured at the 100m and 200m monitoring wells such that the two models can easily be distinguished from one another. A maximum streaming potential of approximately 4.3mV is measured at the 100m well with the 2-phase model, slightly less than the 4.5mV seen by Wurmstich & Morgan, but small differences in material properties (in particular porosities, which are not specified by Wurmstich & Morgan) may account for this discrepancy.

Continuing with the same lithological model, the approach of a water front toward the production well is modelled. The simplified model involves a fully oil-saturated reservoir, and an approaching flood front which

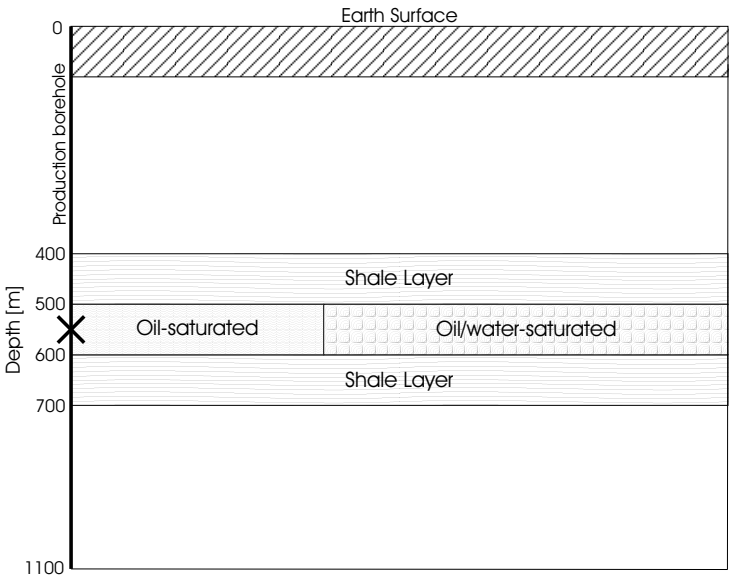

Figure 3.1: The synthetic reservoir model: the oil saturated reservoir is confined by two shale layers, which in turn are bounded by porous sandstone. The top weathered layer is at the Earth surface. The water front is an oil/water mix, and approaches the borehole on the left. The point of fluid extraction is shown by a cross.

is uniform throughout the thickness of the reservoir. The front is positioned at three locations, at 100, 50 and 25m from the borehole, in addition to models in which the reservoir is fully saturated with oil or water. These distances measure the length of a line joining the borehole to the nearest point of the front to the borehole, the boundary of the front being perpendicular to this line. The oil is considered to be anionic and therefore there is no electrokinetic effect when the only fluid moving through the pores is oil. Published results (Revil & Cerepi, 2004) from recent laboratory experiments confirm that the coupling coefficient does indeed fall to zero when the only flowing phase in the pores is oil. Further experimentation will be required to fully investigate the details of this assumption, for instance how much influence the exact type of oil (heavy or light) makes to the coupling coefficient. Previous publications (Jiang et al., 1998) have found non-zero oil-related coupling coefficients, but it is believed that the experiments of Revil & Cerepi (2004) are most similar to the conditions in the present modelling, and therefore these more recent data are used. Where the saturating fluid is an oil/water mix, $L_m = 1.30 \times 10^{-9}$ A/Pa.m. Fluid conductivities are $\sigma_{water} = 1.0$ S/m and $\sigma_{oil} = 0.0001$ S/m. Production is modelled by a spherical Gaussian function centred in the middle of the reservoir at 550m depth:

$$Q = -Ge^{-\left(r^2/l^2\right)}, \tag{3.14}$$

such that the total production rate is 500 bbl/day = 9.2×10^{-4}m^3/s.

The potentials measured at the borehole for the all-oil and all-water models are shown in Fig. 3.3. Where the reservoir layer is fully saturated with oil (Fig. 3.3a) it can be seen that the largest streaming potential is

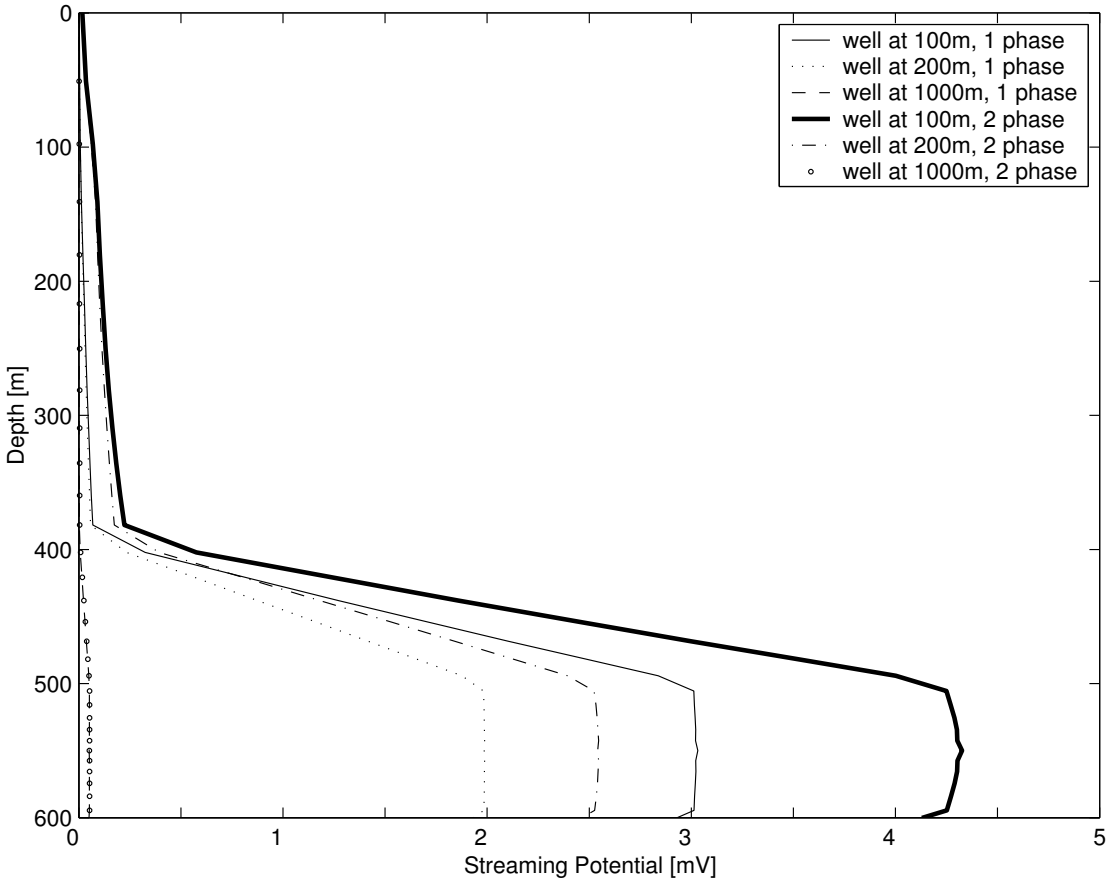

Figure 3.2: Streaming potentials measured in three monitoring wells for 1- and 2-phase flow, as described by Wurmstich & Morgan (1994). The higher coupling coefficient and increased resistivity of the 2-phase model gives larger streaming potentials, such that the presence of a hydrocarbon phase in the pores can easily be detected at the 200m well.

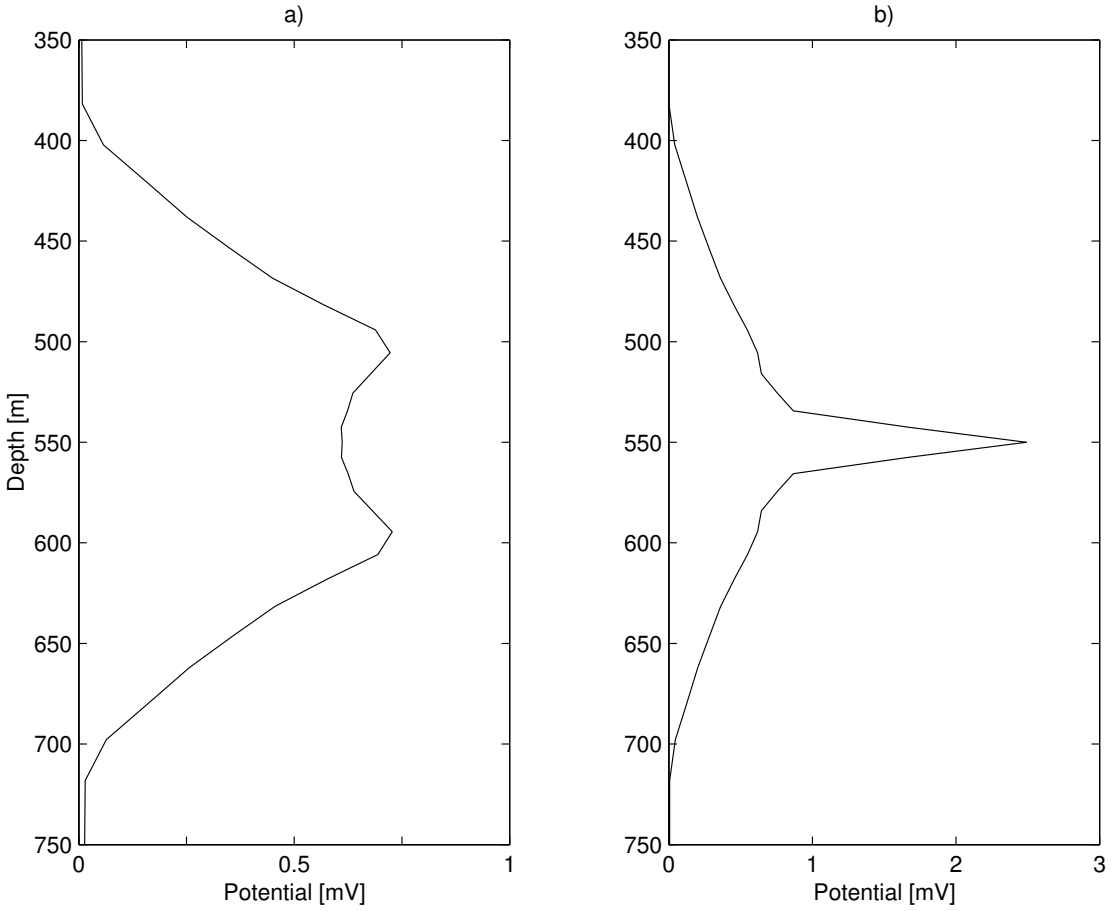

Figure 3.3: The results from modelling using the synthetic reservoir, $\sigma_{water} = 1.0$ S/m, $\sigma_{oil} = 0.0001$ S/m: streaming potential measured at the borehole for a) the all-oil model and b) for the all-water model. The presence of water in the reservoir is signified by an increased potential measured near the point of production (550m), and a drop in potential above and below the reservoir due to the rise in overall conductivity.

generated in the water-saturated bounding layers. Despite the small fluid velocities in these bounding layers, a measurement of roughly half a millivolt is made where the velocities are greatest, namely just above and just below the reservoir. By contrast the potentials measured for a water-saturated reservoir model (Fig. 3.3b) show the highest values at the level of production, 550m, decreasing above and below according to the decreasing fluid velocities. In addition to the increase in potential measured in the reservoir, there is also a significant decrease in the potential measured above and below the reservoir in the bounding layers, due to the increased conductivity of the reservoir fluid channelling current away. From this two observations may be made: that the presence of moving water in the reservoir will increase the streaming potentials generated, since the anionic nature of the oil phase allows no electrokinetic effect, and that the presence of water will also decrease the streaming potentials due to the increase in overall conductivity of the reservoir rock. Fortunately, these two phenomena exhibit themselves in different ways which may allow interpretation of streaming potential measurements. The increase in potentials with increased water saturation occurs where the oil phase is replaced with water, i.e. in the reservoir. The decrease in potential occurs where the saturating phase is already water, i.e. outside the reservoir or away from the region of production. In Fig. 3.4, streaming potentials measured at the borehole for the intermediate stages are shown, where the flood front is 100, 50 and 25m from the borehole. When the flood front is still far from the borehole the streaming potential is decreasing (Figs. 3.4a and b) due to the increasing conductivity, but when the front comes near to the borehole, in this case to a distance of 25m, the electrokinetic effect dominates and the streaming potential rises sharply right across the reservoir, from 500 to 600m.

3.4 Passive monitoring of a realistic reservoir

The geological model used is taken from an outcrop analogue at Book Cliffs, Utah, USA, (Hampson, 2000) in an area where a network of canyons allows near 3-dimensional mapping of clinoform geometries and lithofacies distribution. Fig. 3.5 shows the reservoir and the four lithofacies types: upper shoreface sandstones ($k = 3000$ mD, $\phi = 0.28$), proximal lower shoreface sandstones ($k = 40$ mD, $\phi = 0.24$), distal lower shoreface sandstones ($k = 4$ mD, ϕ=0.2) and offshore-shelf shales (full of water, $\phi = 0.15$). The reservoir measures 1080m x 510m x 44.88m with non-reservoir shale layers bounding above and below. To model the fluid distributions during production, petrophysical properties based upon those measured within the Rannoch and Etive units of the Brent field are allocated to each lithofacies. Production by line-drive water flood is simulated, with injectors located along the downdip side of the clinoforms and a single producer well, marked in Fig. 3.5 by a black line near the up-dip side of the reservoir. Extraction occurs from the surface of the reservoir to a depth of 32.5m. The finite-element mesh used to model this reservoir (Fig. 3.6) is refined around the borehole and coarsened in the far-field. In this and every model the mesh is designed in this way to ensure grid convergence and accurate representation of velocity and potential fields, while minimising the computational

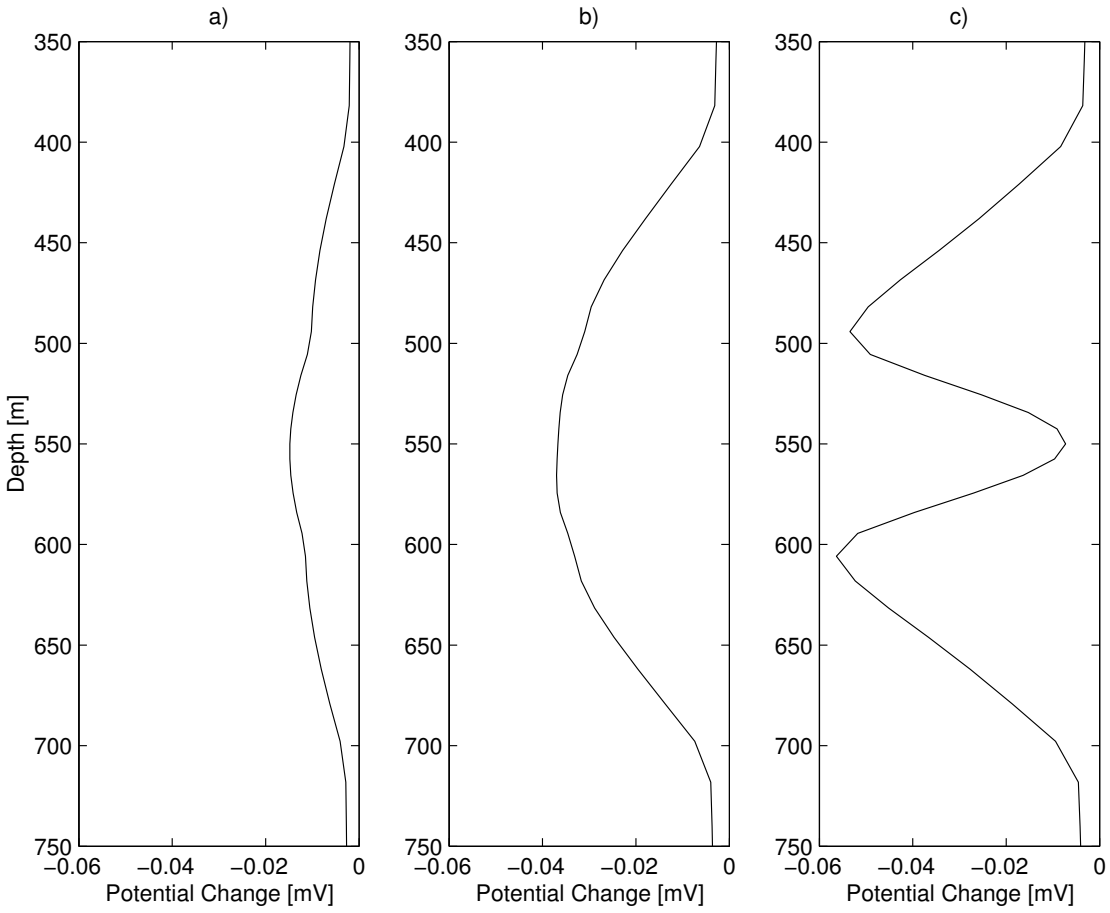

Figure 3.4: The potential changes at the borehole shown in detail for the three intermediate flood front models, using the synthetic reservoir, $\sigma_{water} = 1.0$ S/m, $\sigma_{oil} = 0.0001$ S/m. The flood front is a) 100m, b) 50m and c) 25m from the borehole, and the potential change is measured relative to the all-oil model. In a) and b) the presence of water in the reservoir is signified by a drop in potentials due to increased overall conductivity, but in c) the electrokinetic effect of the moving water dominates and the potentials increase in the reservoir.

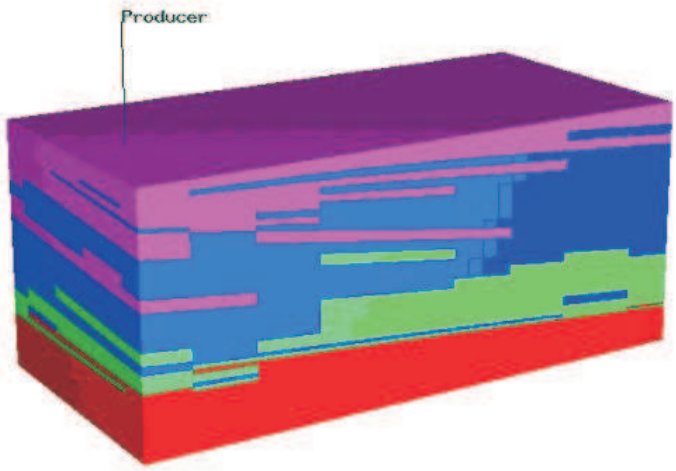

Figure 3.5: The reservoir model reconstructed from outcrop data from Book Cliffs, Utah, USA. The four lithofacies types are shown: upper shoreface sandstone (purple), proximal lower shoreface sandstone (blue), distal lower shoreface sandstone (green) and offshore-shelf shales (red). The location of the production borehole is shown. The dimensions of the reservoir are 1080m $\times$ 510m $\times$ 44.88m (vertical axis enlarged).

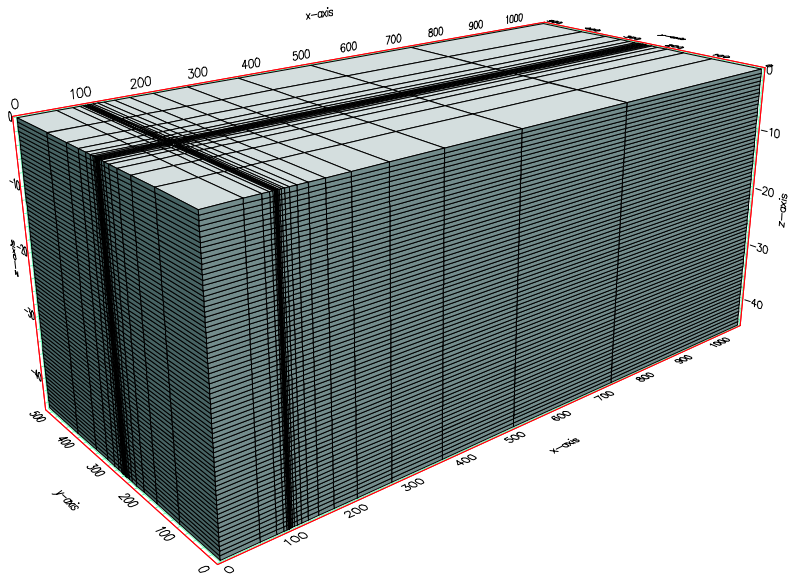

Figure 3.6: The finite-element mesh used for modelling the realistic reservoir. The mesh is refined around the production borehole, and coarsened in the far-field to reduce computational burden. The mesh contains 163800 volume elements and 173098 nodes. In this graphic the vertical axis is enlarged by a factor of 10.

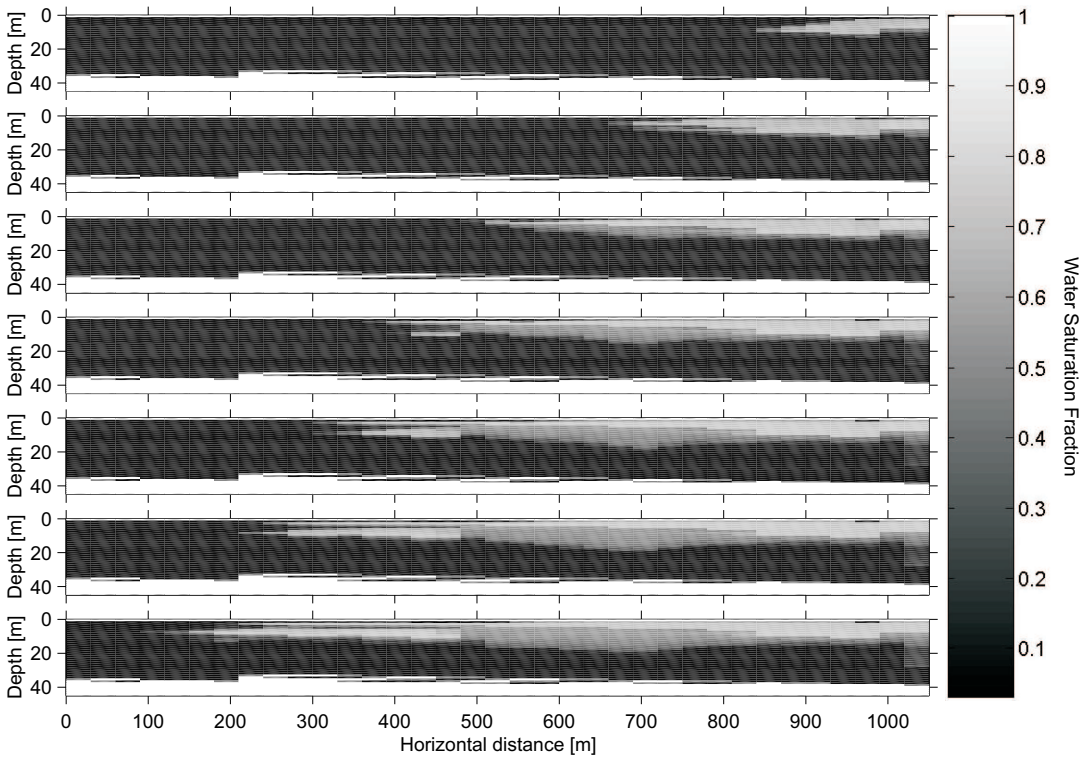

Figure 3.7: Water saturation fractions for the 7 fluid distribution models using a realistic reservoir. Water is injected at the right edge of the cross-sections shown, and production occurs at the borehole which is positioned at 105m on the horizontal axis. In the final model, bottom, the injected water has reached the borehole between 5 and 10 metres depth.

expense of calculating a solution. The fluid distributions are captured at 7 time intervals over a total period of 15 months (M. Jackson, private communication) and the fluid equations are solved for each distribution. Fig. 3.7 shows the 7 fluid distribution models in cross-section through the borehole (at 105m), with the flood front approaching and then reaching the borehole. An initial water saturation of 9% across the entire reservoir is due to immobile water in the pores, water which contributes to the conductivity of the rock, but not to the coupling coefficient (see Eq. 3.13). The shales at the base of the model are fully saturated with immobile water. In contrast to the synthetic model in which a point sink was used, an extended Gaussian distribution sink simulates production along the length of the borehole in the realistic model, and is given by:

$$Q = -G(z)e^{-\left(\left[(x-x_0)^2+(y-y_0)^2\right]/l_h^2+\left[z-z_0\right]^2/l_v^2\right)}, \tag{3.15}$$

with l_h small compared to l_v, and the multiplier $G(z)$ scaled to give a production rate of 10,000 bbl/day = 0.0184 m^3/s. Unlike the synthetic model above, this reservoir has a varying permeability profile along the length of the producing borehole. Therefore the multiplier $G(z)$ is adjusted along the length of the borehole to

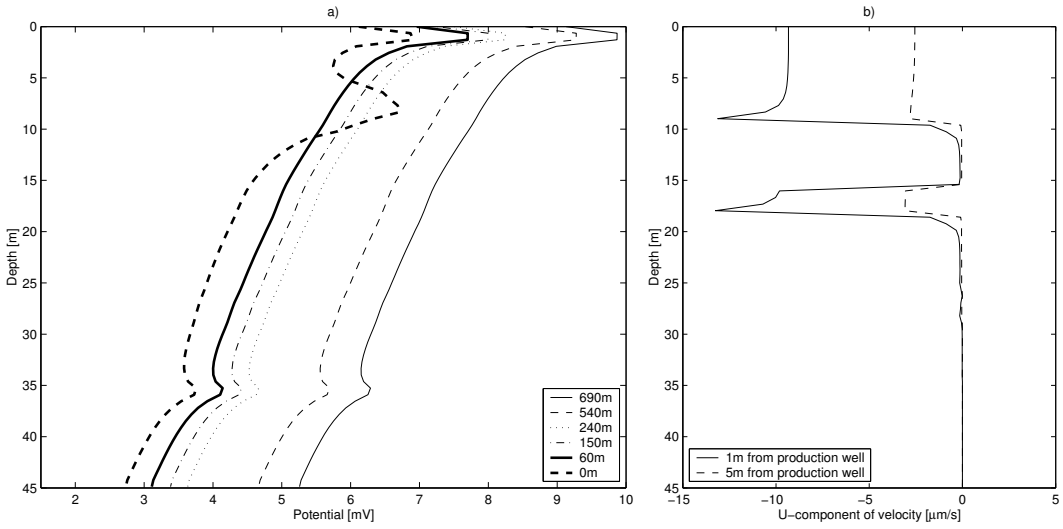

Figure 3.8: Results from modelling using the realistic reservoir model: a) potentials measured at the borehole for models with an approaching flood front at 690, 540, 240, 150, 60 and 0m away. As in the synthetic modelling, the potentials initially drop along the entire length of the borehole, then rise in the local vicinity of the water front layer. b) The fluid velocity profile at 1m and 5m from the production borehole.

ensure a uniform pressure, so that the more permeable zones produce more fluid than the lower permeability zones. The resolution of the finite-element mesh is increased significantly around the borehole to allow the sink to be modelled accurately.

Contrasting conductivities for the oil and water phases are used: $\sigma_{oil} = 0.0001$ S/m, $\sigma_{water} = 1.0$ S/m, and coupling terms: $L_{oil} = 0.0$ A/Pa.m, $L_{water} = 1.416 \times 10^{-8}\phi^{1.8}$ A/Pa.m. Boundary conditions enforce no normal fluid flow and no normal electrical current on any boundary except that at which the water is injected.

The potentials measured at the borehole, along with velocity profiles near the production borehole for this reservoir model are shown in Fig. 3.8, and are mostly similar to those from the synthetic model. As before, initially the potential drops, perhaps due to the increase in overall conductivity in the reservoir. The increase in potential at the final stage is local to the depth of arrival of the water front, between 4 and 12m, and signals that the proportion of water in the flowing fluid has increased significantly. The magnitude of the changes in potential is of millivolts, and therefore would once again probably be a detectable signal in the reservoir environment (Bryant et al., 2002). Other contributions to the self-potential, such as mineralisation, or redox potentials may be as large as a few hundreds of millivolts, but are expected to be quite stable in time (Telford et al., 1990, pg. 294).

Assuming that the final potential profile develops steadily as the water saturation near the borehole begins to rise, the changing potential may be monitored and the flow in the reservoir controlled before the water breaks through. The imminent arrival of the water is signalled by an increase in potential where the saturation fraction

is increasing, but also by a continued decrease in potential elsewhere. During production the flood front may advance by between one and two metres per day so there should be ample time to implement flow control procedures even if the water saturation were increasing within metres of the borehole.

3.5 Induced current

An additional tool available in an intelligent well is an active potential experiment, in which current is injected at the borehole. Measurements made by electrodes also at the borehole indicate the resistivity of the nearby formation and thus, potentially, the nature of the saturating fluid.

Using the geological data from the survey of Book Cliffs, Utah a conductivity profile for the entire reservoir is mapped on to the same finite-element mesh as before. The fluid distribution used is that of the penultimate model, in which the flood front is approximately 85m from the production well. Ideally a series of fluid distributions in which the flood front moved only a few metres at a time would be used for this modelling. The seven saturation models available, however, cover about 15 months and a distance of more than half a kilometre. An approximation to the ideal will therefore be made, by using a single fluid distribution model, and moving the position of the production well with respect to the flood front. The only drawback of using this approach is that the fluid flow is not truly converging on the position of the well, though by using the penultimate model the principal flow features such as high flow in the permeable layer and convergence towards the centre of the domain are included. The final fluid distribution is not used, as in moving the well away from the flood front it would approach the edge of the domain, potentially causing problems with the boundary conditions of the electrical problem.

In this experiment a current I is injected by a current electrode C_1 in the borehole and a measurement is made at a second electrode P_1 also in the borehole, at a distance a from C_1. The second current electrode C_2 and the second potential electrode P_2 which would appear in a Wenner or Schlumberger array are assumed to be remote from the experiment such that their influence is negligible. Thus the experiment can be regarded as current injection at a point source with potential measured relative to zero potential at large distances, and is described by the governing Laplace equation:

$$\nabla.[\sigma(\mathbf{r})\nabla\mathbf{U}(\mathbf{r})] = I\delta(\mathbf{r}-\mathbf{r}_{C1}), \tag{3.16}$$

where $\mathbf{U}$ is the resulting potential field and σ is the (possibly anisotropic) conductivity tensor.

The data measured by the potential electrode pair in the Wenner or Schlumberger array are resistivities ρ_a given by

$$\rho_a = \frac{4\pi\Delta V}{I}\frac{1}{\{(\frac{1}{r_1}-\frac{1}{r_2})-(\frac{1}{r_3}-\frac{1}{r_4})\}} \tag{3.17}$$

where $r_1 = \left|\vec{C_1P_1}\right| = a$, $r_2 = \left|\vec{P_1C_2}\right|$, $r_3 = \left|\vec{C_1P_2}\right|$ and $r_4 = \left|\vec{P_1P_2}\right|$ (Telford et al., 1990, pg. 650). Since

we place C_2 and P_2 remotely we have $r_2 = r_3 = r_4 \to \infty$, leaving

$$\rho_a = \frac{4\pi\Delta V}{I}a. \tag{3.18}$$

The units of ρ_a are therefore $\frac{[Vm]}{[A]} = [\Omega m]$ but ρ_a is not equal to the resistivity of the region between C_1 and P_1 unless the ground is homogeneous and isotropic. Since the domain is not homogeneous the term *apparent resistivity* is used which indicates that the data measured are not average resistivity values for the intervening zone, but are related to the actual resistivity to a certain extent. In practice it makes more sense, however, to think of the measured data not as resistivities, but as normalised voltages. Since Eq. 3.17 is linear the injected current can be set to $I = 1$A. The normalised potential $\frac{V}{I}$, which is the data measured by most resistivity instruments, does not then change even if the current required is larger or smaller than 1A. In the following text the normalised voltage data are referred to as potentials and the changing voltages between measurements as potential differences.

The current source $I\delta(\mathbf{r}-\mathbf{r}_{C1})$ is approximated on the finite-element mesh by a Gaussian distribution spread over a small number of nodes, and is scaled such that the total integral throughout the domain is equal to 1. It is expected that the potential measured near to the source will fall as the water saturation fraction, and therefore the conductivity of the rock, increases.

A cross-section of the the domain, showing the conductivity profile of the reservoir and therefore the fluid distribution, is presented in Fig. 3.9. The direction of fluid motion in this graphic is from right to left. Four borehole positions at which the current injection experiment will be modelled are shown by the vertical black lines at 180, 185, 190 and 195m. The shale layers bounding the reservoir above and below are filled with water and so have the highest conductivities. Note the step-like nature of the lower shale layer, which causes the reservoir to be thinner at the right-most borehole position, 195m, than at the other three. The main thrust of the flood front approaches the boreholes between 5 and 10m depth, with a secondary spur moving just beneath the upper shale but still some 25m from the nearest well position. The front itself is not particularly well defined, especially given the 30m horizontal resolution of the data. A linear interpolation is made between the given coordinates. In terms of water saturations, for this the penultimate model the maximum saturations at 180, 185, 190 and 195m are 12.9%, 18.8%, 24.6% and 30.5%, respectively, compared with an irreducible saturation of 9%.

In moving from 690m to 105m over the course of 15 months, the flood front travels at about 1.3m (4ft) per day. The four well positions therefore potentially give varying degrees of notice of the arrival of the flood front. If we define the critical saturation at 25%, then for the well positions at 190, 185 and 180m there would be about 0.5, 5 and 9 days before breakthrough, respectively. The flood front has already reached the well at 195m, so the greatest change in potential should be seen for this model.

The potentials measured along the length of the borehole, for each of the four borehole positions and using a 1m separation of the current and potential electrodes, are plotted in Fig. 3.10a. The change in potential between

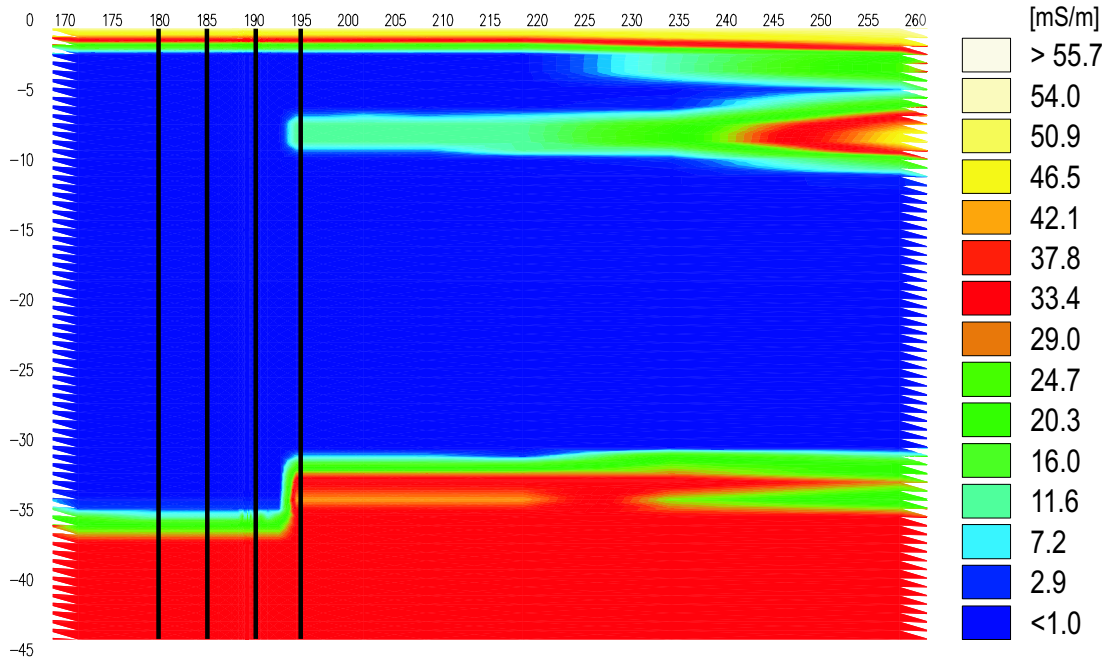

Figure 3.9: A cross-section of the reservoir showing the conductivity profile, and thus also the fluid distribution. The high conductivity shale layers bounding the reservoir above and below are fully saturated with water. The flood front approaches the four well positions, between 5 and 10m depth.

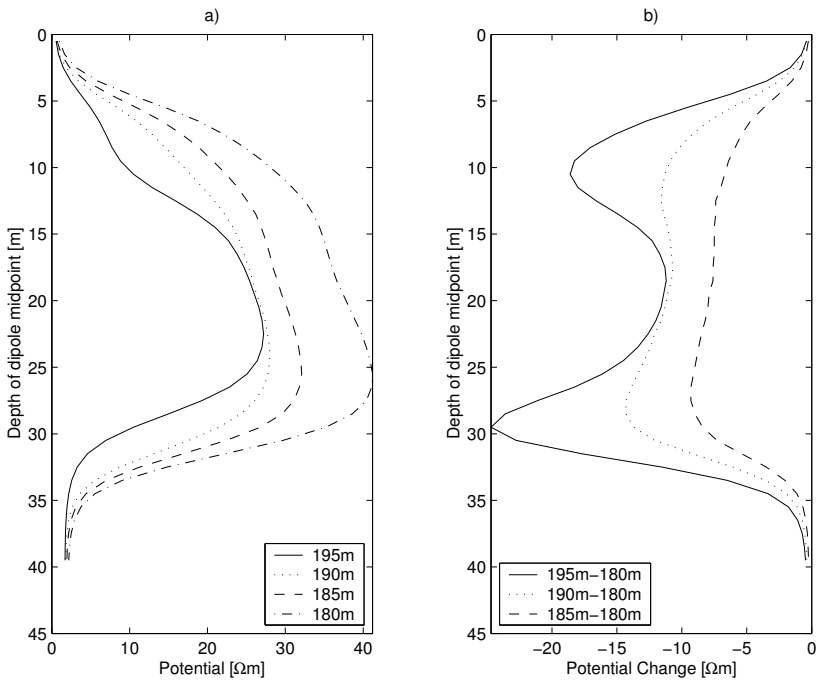

Figure 3.10: Results from the current injection experiment using a 1m spacing between current and potential electrodes: a) the potentials measured along the borehole showing the expected decrease as the flood front approaches and the resistivity of the reservoir falls, and b) the change between the potentials measured in the borehole at 180m and the potentials measured in the other three holes. The largest change is between the 180m well and the 195m, as expected.

the value measured in the borehole at 180m and the values measured in the other three are plotted in Fig. 3.10b. The potentials fall as the flood front approaches the borehole, and the measurement at 195m shows a larger decrease at around 10m depth due to the presence of the flood front. None of the other three curves in Fig. 3.10a show any apparent localised response to the approaching water at this depth. Inspection of the changes in potential (Fig. 3.10b) however, shows that the thin layer of water does affect the potentials measured in the borehole at 190m. The curve shows two negative peaks, one corresponding to the flood front layer, the other to the lower shale layer. The same is perhaps true of the data measured in the borehole at 185m, although there is no actual peak in the data above 25m, only a stationary point at about 15m depth. Electrical noise levels may be expected to be around 0.1mV/m for a 1A injected current (Bryant et al., 2002), so the results here would be viable in the field.

With a separation of 1m between the current and potential electrodes, the depth of penetration away from the borehole is expected to be less than 0.5m. In relation the water saturations at each location, these results therefore suggest that a 1m spacing is able to locate an increase in water saturation of between 13 and 19%.

The results from similar experiments in the same boreholes using electrode spacings of 8 and 15m are

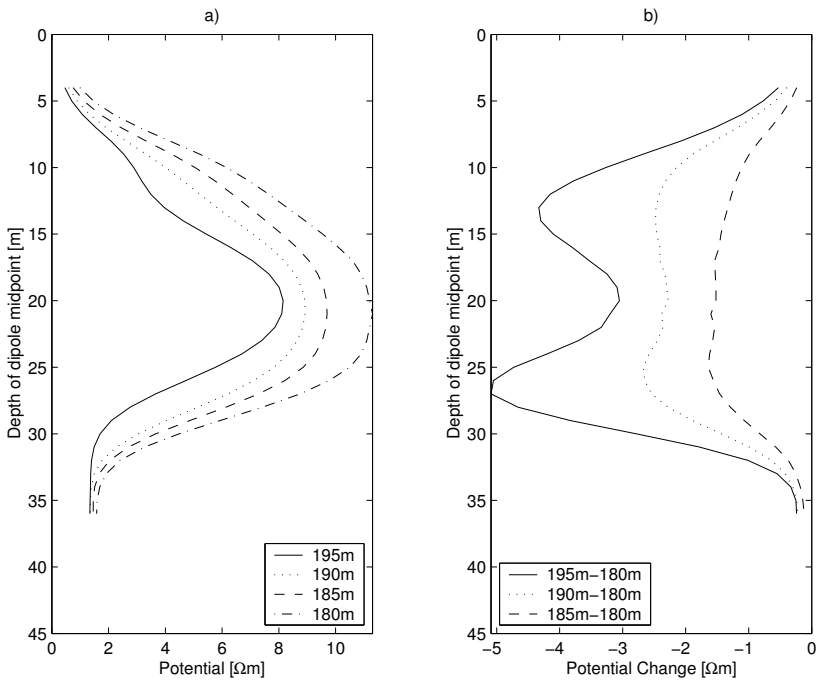

Figure 3.11: Results from the active experiment using a 8m separation between the current and potential electrodes: a) the potentials measured along the borehole, and b) the change in potentials compared to the measurements made in the well at 180m. The extra penetration does not significantly alter the measurements.

shown in Figs. 3.11 and 3.12, respectively. The reason for using a larger spacing is to increase the depth of penetration, and therefore perhaps to give more warning of the arrival of the flood front. The disadvantage is that in encompassing a greater extent of the domain, the recorded data is less well defined spatially. The minimum size of any anomaly which can be detected grows as the spacing is increased. Indeed, Fig. 3.11b using an 8m spacing closely resembles Fig. 3.10b in terms of the shapes of the data curves. The extra penetration depth is counter-balanced by the larger region of low-water-content, highly resistive rock through which the current passes. Increasing the electrode spacing to 15m (Fig. 3.12) worsens the situation further. Now it is not possible to make out that there are two distinct conductive regions, except perhaps in the borehole at 195m. There would be no hope of detecting an oncoming flood front of this thickness with such a large electrode spacing.

The results from modelling of the current injection method suggest that its viability as a tool in detecting water breakthrough at a production well depends on the thickness of any flood front layer which may approach the production borehole. As the thickness of such a layer increases, so does the maximum electrode spacing which will be able to adequately locate the layer. Therefore also the depth of penetration and the amount of advance warning available increase. Inspection of reservoir characteristic logs, especially those of permeability and porosity, may be useful in predicting the likely size of a flood front layer, from which a suitable electrode spacing can be chosen.

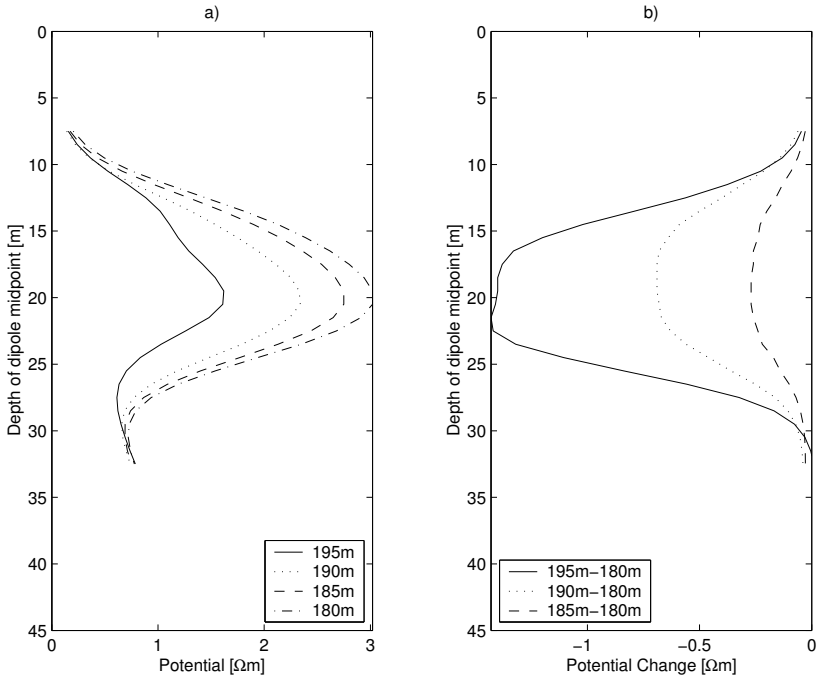

Figure 3.12: Results from the active experiment with a 15m separation between current and potential electrodes: a) the potentials measured along the borehole, and b) the change in potentials compared to the measurements made in the well at 180m. With a large spacing the vertical resolution is not sufficient to pick out the water front layer between 5 and 10m depth.

3.6 Discussion

Improvements to the models presented here may be made by making the material parameters more realistic and by using other techniques to improve the imaging and characterisation of the reservoir. For example, so far, identical values of viscosity for both the water and oil phases have been used. Varying these values and so making the displaced oil more or less mobile than the displacing water will affect the nature of the flood front. In the event of the oil being less viscous than the water, the flood front moves like a shock front, marking a sudden large increase in water saturation. If the oil is more viscous than the water a coherent flood front may not exist as the water flows in thin permeable channels towards the production well. In addition, 'monitoring' wells may be drilled, away from the production borehole in the direction of the oncoming water flood. Fluid flow at these locations would be slower, and thus potentials arising through electrokinetic coupling smaller. However, it might be possible to build up a better picture of the flow distributions using measurements in these boreholes, and therefore make a better calculation of the likely time of arrival of the water front at the production well.

The electrical inversion methods discussed in the previous chapter showed that knowledge of electrical potential distributions in a subsurface can be used to reconstruct an image of the geology including electrical conductivities and anisotropy. In the examples presented previously, electrical current is supplied artificially, usually by having twin boreholes, one containing electrical sources, the other containing receivers. However, it may be possible to regain such information by using the natural electric currents present in the subsurface due to electrokinetic coupling (Revil et al., 2004). This would be useful in contexts where deploying large amounts of electrical equipment is impractical or impossible. It could also be a useful addition to the 'flood front warning' system described here, as it would allow monitoring not only of fluid movement but larger scale rock movement and rock fracture development.

In the active experiment neither the borehole nor its metal casing were included in the model. The metal casing in particular will have a strong effect on the channelling of current, and so may make it more difficult to distinguish relatively small changes in conductivity in the surrounding formation. It would of course be necessary to position the electrodes outside the casing, and to prevent direct contact between the casing and the electrodes. The degree to which electrical and/or spatial isolation is necessary would be the subject of practical, possibly laboratory-based experiments.

3.7 Conclusions

Two methods deployable as part of intelligent well technology which may be used to detect the approach of the flood front to the borehole during production have been presented. In the passive experiment the streaming potential generated by moving fluid was measured, and the change in this potential signifying the changing composition of the pore fluid was monitored. The approach of the water front can be detected by electrodes at

the borehole. The characteristic signal is an initial reduction in potential along the length of the borehole due to the increased conductivity of the domain. This is followed by a localised increase in potential where the water begins to break through to the borehole, due to the increased coupling coefficient associated with the water phase. This method may give a strong indication of the imminent arrival of the flood front in sufficient time to allow fluid control procedures to be undertaken, and thus may be a viable tool in an 'intelligent' well. In the active experiment current was injected between two electrodes in the borehole, and a measurement was made of the resistivity of the formation near the borehole. Changes were noted as the reservoir oil was replaced by water in the pore space. This method may be capable of detecting the water front, depending on the thickness of the water layer and the electrode spacing. Large electrode separations increase the depth of penetration into the formation, but reduce the accuracy with which any changes in conductivity can be located. This method may also be a valuable addition to the technology in an 'intelligent' well, but the ability of the method to forecast the arrival of the water flood is limited by the lithology of the reservoir and the nature of the fluid flow.

Chapter 4

Wilfholme Landing - A Case Study

4.1 Introduction

The results of the previous chapter were all produced by numerical modelling of reservoir fluid flow and electrokinesis. This chapter is a description of field work undertaken at Wilfholme Landing in September 2003, and serves as a case study for electrokinetic/self-potential monitoring. This field work was carried out to determine the magnitude of the self-potential (SP) effect which might be measured in practice. The experiment consisted of an electrical survey which was performed in an attempt to measure the SP generated by water moving through the formation during pumping. In contrast to the work described in the previous chapter which involved measurement of the temporally changing streaming potential, the experiment discussed here involves only measurement of the steady-state SP. The purpose here is to show that an electric potential related to the flow of water through a chalk formation can be measured, and to determine an approximate value for the coupling coefficient in a chalk formation.

Investigations into self-potentials associated with groundwater flow (Fagerlund & Heinson, 2003; Marquis et al., 2002; Schiavone & Quarto, 1984) report measurements of the order of millivolts or tens of millivolts. Reynolds (1997, pg. 494-496) discusses the magnitude of the SP which may be measured in a variety of environments including mountain tops (where the SP may be of the order of volts), and in relation to the percolation of rain water (where the SP measured was around 5mV). An experiment similar to the one described here, in which groundwater was pumped artificially and in which an SP anomaly of tens of millivolts was measured, has been reported (Semenov, 1980). Therefore in this experiment a significant and recordable SP response can be expected. The SP experiment is described here, following a description of the location, geology and layout of the site.

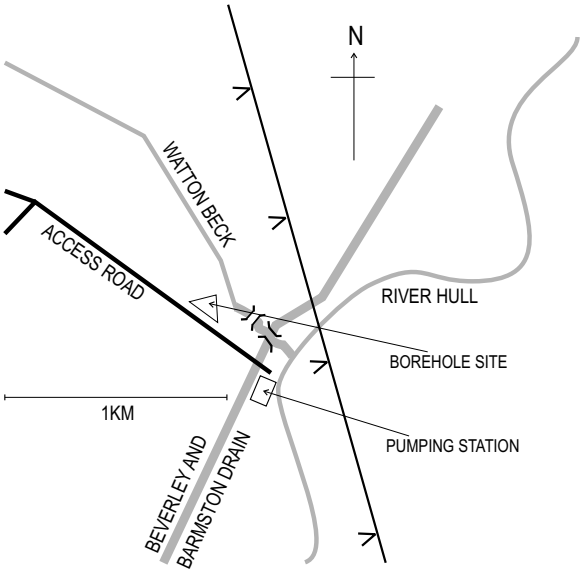

Figure 4.1: Location map for the Wilfholme Landing borehole site. The field site is situated at the junction of the Beverley and Barmston Drain with Watton Beck.

4.2 Site location, geology and layout

Wilfholme Landing is located between Beverley and Driffield, approximately 20km north of Kingston-upon-Hull, Yorkshire, UK, at grid reference (506180E,447180N) and at the junction of the Beverley and Barmston Drain with Watton Beck (see Fig. 4.1). The layout of four of the boreholes is shown in Fig. 4.2, where holes M1, M2 and M3 are the corner points of an equilateral triangle centred on hole P, each at a distance of 25m from P. The fifth borehole, M4, is 100m north-west of borehole P but is not used in these experiments. The drilled depth of each of the holes M1, M2 and M3 is 75m and each is cased in plastic to a depth of approximately 26m. Hole P is drilled to 80m and is cased in steel to a similar depth. The borehole diameters are 15cm with the exception of M3 which is 10cm in diameter. The near-surface geology consists of a thick homogeneous layer ($\sim$180m) of chalk underlying the top 15m of drift deposits. Thus the borehole casings extend over the drift layer and the weathered upper part of the chalk.

4.3 Measurements and results

4.3.1 Schedule of experiments

Over the three days of the site visit, and while air was injected into the central borehole P, self-potential (SP) measurements were recorded in one of the outer three boreholes. A full schedule of experiments is shown in Table 4.1.

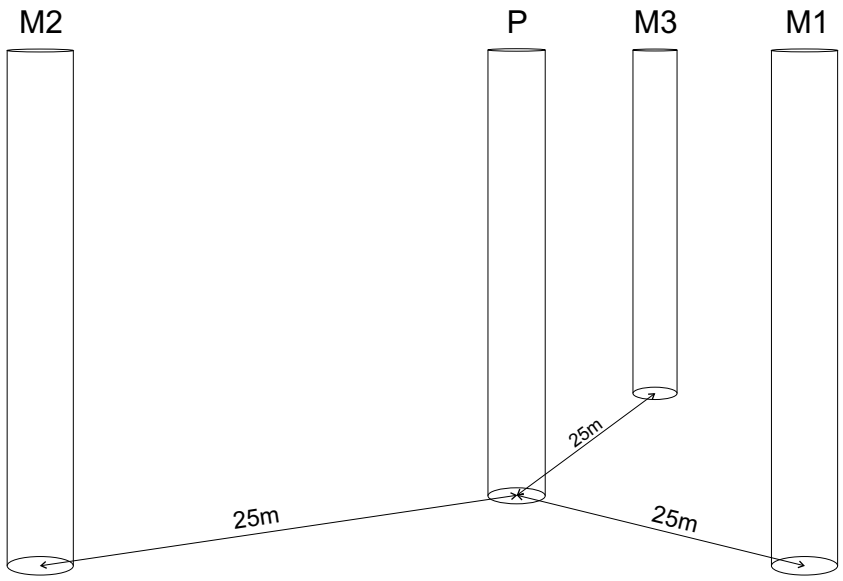

Figure 4.2: Diagram illustrating the layout of four boreholes at Wilfholme Landing. P is the centre point of the equilateral triangle with corners at M1, M2 and M3, such that the distance from each corner to the centre is 25m.

Date	Time	Borehole	Event
23 Sept	1433-1551	BH M2	Self-Potential
	1451-1522	BH P	Air injection at 42m
	1618-1842	BH M2	Self-Potential
	1630-1827	BH P	Air injection at 26m
24 Sept	1532-1658	BH M3	Self-Potential
	1556-1612	BH P	Air injection at 41m
25 Sept	0827-1032	BH M1	Self-Potential
	0847-0945	BH P	Air injection at 39m

Table 4.1: The schedule of experiments as conducted at Wilfholme Landing. Streaming potential experiments were carried out over three days, with measurements made in the outer boreholes, M1, M2 or M3, while air was injected in the central borehole, P.

Figure 4.3: Left: the packer tool used at Wilfholme Landing and connected plastic piping. The inflatable lower section of the tool is expanded to make a seal against the formation above and below the point where air is to be injected into the rock. Right: The packer tool being lowered into hole P.

4.3.2 Electrokinetic Monitoring

4.3.2.1 Experimental set-up and equipment

Data were obtained using the ABEM Terrameter SAS 300, in its passive mode to measure self-potentials. The Terrameter is able to calculate a running average over 4, 16 or 64 measurements, as well as taking a single measurement. A 16-point average was used which, with measurements taken every five seconds, gave a sample rate of 1 minute and 20 seconds. The water level in the boreholes was periodically recorded during the experiment using a dipper tool. The water level readings refer to the distance between lip of the borehole casing and the water surface. Therefore decreasing values denote a rising water level and vice versa. Observations were also made in the boreholes to record the presence of air bubbles, signifying that air injected in the central borehole had reached the outer holes.

The air-pump was connected to a borehole packer tool, positioned in the central borehole, P, by a length of plastic tubing (Fig. 4.3). The length of the inflatable part of the packer was 1m, ensuring that air was injected into a relatively thin layer of the formation. In the monitoring borehole an electrode, $P1$, was positioned at the same depth as the packer, and a second electrode, $P2$, placed at the Earth surface, offset from the monitoring borehole by about 0.5m. Lead electrodes were chosen to minimise polarisation effects; however these are still not at all ideal and, as the results show, significant drift was seen in the data.

4.3.2.2 Results from field experiments

As can be seen in Table 4.1, four SP experiments were conducted at Wilfholme Landing. In the first two of these, the monitoring borehole was hole M2, with the packer (and monitoring electrode $P1$) positioned at 42m depth and then at 26m depth. Holes M3 and M1 were used in the third and fourth experiments with the packer and electrode $P1$ at 41m and 39m depth, respectively. The SP and water level data from each of the experiments are presented in Fig. 4.4.

In Fig. 4.4b pumping appears not to affect the SP significantly. The water levels do rise, at about 5.5cm/hour, but even this rise is small compared to the changes seen in the other experiments and given the longer duration of pumping and recording. Air injection for this second experiment was at about 26m which is just at the bottom of the casing. Tracer tests (N. Odling, private communication) have shown that a high permeability zone between 25-30m depth connects holes P and M2 better than any of the other holes, through a number of relatively large channels. It is possible therefore that air may have been able to escape near hole P, perhaps through cracks in the casing cement or due to a poor packer seal against the rock. The results shown in Fig. 4.4b are puzzling, but the consistency of the other three experiments gives confidence that the method is on the whole reliable.

From Figs. 4.4a, c and d, however, it can be seen that initiating pumping in the central borehole has an immediate effect both on the SP measurements and the borehole water levels. Water level data in the first of these experiments are sparse, and it would be difficult to a make detailed analysis with only the SP data. Therefore only the measurements in holes M3 and M1 will be studied in more detail, while noting the similarities to both shown in Fig. 4.4a.

During the experiment when monitoring in borehole M3 (Fig. 4.4c) there were some difficulties with the air injection, evidenced by the short period of pumping. After only 5 minutes of injection at 41m depth a large amount of bubbling was seen in borehole P, suggesting that the packer seal against the formation had failed. The pumping rate was slowed, but only 7 minutes later it was clear that all the air being pumped was escaping in hole P and not being injected into the formation. The water level readings confirm this, as mid-way through the injection the water level in hole M3 dropped back toward the starting value at 86cm. The rebound pattern seen in the water level data is of hydrological interest as, combined with the quick response time of the levels to the pumping, it may imply that there are a number of fractures connecting holes P and M3 at around 40m depth (N. Odling, private communication). The SP readings for this experiment show that moving water in the fractures immediately begins to initiate a potential. Once pumping had stopped and, judging by the water levels, the fluids in the fractures had reached a static equilibrium, the SP curve regained a similar negative slope to that seen before pumping, in this case approximately -0.17mV/min.

In borehole M1 (Fig. 4.4d) a similar pattern in both the electrical and water level data can be seen. In this experiment, however, with injection into the formation at 39m depth the packer seal remained intact throughout

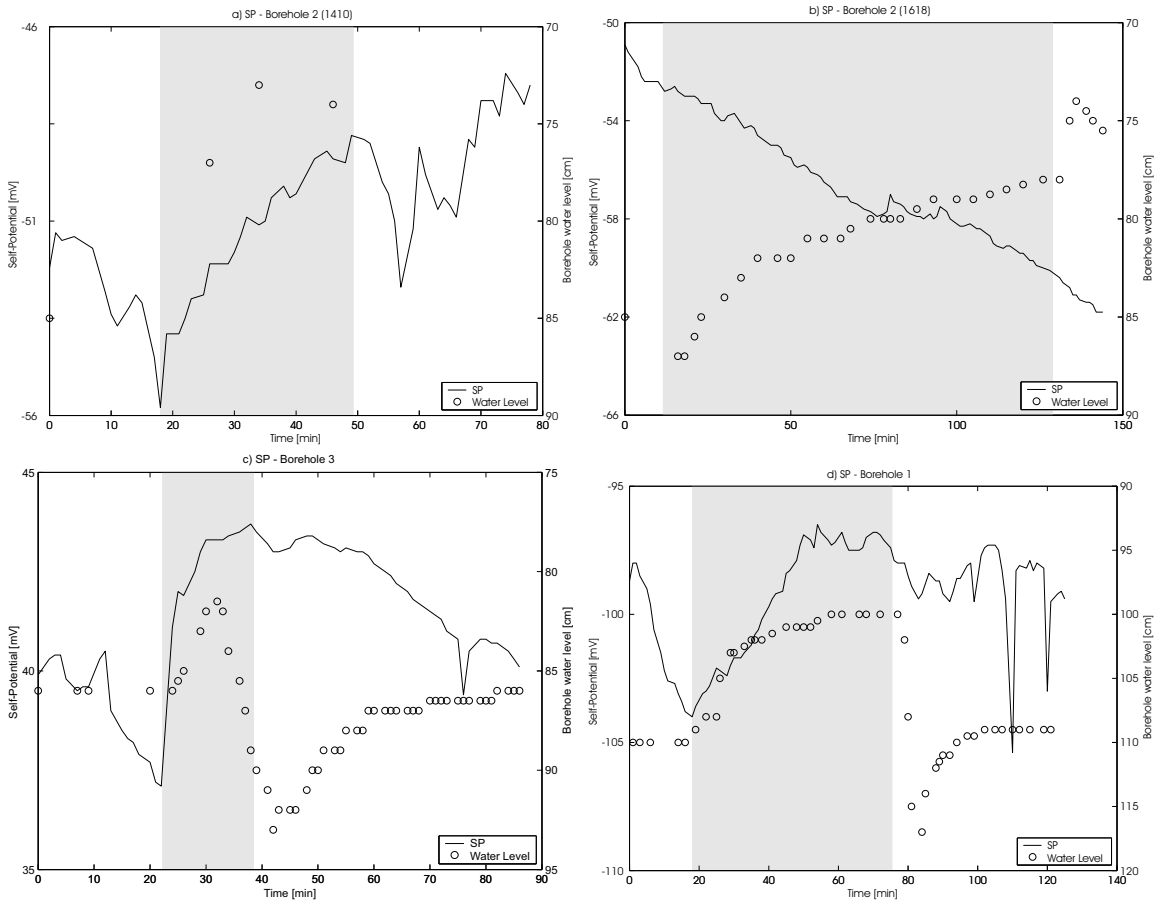

Figure 4.4: SP and water level data from a) and b) borehole M2, c) borehole M3 and d) borehole M1 at Wilfholme Landing during air injection. The grey shaded region covers the time when the pump was active.

nearly an hour of pumping. At the end of pumping the packer was released, and the rebounding effect in the water level readings was even more sharply defined and quicker here than in borehole M3. This may again suggest a well connected system of fractures linking boreholes P and M1. Another reason to believe that the fractures between holes P and M1 are well connected is the significant amount of bubbling observed in hole M1 during and after injection of air in hole P. Bubbles were observed after only 5 minutes of pumping, between 25 and 30 minutes into the experiment and again between 55 and 60 minutes. A brief period of bubbling after 70 minutes was followed by 20 minutes of bubbling after the pump was turned off, between 80 and 100 minutes. The early bubbling may have been due to air trapped in the fractures after the previous three air injection experiments. The bubbling which occurred later, during pumping, coincided with the flattening out of the water level curve so is more likely to have been due to the concurrent episode of pumping. The early change in SP was once again immediate, and was also of a similar magnitude to the change seen in hole M3, roughly 7mV.

4.4 Interpretation of results

If water were being injected into the central borehole and thus not changing the resistivity distribution, and if the injection were at a constant rate, a constant potential difference between the two electrodes should be measured. This streaming potential would be measured in addition to the self-potential measured between the two electrodes with no fluid flow. The data do not show a stable potential difference being established after pumping commences. This may be in part due to an unsteady injection rate, or to the changing constitution of the fracture-filling fluid. However at early times, in the first few minutes after pumping, the volume of air in the fractures was small (less than $0.3m^3$ after five minutes) and so approximated a water-injection experiment causing steady-state fluid flow but no change in bulk resistivity.

It will be assumed that the change in potentials seen in Figs. 4.4a, c and d are due to electrokinetic coupling. The immediacy of the response in the electrical data to the onset of pumping would seem to support this assumption. For verification, a model using a similar finite-element approach to that used in chapter 3 is set up. Permeability and porosity distributions are interpolated on to a finite-element mesh, and a steady-state flow model is created, simulating the injection of fluid at a given depth in a borehole. There will be a significant degree of uncertainty in many of the parameters in the modelling, so the aim will be simply to calculate the value of the coupling coefficient which gives a similar value of SP response to that seen in the field experiments, i.e. approximately 10mV.

The permeability distributions in the model are based on the work carried out at Wilfholme Landing by workers from the University of Leeds (Odling, Hartmann and West, personal communication). Inspection of a nearby cliff outcrop was also made by this group to estimate the likely porosity of the formation at Wilfholme. For the purposes of this modelling, the important conclusions of that work are the following:

- The chalk formation can be thought of as a dual-porosity medium,
- The chalk matrix has high porosity ($\phi \approx 25\%$), and low permeability,
- Fractures contribute approximately 1% to bulk porosity, but have high permeability.

More recent wireline logs carried out in borehole P at Wilfholme Landing gave porosity values around 5% along the length of the borehole. This latter figure may be more accurate as it was measured in the Wilfholme borehole, but both porosity values will be considered in modelling as the higher value is given as typical of the chalk formations in the area. This may be more appropriate for the inter-borehole formation which has not been affected by drilling.

The low fracture porosity means that a uniform porosity distribution of ϕ = 25% (or 5%) can be used as a good approximation in the model. The model is separated into discrete horizontal layers for the purposes of approximating the permeability distribution, based on packer flow experiments carried out in borehole M2 and borehole P by the Leeds group. Permeability data for the boreholes are unfortunately not available in a form compatible with the modelling. (The existing data are in units of m/day which requires knowledge of the applied pressure gradient, whereas the model requires permeability in units of mD or m^2.) Permeability logs from a borehole in fractured chalk located in the south of England (British Geological Survey via J. Singer, private communication) show core permeability between 1 and 10mD, and permeability from packer tests between 100mD and 1D. Reports of experiments conducted in a danish fractured chalk formation (Nygaard et al., 1998) describe matrix permeability values up to a maximum of 1mD and bulk permeability of the order of 10mD. The values to be used in the model are in the mid-range of these values. A low permeability of 0.01mD is given to the chalk matrix which will allow only a small amount of flow. Two layers of higher permeability (k=10mD) are found at 28-32m and 42-47m depth, and a layer of even higher permeability (k=50mD) is found at 32-37m depth. The layering of the synthetic permeability log to be used here is based on the log from borehole M2, and is shown in Fig. 4.5. Fluid conductivity was, unfortunately, not measured at the site at the time, but measurements of the fluid conductivity taken in well M1 in the Spring of 2002 were around 0.1S/m, and in well M3 up to 0.17S/m. A value of σ_{flu}=0.1S/m will be used initially in the modelling. The electrokinetic coupling term L is, as before in Eq. 3.11, given by

$$L = \frac{-\zeta\epsilon}{\eta}\phi^{1.8} \tag{4.1}$$

where ζ is the zeta potential, ϵ is the dielectric permittivity and η=0.001Pa.s is the fluid viscosity. The higher resistivity gives a larger zeta potential than before (see Eq. 3.12), so for this modelling we have ζ=-46mV, ϵ=7.08×10^{-10}Farad/m, and therefore:

$$L = 3.25 \times 10^{-8}\phi^{1.8}. \tag{4.2}$$

The model includes various details to mimic the situation at Wilfholme: two boreholes are explicitly modelled with 100% porosity and zero coupling coefficient, (virtually) impermeable layers are positioned in bore-

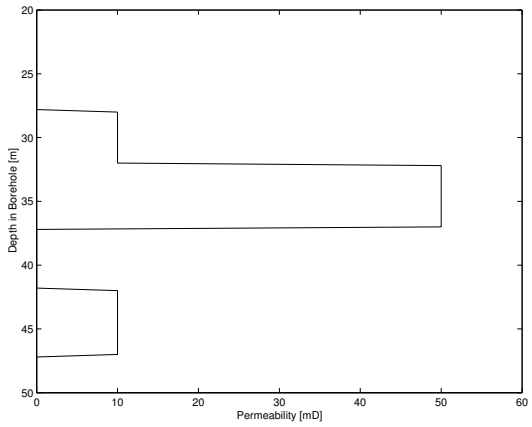

Figure 4.5: Vertical permeability profile used for modelling of the SP experiment carried out at Wilfholme Landing. The majority of the formation has low permeability equal to 0.01mD. Three permeable zones intersect the borehole, two with k=10mD, one with k=50mD.

hole P above and below the source to model the packer, and the integral of the source over the whole domain is equal to the injection rate of 1×10^{-3}m^3/s. In calculating the SP response to injection at the central borehole, the potential difference between an electrode in the monitoring borehole at 39m depth and a second electrode at the surface, offset by 0.5m from the monitoring borehole was measured.

The potentials measured along a line intersecting the two electrodes in the model are plotted in Fig. 4.6, for both the low and high porosity cases. The logs suffer a little from numerical noise, but it can be seen that the difference between the two models is small and thus the ambiguity in porosity may be discounted as a major uncertainty in the results. In either case, the potential difference between the borehole electrode (whose depth is shown in Fig. 4.6 by a dotted line) and the surface electrode is approximately 250mV. In Fig. 4.4 the magnitude of the SP associated with pumping as measured in boreholes M1 and M3 was of the order of 10mV.

These results may suggest that the modelling parameters were wrong, and that the fluid flow pattern in the fractures was considerably different to that represented in the model. However, the over-estimation of the SP in the modelling could be explained by the coupling coefficient being lower in a chalk formation than in sandstone, as well as by errors in the measurement of fluid conductivity. Using $\sigma_{fl} = 0.17$S/m together with a reduction of the zeta potential in the chalk by a factor of 10 to between -1 and -5mV would be enough to reduce the potential measurements to the same values. In this case the necessary value of the coupling term L would be adjusted from that given in Eq. 4.2 to:

$$L_{chalk} \approx 1.0 \times 10^{-9}\phi^{1.8}. \tag{4.3}$$

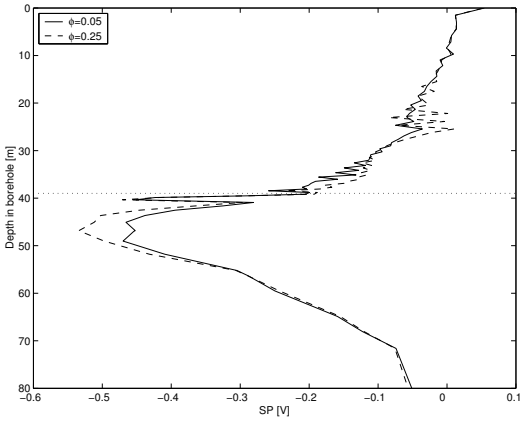

Figure 4.6: Potential measurements as if recorded by electrodes along a line intersecting the borehole and surface electrode for the low and high porosity models. The depth of the borehole electrode, 39m, is indicated by the dotted line, and the SP value recorded is the difference between the value at the surface and the value at 39m depth.

4.5 Conclusions

Measurements recorded in the field indicate that a significant self-potential is associated with the movement of water due to air injection. In three out of four experiments an immediate response to pumping was observed in both the SP data and in measurements of the water levels made in nearby boreholes. There will inevitably be some degree of drift in these data due to electrode polarisation effects, but this drift was difficult to anticipate and thus was disregarded. Modelling of these experiments has revealed that the coupling coefficient appropriate for electrokinesis in sandstone formations may be too large for this chalk environment. Allowing for the other uncertainties in the model, a reduction in the coupling coefficient by approximately one order of magnitude gives a better fit to the data recorded in the field.

Chapter 5

Borehole Electroseismics for formation characterisation - Theory

5.1 Introduction

Formation characterisation using borehole acoustic logs has been the subject of much interest and theoretical development over the last 50 years, since the theoretical papers of Biot (1956) and Biot & Willis (1957). Following these publications came a significant range of work focusing on particular aspects of the theory, and developing analytical solutions for particular cases (Rosenbaum, 1974; Tsang & Rader, 1979; Cheng & Toksöz, 1981; Astbury & Worthington, 1986; Tang et al., 1991). Analytical models for the propagation of elastic waves in a borehole and in the surrounding formation have led to an understanding of the effects of formation parameters, particularly porosity and permeability, and the influence of the frequency of the acoustic source on the attenuation and dispersion characteristics of the various wave modes (Brie et al., 2000; Burns, 1991; Liu & Johnson, 1997; Paillet, 1991; Tang et al., 1991). Experimental results by Winkler et al. (1989) support the dependence of Stoneley wave attenuation and velocity on frequency given by Biot theory. Current state-of-the-art borehole logging techniques include full waveform acoustic logs, which allow the determination of formation parameters such as porosity with some degree of accuracy and reliability.

Over a similar period the electrokinetic theory has been developed (Revil et al., 1999a; Haartsen et al., 1998; Jouniaux & Pozzi, 1995), and surface SP surveys have been used to monitor fluid flow in deep and shallow fractured formations (Marquis et al., 2002; Fagerlund & Heinson, 2003; Thompson & Gist, 1993). Wurmstich & Morgan (1994) modelled two-phase flow in a hydrocarbon reservoir and found that the potentials arising through electrokinetic conversion may be used to characterise the reservoir fluids. The theoretical development of the full poroelastic equations coupled to Maxwell's equations has been made by Pride (1994)

and Neev & Yeatts (1989). Revil et al. (2003) used this coupled set to monitor the movement of groundwater flow in a volcanic edifice, and noted that the technique may be used to detect the precursory electromagnetic signals associated with an eruption. Thompson & Gist (1993) discuss applications of electrokinetic conversion, particularly in shallow exploration of 'aquifers, cultural artifacts, or for pollution monitoring'.

In comparison with the theory of seismic wave propagation, however, the electrokinetic theory has received very little by way of experimental confirmation to date. The degree of uncertainty remaining in the theory, in particular in relation to the coupling coefficient and its value in any particular environment, means that at present we cannot be fully certain that it is applicable in a borehole logging situation in the presence of hydrocarbons and porous formations. However, encouragement can be taken from the studies of Zhu et al. (1999) who see strong Stoneley-related electric signals, and 'confirm that seismic waves in a borehole generate seismoelectric signals in the borehole formation which can be received by an electrode in the borehole's centre'. Mikhailov et al. (2000) also provide strong evidence that formation characterisation with borehole electroseismic methods is viable, finding correspondence between measurements of the normalised electric field (NEF) along the borehole and the fracture logs which signify high porosity and/or permeability. With the appropriate constraints, such as using low frequency seismic waves, the developing theory of steady-state electrokinesis can be used in conjunction with established seismic theory to investigate borehole electroseismic phenomena with some confidence. Therefore the model described here incorporates the current theory with the appropriate assumptions and simplifications, while further experimentation in the near future will aid understanding of the processes at work and give validation.

Since the ultimate aim is to solve 3-D problems with potentially complex internal structures it was decided to solve the equations numerically in the time domain. The main reason being that iterative solution methods were deemed necessary as they generally scale better (in terms of CPU cost per node) than direct solution methods for 3-D problems (Golub & van Loan, 1989). In the frequency domain (just like the reduced wave equation) the resulting matrix equations are poorly conditioned and difficult to solve using iterative solution methods (Stekl & Pratt, 1998).

For robustness, the equations are solved using implicit time-stepping methods. The unconditional stability and ability to suppress numerical oscillations of these methods is important as small elements may be necessary to resolve wave structures near interfaces, and time steps beyond unity grid Courant numbers (based on compression wave speeds, say) may be used. The time step size can then be chosen based purely on accuracy requirements. Finite elements are used here as they have the geometrical flexibility to allow both variable resolution (putting more resolution where required) and the ability to represent internal (defined by varying material properties) and external geometries of arbitrary complexity - important for the complex Earth. For numerical stability a mixed finite-element formulation is also used (Zienkiewicz & Taylor, 2000).

Since this model allows examination of the entire domain at a fixed point in time, or of a single point throughout the duration of the simulation, a full analysis of the several wave modes which are associated with

borehole seismics will be possible. The compressional, shear and Stoneley waves will be the most prominent, especially at low frequency (Astbury & Worthington, 1986), and it will be possible to investigate where these waves originate, and how and where they propagate. Depending on the properties of the formation and the source frequency, the pseudo-Rayleigh mode and the Biot slow wave may be observed, the latter being the mechanism which takes energy from the borehole Stoneley wave into the formation, and through which the Stoneley-related (streaming) potential is generated.

In this chapter a finite-element formulation is described which solves the Biot poroelastic equations coupled to a single electrokinetic conversion equation (a simplification of Maxwell's equations). First the governing equations are presented and all the necessary variables for the complete Biot poroelastic theory and the electrokinetic theory are introduced. It is shown how these variables relate to one another and to measurable parameters such as velocities and densities. Next the method is described by which the equations are discretised both in space and time. Finally some examples of the output are presented, showing the range of wave modes created in this environment and the various ways in which the data can be collected and manipulated. To validate the model, results are compared to example in the literature.

5.2 MAPEK: A mixed finite-element method for seismo-electrics

In this section the theory of generating electrokinetic streaming potential from seismic sources, and the modelling software, MAPEK (Modelling of Acoustics, Poroelastics and ElectroKinetics), which we use for this purpose are described. MAPEK uses implicit linear multi-step (LMS) time-stepping and a mixed finite-element formulation (with the stresses and displacements centred at different locations) to solve the Biot poroelastic wave equations in velocity form. An implicit time-stepping method has been used because of the strong coupling (which needs to be treated implicitly) between the solid and liquid phases of a typical porous medium in the Biot equations (Biot, 1956). This implicitness allows one to use consistent finite-element mass matrices, which helps achieve accurate solutions. The implicit method is also unconditionally stable which may be important for future applications involving small elements and unstructured (possibly adaptive) meshes. The resulting sets of linear equations are solved using preconditioned generalised minimal residual (GMRES) methods in which the preconditioner treats the inter-phase coupling implicitly. The set of linear equations for streaming potential are solved using preconditioned conjugate gradients (PCG). These solvers are highly efficient and allow the method to be applied in 3-D - the eventual aim. A mixed finite-element formulation has been used to circumvent the well known problems (Saenger et al., 2000) of non-zero shear wave velocity in the water phase in which the shear wave velocity should be zero. The unstructured finite-element framework allows complex geometries e.g. boreholes that deviate from a straight line or fracture geometries, to be easily represented numerically. Reflection boundary conditions are naturally applied using finite-element meshes, and open boundary conditions are modelled with the use of absorbing terms in the governing equations, which

damp out the wave motion near the boundaries. At each instance in time it is assumed that the streaming potential is at steady state. This is valid for low frequencies and allows one to dispense with the full Maxwell's equations and instead solve a Poisson equation for streaming potential.

5.3 Governing equations

There are two sets of equations: the multi-phase wave equations and the streaming potential equation. These are coupled allowing the streaming potential to react to solid and fluid velocity changes. In this section a summary of seismic wave theory is given, leading into the statement of the poroelastic wave equations due to Biot. Details relevant to the computational implementation of these equations, including boundary conditions, absorption terms and the calculation of material properties, are discussed. Then the streaming potential equation, similar to that presented in previous chapters, is presented, except now allowing for a non-stationary solid phase, followed by a description of the method used for simulation of a seismic source positioned in the borehole.

5.3.1 Poroelastic wave equations

A system of linear equations combining the mechanics of deformation together with acoustic propagation in a fluid-saturated porous medium has been presented by Biot (1956, 1962). This formulation is derived from the stress-strain relationships existing within both the solid and fluid phases, in addition to the coupling terms through which energy is transferred from one phase to the other. Such coupling occurs in two ways, primarily through a drag term b dependent on the relative motion between the fluid and the solid, and secondarily through apparent mass terms ρ_{ii} which account for the contributions of each phase to the total mass of the moving whole. These terms are extensively described by Biot (1956). The treatment as a whole is based on assumptions at the macroscopic level, and so a parameterisation of the heterogeneities occurring at the pore-scale is required. It is assumed here that wavelengths are long in comparison with the macroscopic elementary volume, that displacements are small, that the fluid phase is continuous and that the solid matrix is both elastic and isotropic. A restriction is also made to consideration of the saturating phase being a liquid, as a more generalised theory is required where the two phase densities are significantly dissimilar (Biot, 1956; Bourbié et al., 1987).

The result is a set of equations for both the water (acoustic) displacement $U = (U_r\ U_z)^T$ and solid (elastic) displacement $u = (u_r\ u_z)^T$. The equations in cylindrical coordinates are presented below.

5.3.1.1 Solids wave equation

The r-component of the solid phase poroelastic equation is:

$$\begin{aligned}&\frac{\partial}{\partial r}\lambda\left(\frac{1}{r}\frac{\partial r u_r}{\partial r}+\frac{\partial u_z}{\partial z}\right)+\frac{1}{r}\frac{\partial}{\partial r}r2\mu\frac{\partial u_r}{\partial r}+\frac{2\mu u_r}{r^2}+\frac{\partial}{\partial z}\mu\left(\frac{\partial u_r}{\partial z}+\frac{\partial u_z}{\partial r}\right)+\frac{\partial}{\partial r}\gamma\left(\frac{1}{r}\frac{\partial r U_r}{\partial r}+\frac{\partial U_z}{\partial z}\right)\\&=\rho_{11}\frac{\partial^2 u_r}{\partial t^2}+\rho_{12}\frac{\partial^2 U_r}{\partial t^2}+b\left(\frac{\partial u_r}{\partial t}-\frac{\partial U_r}{\partial t}\right)+\hat{W}_{mc}\phi\left(u_r-U_r\right)+q_s^d u_r+q_s^v\frac{\partial u_r}{\partial t}.\end{aligned}\tag{5.1a}$$

The z-component of the solid phase poroelastic equation is:

$$\begin{aligned}&\frac{\partial}{\partial z}\lambda\left(\frac{1}{r}\frac{\partial r u_r}{\partial r}+\frac{\partial u_z}{\partial z}\right)+\frac{1}{r}\frac{\partial}{\partial r}\mu\left(r\frac{\partial u_r}{\partial z}+\frac{\partial u_z}{\partial r}\right)+\frac{\partial}{\partial z}\left(2\mu\frac{\partial u_z}{\partial z}\right)+\frac{\partial}{\partial z}\gamma\left(\frac{1}{r}\frac{\partial r U_r}{\partial r}+\frac{\partial U_z}{\partial z}\right)\\&=\rho_{11}\frac{\partial^2 u_z}{\partial t^2}+\rho_{12}\frac{\partial^2 U_z}{\partial t^2}+b\left(\frac{\partial u_z}{\partial t}-\frac{\partial U_z}{\partial t}\right)+\hat{W}_{mc}\phi\left(u_z-U_z\right)+q_s^d u_z+q_s^v\frac{\partial u_z}{\partial t}.\end{aligned}\tag{5.1b}$$

5.3.1.2 Acoustic wave equation

The r-component of the liquid phase poroelastic equation is:

$$\begin{aligned}&\frac{\partial}{\partial r}\gamma\left(\frac{1}{r}\frac{\partial r u_r}{\partial r}+\frac{\partial u_z}{\partial z}\right)+\frac{\partial}{\partial r}R\left(\frac{1}{r}\frac{\partial r U_r}{\partial r}+\frac{\partial U_z}{\partial z}\right)\\&=\rho_{12}\frac{\partial^2 u_r}{\partial t^2}+\rho_{22}\frac{\partial^2 U_r}{\partial t^2}-b\left(\frac{\partial u_r}{\partial t}-\frac{\partial U_r}{\partial t}\right)-\hat{W}_{mc}\phi\left(u_r-U_r\right)+q_{fl}^d U_r+q_{fl}^v\frac{\partial U_r}{\partial t}.\end{aligned}\tag{5.2a}$$

The z-component of the liquid phase poroelastic equation is:

$$\begin{aligned}&\frac{\partial}{\partial z}\gamma\left(\frac{1}{r}\frac{\partial r u_r}{\partial r}+\frac{\partial u_z}{\partial z}\right)+\frac{\partial}{\partial z}R\left(\frac{1}{r}\frac{\partial r U_r}{\partial r}+\frac{\partial U_z}{\partial z}\right)\\&=\rho_{12}\frac{\partial^2 u_z}{\partial t^2}+\rho_{22}\frac{\partial^2 U_z}{\partial t^2}-b\left(\frac{\partial u_z}{\partial t}-\frac{\partial U_z}{\partial t}\right)-\hat{W}_{mc}\phi\left(u_r-U_r\right)+q_{fl}^d U_z+q_{fl}^v\frac{\partial U_z}{\partial t}.\end{aligned}\tag{5.2b}$$

The definitions of the material properties λ, μ, γ, R, ρ_{ij}, b, $\hat{W}_{mc}$, q_s^d and q_s^v are given in section 5.3.1.4.

5.3.1.3 Boundary conditions

The appropriate boundary conditions on planes of symmetry are no normal displacement and zero shear stress. The boundary conditions at the Earth surface are zero normal and shear stress conditions. Along the central axis in axisymmetric rz coordinates a zero normal displacement is specified. However, no information can cross such a boundary as it has zero surface area.

5.3.1.4 Material Properties

The parameters in the above equations relate to the basic material properties of the formation and the borehole fluid. Here they are defined them in terms of those properties, and their physical role is explained where relevant, following the notation of Bourbié et al. (1987). For the purposes of the present modelling, it is assumed that the characteristics of the formation are known, in particular the formation porosity ϕ, the formation permeability k, the fluid viscosity η, the solid compressional and shear velocities c_s^p and c_s^s, the fluid compressional velocity c_{fl}^p, the solid density ρ_s and the fluid density ρ_{fl}. Here, 'solid' (subscript 's') refers to the rock grains, as it were with zero porosity, while 'dry' (subscript 'o' for open) and 'saturated' (subscript 'f' for

formation) refer to the porous rock without and with the fluid filling the pores respectively. The subscript 'fl' refers to the borehole fluid which is identical to the pore fluid. The saturated bulk density ρ_f is then simply

$$\rho_f = (1-\phi)\rho_s + \phi\rho_{fl}. \tag{5.3}$$

The three density terms, or apparent mass coefficients, then follow:

$$\rho_{11} = \rho_f + \phi\rho_{fl}(a-2), \tag{5.4a}$$

$$\rho_{12} = \phi\rho_{fl}(1-a), \tag{5.4b}$$

$$\rho_{22} = a\phi\rho_{fl}, \tag{5.4c}$$

where the subscript 1 refers to the solid phase, 2 refers to the fluid phase, and a is the tortuosity. The first, ρ_{11}, denotes the effective mass of the solid phase moving in the fluid; the second, $\rho_{12} < 0$, is a parameter which couples the phases, and the third, ρ_{22}, is the effective mass of the fluid moving in the solid. The hydraulic permeability, or mobility is given by:

$$\mathcal{K} = \frac{k}{\eta}, \tag{5.5}$$

which leads to the parameter b, governing the level of inter-phase coupling:

$$b = \frac{\phi^2}{\mathcal{K}}. \tag{5.6}$$

For the purposes of obtaining a reasonable estimate of the bulk and shear moduli of the saturated porous rock, the compressional velocity of the formation (assuming adequate grain consolidation) can be found from the Wyllie time-average equation (Wyllie et al., 1956):

$$c_f^p = \left(\frac{\phi}{c_{fl}^p} + \frac{1-\phi}{c_s^p}\right)^{-1}. \tag{5.7}$$

Similarly, an empirical relation is used to define the shear velocity of the formation:

$$c_f^s = \frac{c_f^p}{\alpha(1+0.24\phi)}, \tag{5.8}$$

where $\alpha = \frac{c_s^p}{c_s^s}$ is the solid velocity ratio. The shear moduli are then defined as:

$$\mu_s = \rho_s c_s^{s2} \tag{5.9}$$

and

$$\mu_f = \mu = \rho_f c_f^{s2}. \tag{5.10}$$

The fluid has no shear wave and so also no shear modulus. The bulk moduli are defined as:

$$K_{fl} = \rho_{fl} c_{fl}^{p2} \tag{5.11a}$$

$$K_s = \rho_s c_s^{p2} - \frac{4}{3}\mu_s \tag{5.11b}$$

$$K_f = \rho_f c_f^{p2} - \frac{4}{3}\mu \tag{5.11c}$$

and

$$K_o = \frac{1 + \phi K_f(\frac{1}{K_s} - \frac{1}{K_{fl}}) - \frac{K_f}{K_s}}{\frac{1+\phi}{K_s} - \frac{\phi}{K_{fl}} - \frac{K_f}{K_s^2}}. \tag{5.11d}$$

It may be preferable to specify the shear and bulk moduli directly, in which case there is no need to calculate the compressional or shear velocities of the saturated rock. These moduli are then used to define the following:

$$\beta = 1 - \frac{K_o}{K_s} \tag{5.12}$$

and

$$M = \frac{1}{\frac{\beta-\phi}{K_s} + \frac{\phi}{K_{fl}}}, \tag{5.13}$$

of which the physical interpretations are described by Bourbié et al. (1987) and Biot & Willis (1957). Three of the four remaining parameters can be defined from the equations:

$$\lambda = K_f - \frac{2}{3}\mu + M\phi(\phi - 2\beta), \tag{5.14}$$

$$\gamma = M\phi(\beta - \phi) \tag{5.15}$$

and

$$R = M\phi^2. \tag{5.16}$$

Where we have all fluid then:

$$\phi = \beta = a = 1, \;\; R = M = K_{fl}, \;\; \mu = \lambda = \gamma = 0. \tag{5.17}$$

For a non-porous solid:

$$\beta = \phi = 0, \;\; M \to \infty, \;\; R = \gamma = 0. \tag{5.18}$$

The frequency dependence of material properties such as the permeability will not be included here. The transition frequency ω_t separating low-frequency viscous flow from high-frequency inertial flow is given by (Pride, 1994)

$$\omega_t = \frac{\phi\eta}{\alpha k \rho_{fl}} \tag{5.19}$$

and thus is of the order of kHz when $\phi = 0.1$ and $k = 1$D. For higher porosities or lower permeabilities, which may be more typical in reservoir conditions ω_t will be well above the range to be used in the present modelling. Inclusion of the full description of frequency-dependent material properties would be an important area for future research.

The last parameter, W_{mc}, is the impedance or stiffness of a zero-thickness mudcake layer along the wall of the borehole as described by Rosenbaum (1974) and Liu & Johnson (1997). If there is no mudcake ($W_{mc} = 0$)

then the borehole fluid moves the fluid in the formation easily, and moves the formation solid to a smaller extent. A stiff membrane along the borehole wall increases the movement of the solid phase and reduces the movement of the fluid phase, and this effect increases with greater stiffness as the mudcake layer is less able to flex into the pore space between the solid particles. The presence of mudcake therefore changes the relative movement of the solid and fluid phases in the formation. W_{mc} is reported to lie between 0 and 10 GPa/cm (Liu & Johnson, 1997). $\hat{W}_{mc}$ is used instead of W_{mc} in Eqs. 5.1 and 5.2 to convert the surface stiffness to a volumetric coefficient which acts in the local vicinity of the mudcake. A varying value of W_{mc} along the length of the borehole can be used to model other flow features, e.g. fractures.

5.3.1.5 Absorption terms

Absorption terms (non zero q_s^v, q_f^v) are used in the governing equations to damp out all wave motion near open boundaries. However care must be taken in choosing appropriate magnitudes of the absorption - too small and it will not damp out the wave motion - too large and it may reflect waves back into the domain of dynamic interest. A common solution to this problem is to exponentially increase the exponent according to the distance x to the boundary, that is $q^v = A_0(\exp(x_0 - x) - 1)$ where x_0 is the distance from the boundary that the q^v first has a non-zero value, so A_0 contains the Heaviside function. The parameter q^v is adjusted such that in the middle of the absorbing layer $\frac{\rho}{\triangle T} = q^v$ in which ρ is the density of the medium and $\triangle T$ is the time scale on which the absorption acts for a wave speed of c: $\triangle T = \frac{L}{c}$ where L is the width of the absorption layer. The wave speed c is taken as the maximum wave speed which is associated with solid compressional waves.

5.3.1.6 Pressure calculation

The (fluid) pressure p in the model is a diagnostic tool and so does not play an active part in the calculations above. However, the definition:

$$p = -K_{fl}\nabla.U \tag{5.20}$$

is used, and the pressure output from the model will be analysed as if it were hydrophone data in the field.

5.3.2 Streaming potential equation

The equations governing the coupling of the electric field $\underline{E}$ and the current density $\underline{j}$ to the solid and fluid displacements u and U are given by (Haartsen & Pride, 1997):

$$\phi(\dot{u} - \dot{U}) = \frac{k}{\eta}[-\nabla p + \omega^2 \rho_{fl} u + \underline{f}] + L_x \underline{E} \tag{5.21}$$

and

$$\underline{j} = L_x[-\nabla p + \omega^2 \rho_{fl} u + \underline{f}] + \sigma_f \underline{E}, \tag{5.22}$$

where ω is the source frequency and $\underline{f}$ is an applied body force acting on the fluid phase e.g. a buoyancy force. In the absence of external current sources, the coupling term $L_x\underline{E}$ can be neglected in Eq. 5.21 (Wurmstich & Morgan, 1994) and also $\nabla.\underline{j} = 0$. Thus:

$$\nabla.\sigma_f\underline{E} = -\nabla.L_x[-\nabla p + \omega^2\rho_{fl}u + \underline{f}] \tag{5.23}$$

from Eq. 5.22. Substituting the bracketed term in Eq. 5.21 into Eq. 5.23 then gives the equation for streaming potential for low frequency seismic oscillations:

$$\nabla.\sigma_f\nabla\psi = -\nabla.\frac{L_x\eta\phi}{k}(\dot{u} - \dot{U}) \tag{5.24}$$

in which ψ is the streaming potential and $\nabla\psi = -\underline{E}$. This is also the equation for streaming potential in steady flow problems in porous media (c.f. Eq. 3.5d), in which case $\dot{u} = 0$. The coupling coefficient $C_v = \frac{\zeta\epsilon}{\eta\sigma_{fl}}$, where ζ is the zeta potential and ϵ is the dielectric permittivity. Then $L_x = C_v\sigma_f$, in which the saturated rock conductivity σ_f for varying porosities ϕ is calculated with Archie's Law, that is $\sigma_f = \sigma_{fl}\phi^m$ with $m = 1.8$ (Wurmstich & Morgan, 1994). For a deeper understanding of the chemistry and physical processes involved in electrokinetics, the reader is referred to Revil et al. (1999a) and references therein.

5.3.2.1 Boundary conditions

The boundary conditions used here are zero potential at the far field boundary (all boundaries other than symmetry boundaries) and zero normal potential gradient at the Earth surface - modelling the interaction with the low conductivity air.

5.3.3 The Seismic Source

Although streaming potential is undoubtedly sensitive to porosity it may be that the signal strength is too low to be reliably measured. The linear nature of the equations allows normalisation of the maximum source displacement to some convenient value, e.g. 1m or 1mm, and multiplication of all the resulting displacements, pressures and potentials by the appropriate scaling factor when it comes to comparison with a field test. All results are in SI units.

A better characterisation of the source than velocity is the integral under the pressure of the source generated by the tool. That is:

$$\int_{\Omega_{cyl}} pdV = -M\int_{\Omega_{cyl}} \nabla.UdV \tag{5.25}$$

in which the subdomain Ω_{cyl} defines the region containing the source. For instance, if the source is a right cylindrical surface Γ_{cyl} of radius 0.05m with a maximum of unity (1m) normal displacement on the surface, then the maximum value of $\int_{\Omega_{cyl}} \nabla.UdV$ is

$$\int_{\Omega_{cyl}} 2\pi r\left(\frac{1}{r}\frac{\partial rU_r}{\partial r} + \frac{\partial U_z}{\partial z}\right)drdz = 2\pi\int_{\Gamma_{cyl}} r(n_rU_r + n_zU_z)drdz = 0.0471239, \tag{5.26}$$

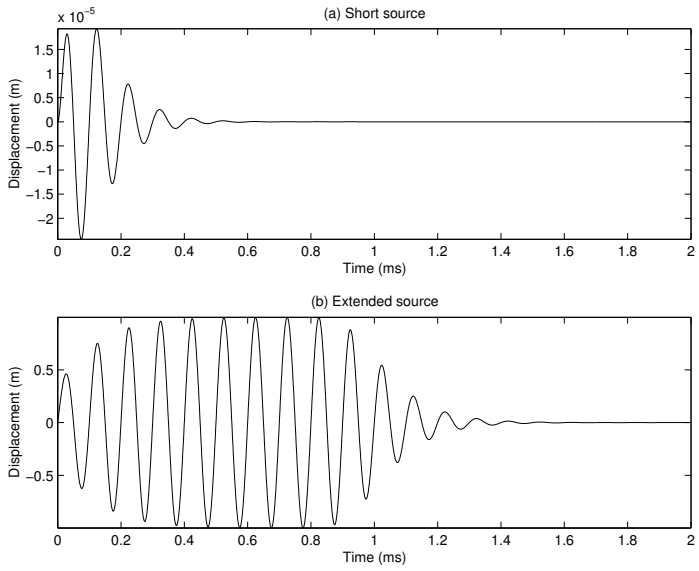

Figure 5.1: Two options for the source signature to be used in modelling. Trace (a) is the short source, described by Eq. 5.27 with A=1, B=15000 and C=2π*10000. Trace (b) is the extended source described by Eq. 5.28 with A=1, B=0.001 and C=2π*10000.

in which n_r, n_z are the components of the normal to the cylindrical surface. For example with the source in the borehole, and with $M = K_{fl} = 1200 \times 1630^2$ then the maximum pressure amplitude is 1.5024×10^8 Pa. If the maximum source displacement was 1mm instead, then the maximum pressure would be reduced by a factor of 1000. Being able to relate the source signature and maximum pressure in this way may be of benefit in the field, either for diagnosing the source displacement from hydrophone measurements, or optimising the source displacement depending on the sensitivity of the hydrophones.

The motion of the acoustic source situated in the borehole is defined by setting a boundary condition along the perimeter of the source. Two differing source signatures have been used, in which the displacement $x(t)$ of the source is given either by

$$x(t) = At\, exp(-Bt) sin(Ct) \tag{5.27}$$

which is called a 'short' source, or by

$$x(t) = A\, exp(-exp(-t/0.0001))(1 - exp(-exp(-(t-B)/0.0001)))sin(Ct) \tag{5.28}$$

which is the 'extended' source. An example of each source type is shown in Fig. 5.1. In each case, the amplitude of the source is principally governed by the scalar multiplier A, the duration of the source by B and the angular frequency by C.

5.4 Discretising the equations

In this section the spatial and temporal discretisation of the governing equations above is presented. For clarity, though with some loss of rigour, no distinction is made between numerical approximations and the exact solutions in Eqs. 5.1, 5.2, 5.20 and 5.24 for the dependent variables e.g. U, u, ϕ and p.

5.4.1 Spatial discretisation

Here the finite-element discretisation of both the poroelastic and streaming potential equations is described.

5.4.1.1 Mixed formulation for wave equation

A mixed finite-element formulation is used in which the stresses $\underline{\sigma}$ and strains $\underline{\epsilon}$ have a finite-element representation defined by the $\mathcal{M}$ basis functions Q_i, that is $\sigma = \sum_{j=1}^{\mathcal{M}} Q_j \underline{\sigma}_j$ and $\epsilon = \sum_{j=1}^{\mathcal{M}} Q_j \underline{\epsilon}_j$.

In axisymmetric coordinates part of the strain is

$$\hat{\epsilon} = \begin{pmatrix} \frac{\partial u_z}{\partial z} \\ \frac{\partial u_r}{\partial r} \\ \frac{u_r}{r} \\ \frac{\partial u_r}{\partial z} + \frac{\partial u_z}{\partial r} \end{pmatrix} = Su. \tag{5.29}$$

To help with the discretisation of the stress terms a matrix $\tilde{B}$ is defined:

$$\tilde{B}_i = \begin{pmatrix} 0 & N_{iz} \\ N_{ir} & 0 \\ \frac{1}{r} N_i & 0 \\ N_{ir} & N_{iz} \end{pmatrix}. \tag{5.30}$$

The matrix B is such that

$$B_{ij} = \int_{\Omega} Q_i \tilde{B}_j dV, \tag{5.31}$$

in which Ω is the solution domain.

The matrix $W_{\mu_{ii}}$ is defined as

$$W_{\mu_{ii}} = \begin{pmatrix} 2\mu & 0 & 0 & 0 \\ 0 & 2\mu & 0 & 0 \\ 0 & 0 & 2\mu & 0 \\ 0 & 0 & 0 & 2\mu \end{pmatrix}^{\frac{1}{2}} \tag{5.32}$$

- the off block diagonal terms in W_μ are zero, and

$$M_{p_{ij}} = \begin{pmatrix} \int Q_i Q_j dV & 0 & 0 & 0 \\ 0 & \int Q_i Q_j dV & 0 & 0 \\ 0 & 0 & \int Q_i Q_j dV & 0 \\ 0 & 0 & 0 & \int Q_i Q_j dV \end{pmatrix}. \tag{5.33}$$

Suppose

$$W_{\lambda_{ii}} = \frac{1}{\sqrt{3}} \begin{pmatrix} \lambda^{\frac{1}{2}} & \lambda^{\frac{1}{2}} & \lambda^{\frac{1}{2}} & 0 \\ \lambda^{\frac{1}{2}} & \lambda^{\frac{1}{2}} & \lambda^{\frac{1}{2}} & 0 \\ \lambda^{\frac{1}{2}} & \lambda^{\frac{1}{2}} & \lambda^{\frac{1}{2}} & 0 \\ 0 & 0 & 0 & 0 \end{pmatrix}, \tag{5.34}$$

and thus

$$W_{\lambda_{ii}}^T W_{\lambda_{ii}} = \begin{pmatrix} \lambda & \lambda & \lambda & 0 \\ \lambda & \lambda & \lambda & 0 \\ \lambda & \lambda & \lambda & 0 \\ 0 & 0 & 0 & 0 \end{pmatrix}. \tag{5.35}$$

All off block diagonal entries of W_λ are zero, that is $W_{\lambda_{ij}} = 0$ for $i \neq j$. W_γ and W_R are defined similarly to W_λ but with variables γ and R replacing λ respectively. Thus

$$M_p \underline{\epsilon} = (W_\mu^T W_\mu + W_\lambda^T W_\lambda) B \underline{u}. \tag{5.36}$$

Suppose the matrix H is defined:

$$H_\mu^{-1} = W_\mu^T M_p^{-1} W_\mu \tag{5.37}$$

and that the matrices G_λ, G_γ and G_R are defined:

$$G_\lambda^{-1} = W_\lambda^T M_p^{-1} W_\lambda, \tag{5.38a}$$

$$G_\gamma^{-1} = W_\gamma^T M_p^{-1} W_\gamma, \tag{5.38b}$$

$$G_R^{-1} = W_R^T M_p^{-1} W_R. \tag{5.38c}$$

The finite-element expansion for $U = \sum_{j=1}^{\mathcal{N}} N_j U_j$ and $u = \sum_{j=1}^{\mathcal{N}} N_j u_j$, where $\mathcal{N}$ is the number of finite element nodes used and U_j and u_j are the solid and liquid velocities in the numerical approximation centred on the node j. Multiplying the wave equation set (Eqs. 5.1 and 5.2) by the basis functions N_i, integrating the result over the domain of interest, and using the finite-element expressions for U and u and the matrices above, the following expression for the spatial discretised solid phase equations is obtained:

$$\begin{aligned} &-B^T G_\lambda^{-1} B \underline{u} - B^T H_\mu^{-1} B \underline{u} - B^T G_\gamma^{-1} B \underline{U} \\ &= M_{\rho 11} \frac{\partial^2 \underline{u}}{\partial t^2} + M_{\rho 12} \frac{\partial^2 \underline{U}}{\partial t^2} + M_b \left(\frac{\partial \underline{u}}{\partial t} - \frac{\partial \underline{U}}{\partial t} \right) + M_{q_s^d} \underline{u} + M_{q_s^v} \frac{\partial \underline{u}}{\partial t}, \end{aligned} \tag{5.39a}$$

and for the liquid phase:

$$\begin{aligned} &-B^T G_\gamma^{-1} B\underline{u} - B^T G_R^{-1} B\underline{U} \\ &= M_{\rho_{12}} \frac{\partial^2 \underline{u}}{\partial t^2} + M_{\rho_{22}} \frac{\partial^2 \underline{U}}{\partial t^2} - M_b \left(\frac{\partial \underline{u}}{\partial t} - \frac{\partial \underline{U}}{\partial t} \right) + M_{q_s^d} \underline{U} + M_{q_s^v} \frac{\partial \underline{U}}{\partial t} \end{aligned} \tag{5.39b}$$

in which the mass matrices $M_{\rho_{11}} = \begin{pmatrix} \hat{M}_{\rho_{11}} & 0 \\ 0 & \hat{M}_{\rho_{11}} \end{pmatrix}$, $M_{\rho_{12}} = \begin{pmatrix} \hat{M}_{\rho_{12}} & 0 \\ 0 & \hat{M}_{\rho_{12}} \end{pmatrix}$, $M_b = \begin{pmatrix} \hat{M}_b & 0 \\ 0 & \hat{M}_b \end{pmatrix}$ etc are defined by $\hat{M}_{\rho_{11}{}_{ij}} = \int_\Omega N_i \rho_{11} N_j dV$, $\hat{M}_{\rho_{12}{}_{ij}} = \int_\Omega N_i \rho_{12} N_j dV$ and $\hat{M}_{b_{ij}} = \int N_i b N_j dV$ respectively. Using $\underline{\mathcal{U}} = (u^T \; U^T)^T$ and collecting the matrices together in Eqs. 5.39a and 5.39b above, the resulting matrix equation set is:

$$\begin{aligned} A\frac{\partial \underline{p}}{\partial t} + B\frac{\partial \underline{\mathcal{U}}}{\partial t} + L\underline{\mathcal{U}} &= \underline{s}, \\ \frac{\partial \underline{\mathcal{U}}}{\partial t} &= \underline{p}. \end{aligned} \tag{5.40}$$

In the simulations conducted here four-node rectangular elements have been used with a full bi-linear variation of all velocity components defined by the basis N_i and a constant variation of the stress/strains throughout each element defined by the basis Q_i. The discretisation described here follows closely that used to solve the multi-phase fluids equations in Pain et al. (2000).

5.4.1.2 Mass matrices in the wave equation

The mass matrices in Eq. 5.40 and defined above with matrices M are distributed (consistent). However, although consistent mass matrices are used here they can lead to dispersive numerical solutions near abruptly changing material properties and as such options have been inserted into our model for lumping the various mass matrices so that they are diagonal and no longer distributed. In Eqs. 5.38 M_p^{-1} is generally a computationally unmanageable matrix unless M_p is diagonal (as with the use here of basis functions Q_i constant throughout an element) or block diagonal and when Q_i is represented by discontinuous elements. Alternatively, for numerical convenience if M_p is lumped it may be diagonalised with some loss of accuracy.

5.4.1.3 Streaming potential

Using the Galerkin weight residual method, multiplying the governing equation by the basis functions N_i, integrating over the solution domain using Green's theorem and expanding out the potential with this same basis $\psi = \sum_{i=1}^{\mathcal{N}} N_i \psi_i$ the matrix equation for streaming potential is obtained:

$$A\underline{\psi} = \underline{b}, \tag{5.41}$$

where the matrix A has coefficients $A_{ij} = -\int_\Omega \nabla N_i \sigma \nabla N_j dV$ and the right hand side vector $\underline{b}$ has elements $b_i = -\int_\Omega N_i \nabla . \frac{L_x \eta \phi}{k} (u - U) dV$ with similar finite-element expansions for the material properties and the wave displacements u, U. This equation has no time terms and requires no time discretisation. It is solved with an updated right hand side into $\underline{b}$ at every time step. The matrix A is positive-definite and thus Eq. 5.41 is solved using the Preconditioned Conjugate Gradient with a Forward Backward Gauss Seidel preconditioner.

5.4.2 Time discretisation of the wave equation

The implicit time-stepping scheme has a single parameter Θ unlike other methods such as the Newmark scheme (which has two parameters). Thus the parameter choice is relatively easy to optimise and understand. $\Theta = 1$ corresponds to Backward Euler time-stepping, $\Theta = \frac{2}{3}$ Galerkin with linear time elements and $\Theta = \frac{1}{2}$ corresponds to second-order Crank-Nicholson time-stepping. The important thing is that the second-order temporal accuracy is comparable to that of the second-order spatial discretisation used here. If higher order (than linear) elements like quadratic or spectral elements are used, then the accuracy of the time-stepping should be increased accordingly by extending the number of time levels over which the LMS method works.

The resulting time discretisation is:

$$\begin{gathered}\left(\frac{1}{\Theta\triangle t}A + B + \Theta\triangle t L\right)\underline{\mathcal{U}}^{n+1} = \left(\frac{1}{\Theta\triangle t}A + B - (1-\Theta)\triangle t L\right)\underline{\mathcal{U}}^{n} + \frac{1}{\Theta}A\underline{p}^{n} + \triangle t\underline{s}^{n+\Theta}, \\ \underline{p}^{n+1} = \frac{1}{\Theta}\left(\frac{\underline{u}^{n+1}-\underline{u}^{n}}{\triangle t} - (1-\Theta)\underline{p}^{n}\right)\end{gathered} \tag{5.42}$$

in which n is the time level and $\triangle t$ the time step size.

5.4.3 Possible finite-element pairs and stabilisation

Numerical oscillations associated with displacement modes and spurious fluid shear waves can be eliminated by careful choice of the element pair used to represent displacement and stress, see Zienkiewicz & Taylor (2000) volume 1. Appropriate finite-element pairs are also well known in the computational fluid dynamics literature (Gresho & Sani, 1998) and in this case are used to represent fluid velocity and pressure instead of displacement and stress respectively.

In this work rectangular elements with bi-linear displacement variations throughout each element and simple displacement continuity between elements are used. Stress has a constant variation throughout each element. There are still modes associated with this element pair particularly with the use of displacement boundary conditions resulting in a so-called checker-board mode (associated with zero eigenvalues of the matrix B above) and so-called pesky modes that manifest themselves in the form of oscillations covering a small number of grid points and associated with eigenvalues of $O(h)$ (h is the element length scale) or less in matrix B. However, in general this element (with bi-linear displacement variation and constant stress variation) does perform exceptionally well in practice (Gresho & Sani, 1998) and has the optimal ratio of the number of displacement nodes to stress nodes of about unity. A good alternative is the mini-element in which there is a cubic (for triangle or tetrahedral elements) or quadratic (for linear rectangular or hexahedral elements) additional bubble function inside the element for the displacements otherwise the displacements and stresses are represented with the same basis functions. Other alternative elements include various quadratic elements with a quadratic variation of displacement and linear variation of stress. In addition, from the structure and rank of matrices $B^T G_\gamma^{-1} B$, $B^T G_\lambda^{-1} B$ and $B_T G_R^{-1} B$ from Eqs. 5.39a and 5.39b (with Eq. 5.30), it can be

seen that for such a quadratic element, 4 times the number of stress nodes must be less than 2 times the number of displacement nodes.

The extra equations in the mini-element for displacement and associated with the centre of the element can be eliminated out of the equations resulting in a Petrov-Galerkin type of formulation. Thus Petrov-Galerkin formulations in general (using an upwind bias - upwind determined from the first-order form of the equations or from their characteristics/eigenvalues) result in stabilisation of the formulation. Riemann methods provide a similar method of stabilisation and can result in identical discretisations to Petrov-Galerkin methods. These methods are also very robust as they suppress spurious solution oscillations associated with inadequate spatial resolution. Space-time Petrov-Galerkin methods can also be effectively used here (Zienkiewicz & Taylor, 2000) as well as non-linear Petrov-Galerkin and Riemann methods (Donea & Huerta, 2003; LeVeque, 2002). However, if the waves can be resolved then Bubnov-Galerkin methods are generally more accurate than Petrov-Galerkin methods and are thus used here and stabilised with a mixed formulation.

5.4.4 Computation performance of the method

Symmetries are exploited in the near-borehole geometry to simplify the domain from 3D cylindrical coordinates to a 2D quarter-space (see Fig. 5.2). The mesh used in these examples is 6m tall and 2m wide, containing 61118 nodes and 61640 four-node rectangular elements. The memory overhead of this method is large since a number of large matrices for the implicit time-stepping need to be stored. Simulations are performed in double precision and in 180MB of core memory. If memory allows it would be desirable to increase the amount of storage further to accommodate a number of other large matrices which would circumvent the assembly of the matrix equations each time step - a substantial saving in CPU. However, this would require a factor of 2 to 3 increase in core memory which is not unreasonable.

The CPU time of a typical simulation is large partly for this reason, but more importantly because no attempt at optimising the performance of the iterative solvers is made. Simulations take approximately 30 hours to run on a Compac ALPHA ev6 833 MHz workstation, performing 3000 time steps with a time step size of 1×10^{-6}s. This time step size is chosen so that the maximum Courant number $\frac{\triangle t c}{\triangle x}$ is of the order of unity, where $\triangle t$ is the time step size, c the maximum wave speed and $\triangle x$ the finite-element characteristic length. Solutions become dispersive for significantly larger values of the Courant number (e.g. of the order of one hundred), and while values smaller than unity give an improvement in the solution accuracy, especially the resolution of higher frequency features, the small change in the solution is not enough to justify the considerable extra computation time required. A saving of up to 40% in computation time may be made by decreasing the solution tolerances by 3 or 4 orders of magnitude in a simple formation geometry at low frequency without affecting the results. High frequency sources and 3-D modelling are expected to be computationally demanding so the parallel computing options (which exploit domain decomposition solvers) in the code will be exploited in further such studies.

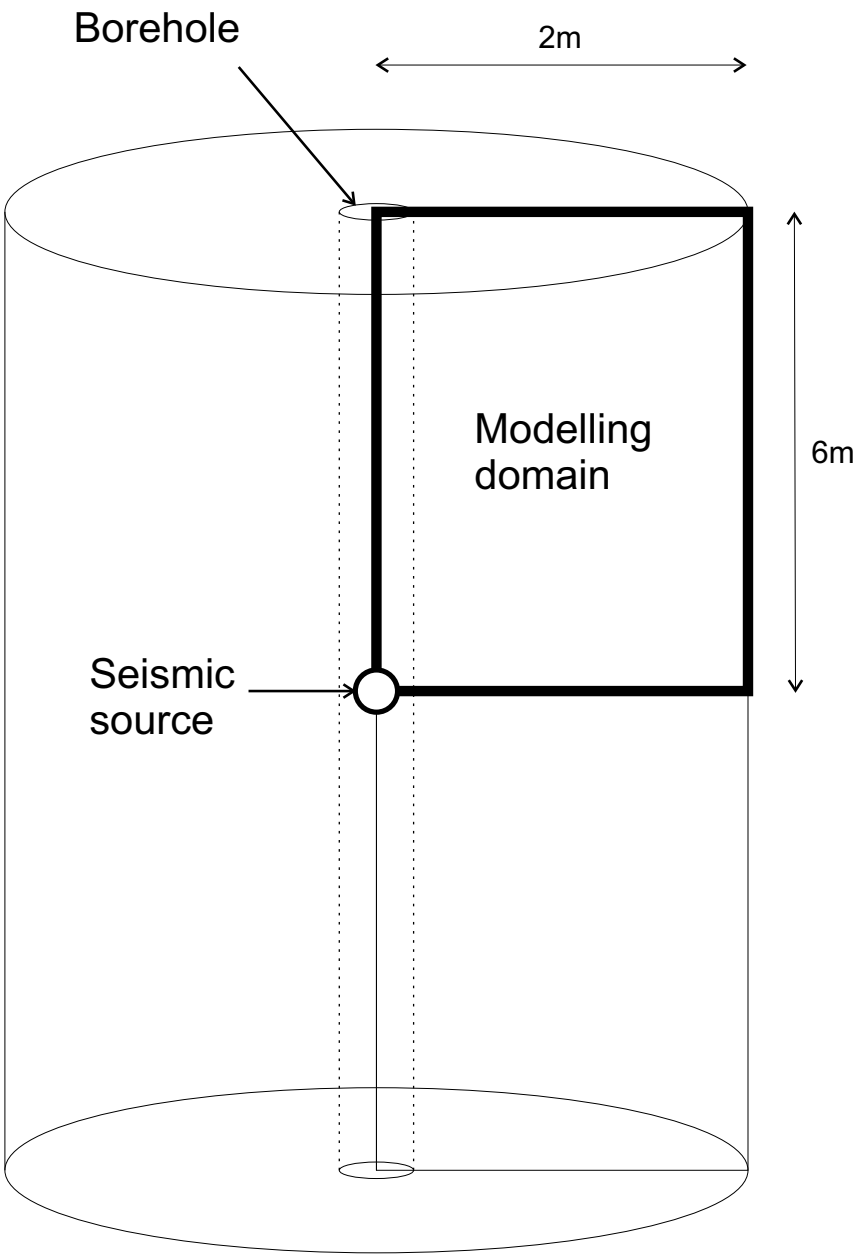

Figure 5.2: A schematic diagram (not to scale) showing the cylindrical geometry of the borehole region. The seismic source is positioned centrally in the borehole. Azimuthal symmetry (around the borehole) and vertical symmetry (above and below the source) allow modelling of only the 2D region shown by the heavy outline. In this reduced domain the source is represented by a quarter circle in the lower-left corner. The modelling domain in the examples shown here extends two metres from the central axis of the borehole and is six metres in height. The finite-element mesh is most refined along the borehole wall, and is progressively coarsened toward the top-right corner of the domain to reduce the computational burden.

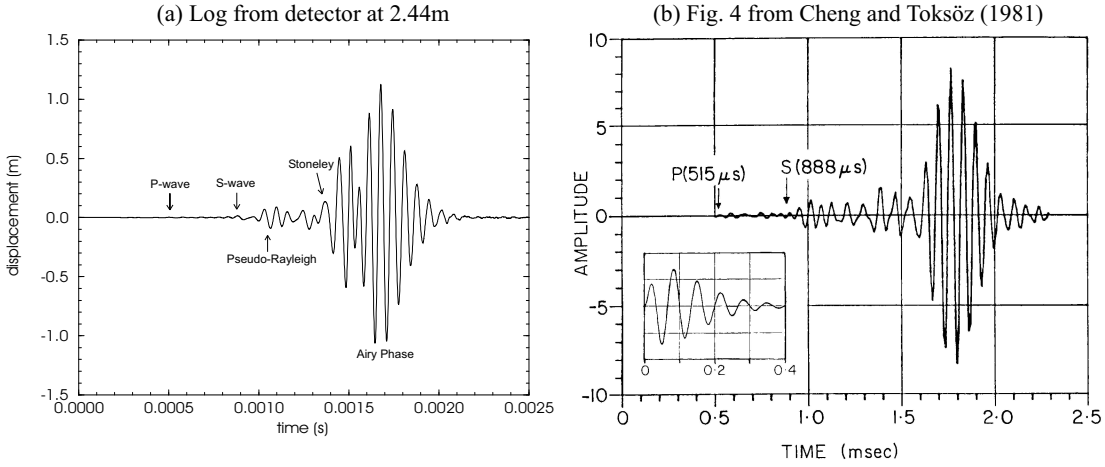

Figure 5.3: (a) A log from a borehole detector showing the vertical displacement. Five wave modes can be identified (see text), and this result is compared to (b) which is a reproduction of Fig. 4 from Cheng & Toksöz (1981) using the same formation and fluid parameters.

5.5 Examples

The results of some simulations run using MAPEK are presented in this section. In the first example formation and source parameters similar to those used by Cheng & Toksöz (1981) are employed (ρ_f = 2300 kg/m^3, c_f^p = 5940 m/s, c_s^s = 3050 m/s, ρ_{fl} = 1200 kg/m^3, c_{fl}^p = 1830 m/s, 'short' source frequency = 15 kHz with B=15000 and borehole radius = 0.1 m) to validate our model. The formation in this example is non-porous and impermeable. In Fig. 5.3a the displacement in the borehole as measured by a detector (e.g. geophone) at 2.44m distance from the source is shown, and compared to Fig. 4 in Cheng & Toksöz (1981), reproduced here for convenience as Fig. 5.3b. Note in Fig. 5.3a the small p-wave arrival at around 0.5ms and the larger shear wave around 0.9ms, and also note the later wave packets which Cheng & Toksöz identify as the pseudo-Rayleigh, the lower frequency Stoneley and finally the largest arrival, the Airy phase of the pseudo-Rayleigh wave between 1.6 and 1.9ms. The wave forms are not identical as the arrival after 1.5ms is larger in our simulation than in the analytical model. This may be in part due to the different borehole radii (Cheng & Toksöz use a radius of 0.102m), or that in calculating the microseismograms Cheng & Toksöz do not take account of the elasticity of the formation which is included in our model. However, the otherwise excellent match validates MAPEK against the analytical model.

Next, results from a simulation in which the formation surrounding the borehole is porous ($\phi = 0.3$) and permeable ($k = 1mD$) are shown. The source is the 'short' type again, with a frequency of 10 kHz and $B = 15000$ as in the first example. Fig. 5.4 shows the displacement and potential measured at a detector 2.45m from the source in the borehole. The principle difference between these logs and the displacement logs

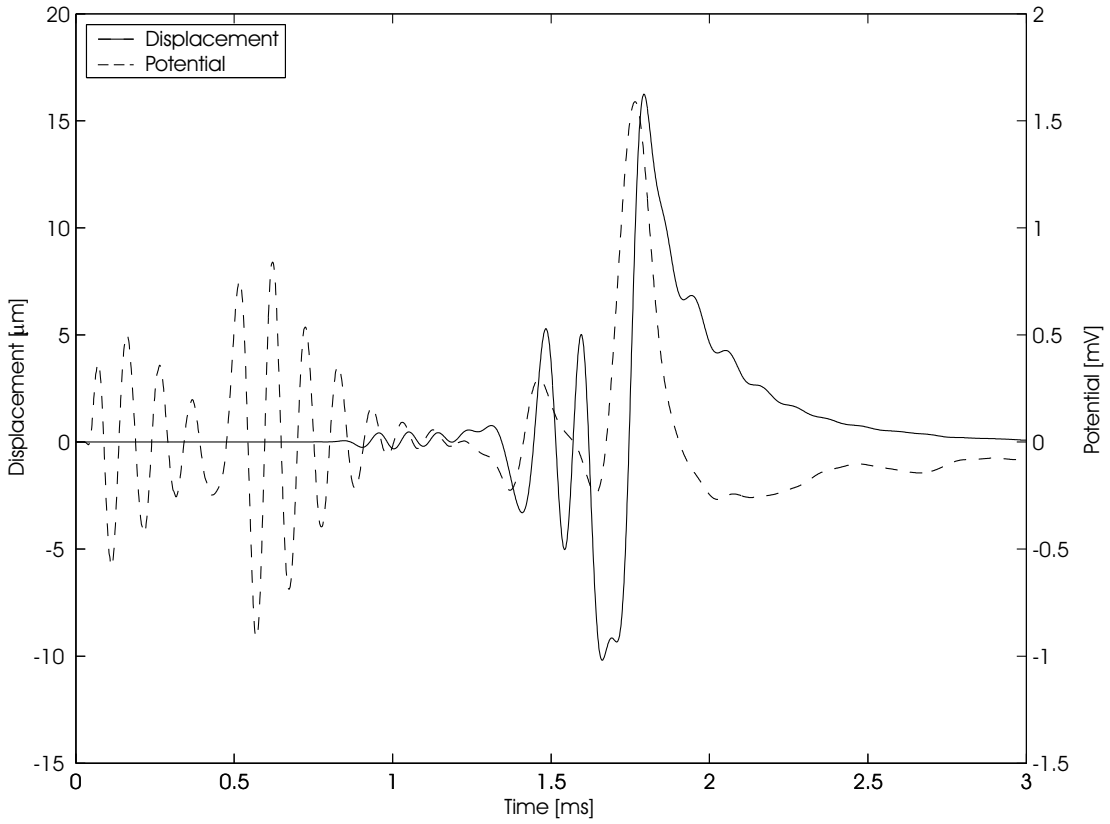

Figure 5.4: Borehole displacement and potential logs measured by a detector 2.45m from the source in the borehole. The formation surrounding the borehole in this example is porous and permeable. The potential signals occurring before 1ms are due to events near the source which cause propagating electrical waves throughout the domain.

in the previous example is the prominence of the Stoneley wave, which is seen at around 1.8ms in both the acoustic and electrical logs. The alteration in the relative sizes of the Stoneley and pseudo-Rayleigh waves is due to the lower frequency source used in this example. The cut-off frequency for the pseudo-Rayleigh mode with a borehole of this diameter (0.1m) is around 9kHz (Astbury & Worthington, 1986), while the Stoneley wave is expected to be excited more at lower frequencies. While there is some potential seemingly related to the pseudo-Rayleigh wave and perhaps the shear wave, the clearest signal is related to the Stoneley wave, with a peak of about 1.5mV for a displacement of around 10μm. In the potential log electrical signals from nearer the source are seen, which propagate infinitely fast through the domain and arrive at this detector during the first millisecond of the simulation. These propagating waves, which are seen at all detectors, are due to the first impact of the fluid compressional wave on the borehole wall and the relative fluid/solid motion in the compressional slow wave which is generated by conversion at the borehole wall.

A third example shows the response to a low frequency, 1kHz source. The formation surrounding the borehole has a porosity $\phi = 0.3$ and a permeability $k = 100$ mD. A complete list of formation and fluid properties is given in Table 5.1, along with the values of the principal coefficients in the Biot equations. The duration of the model is 3ms with a time step of 1×10^{-6}s. The seismic source signature is the 'short' source Eq. 5.27, with $A = 0.7364$, $B = 15000$ and $C = 2\pi \times 1000$. This set-up allows the source to complete one half cycle at 1kHz, although it is not an entirely clean signal and contains lower and higher frequency components due to the strong damping of the amplitude by the exponential term in Eq. 5.27. The maximum displacement is 1mm.

Fig. 5.5 shows the vertical displacement in the example model at 5 stages during the simulation, at 0.3ms, 0.9ms, 1.5ms, 2.1ms and at 2.7ms. Positive displacements are upward and negative displacements are downward. Visible in the slides shown is the solid compressional wave which reaches the top of the domain (6m from the source) between the third and fourth slide, and which leads ahead of the fluid compressional wave in the borehole. Following behind both compressional waves, and visible as a slow-moving positive-negative pair of peaks, is the Stoneley wave. In this model, in which the Stoneley wave phase speed is expected to be around 1400m/s, this mode reaches approximately two-thirds of the way up the domain by the final slide, at 2.7ms. The corresponding slides showing the potential generated by the relative fluid/solid motion are shown in Fig. 5.6. The compressional wave has a potential associated with it, but the largest potential is generated along the borehole wall, and is associated with the Stoneley wave. The first slide in Fig. 5.6 also shows the propagating wave which arrives at all detectors in the early stages of the simulation. Figs 5.7 and 5.8 show the pressure p and potential ϕ measured at 7 detectors positioned in the borehole, at 50cm intervals beginning 45cm above the source. The compressional and Stoneley waves are clear once again in the pressure plot, as is the shear mode which travels between them ($c_f^p = 3188$m/s, $c_f^s = 1859$m/s, $c^{stoneley} \approx 1400$m/s). The attenuation of the Stoneley wave due to the high porosity and permeability of the formation is particularly evident, as the wave packet is slowed, reduced in amplitude and flattened (i.e. the wavelength increases). Looking at the potential

Parameter	Property	Value
ρ_{fl}	Fluid density (kg/m^3)	1200
c_{fl}^p	Fluid compressional velocity (m/s)	1630
η	Fluid viscosity $(Pa.s)$	0.0009
σ_{fl}	Fluid conductivity (S/m)	1
ρ_s	Solid density (kg/m^3)	2650
c_s^p	Solid compressional velocity (m/s)	5400
α	Solid velocity ratio	1.6
ϕ	Porosity $(\%)$	30
k	Permeability (m^2)	1e-13
W_{mc}	Mudcake stiffness (GPa/cm)	0
ζ	Zeta potential (V)	-0.02
ϵ	Dielectric permittivity $(Farad/m)$	7.08e-10
a	Tortuosity	3.34
λ		3.377e9
γ		1.502e9
R		8.272e8

Table 5.1: The material properties for the formation and fluid and the resulting Biot coefficients used in the third example.

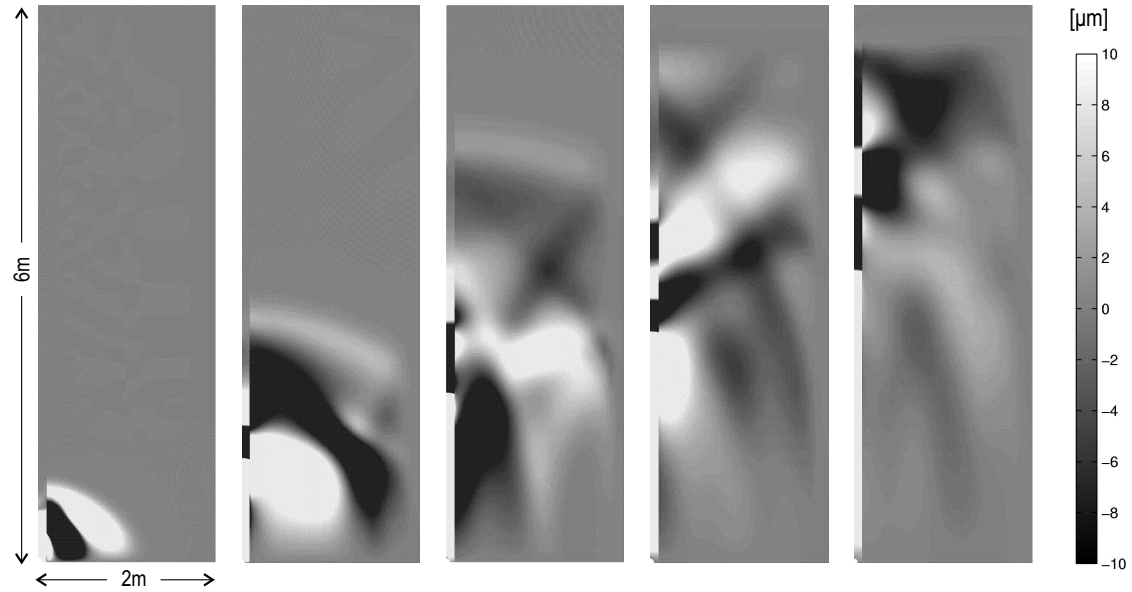

Figure 5.5: The vertical displacement (in the plane of the page) of the liquid phase in the example model, at (from left to right) t=0.3ms, 0.9ms, 1.5ms, 2.1ms and 2.7ms, where positive displacement is upward and negative displacement is downward.

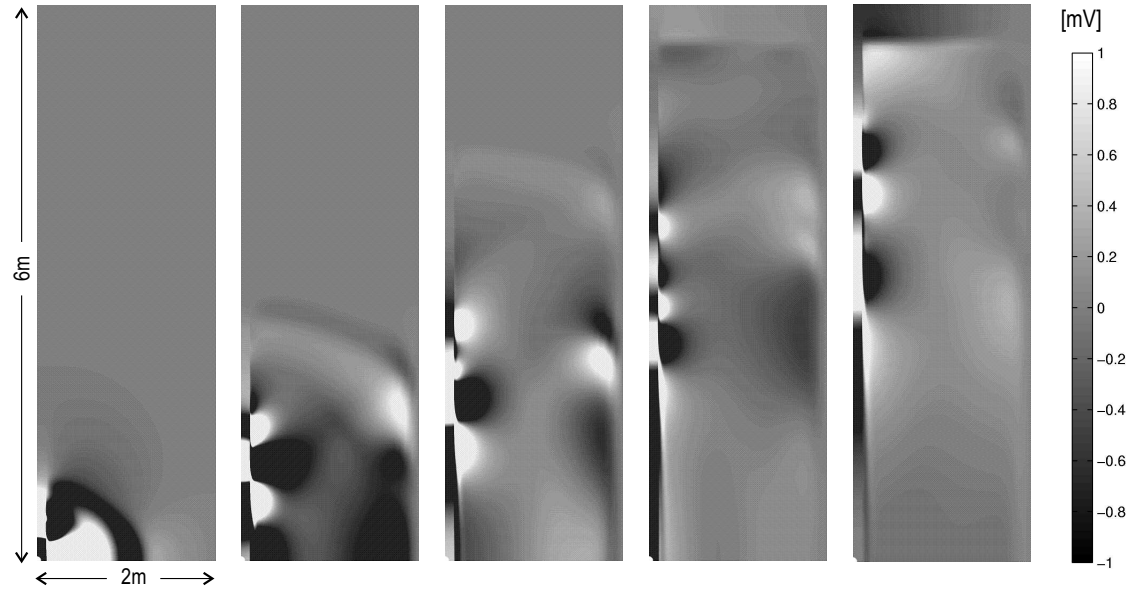

Figure 5.6: The resulting potential in the example model, at (from left to right) t=0.3ms, 0.9ms, 1.5ms, 2.1ms and 2.7ms. While there is a potential generated by the solid p-wave and other modes, the principal potential is along the borehole wall, and related to the Stoneley wave seen in Fig. 5.5.

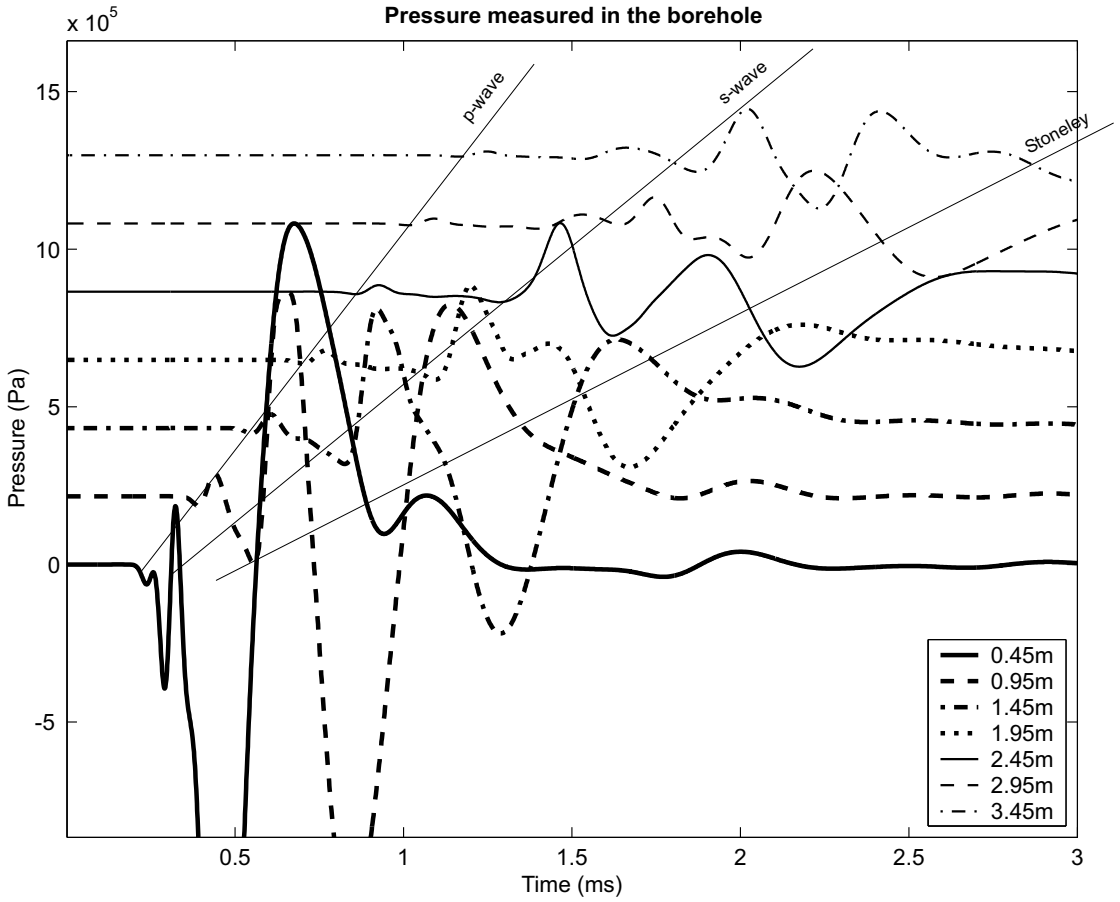

Figure 5.7: Pressure measured at 7 borehole detectors in the example model described in the main text. Compressional (p-wave), shear (s-wave) and Stoneley wave modes are all clearly visible, although the attenuation of the Stoneley is such that it does not reach the top-most detector before the simulation ends.

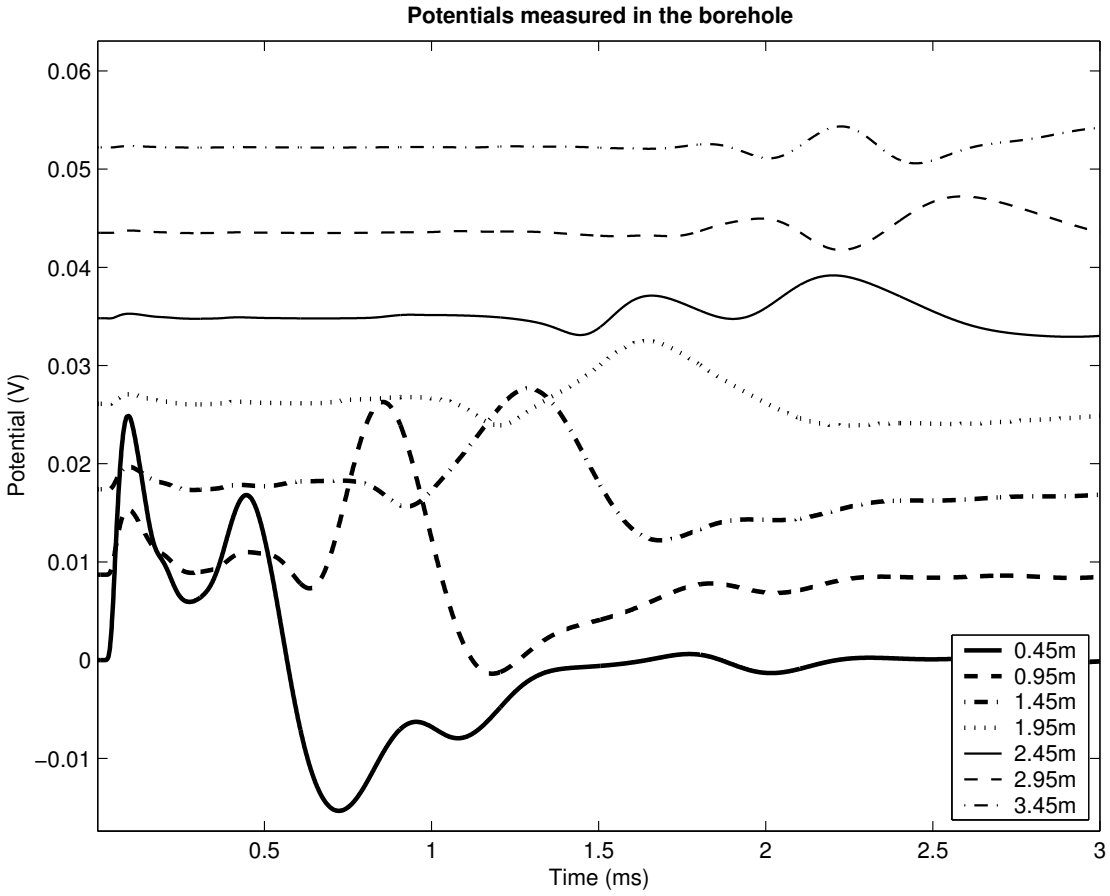

Figure 5.8: Potential measured at 7 detectors in the borehole in the example model described in the main text. The main feature visible is the Stoneley-related (streaming) potential, since the compressional and shear modes produce relatively small potentials. Also visible is the initial burst (see text).

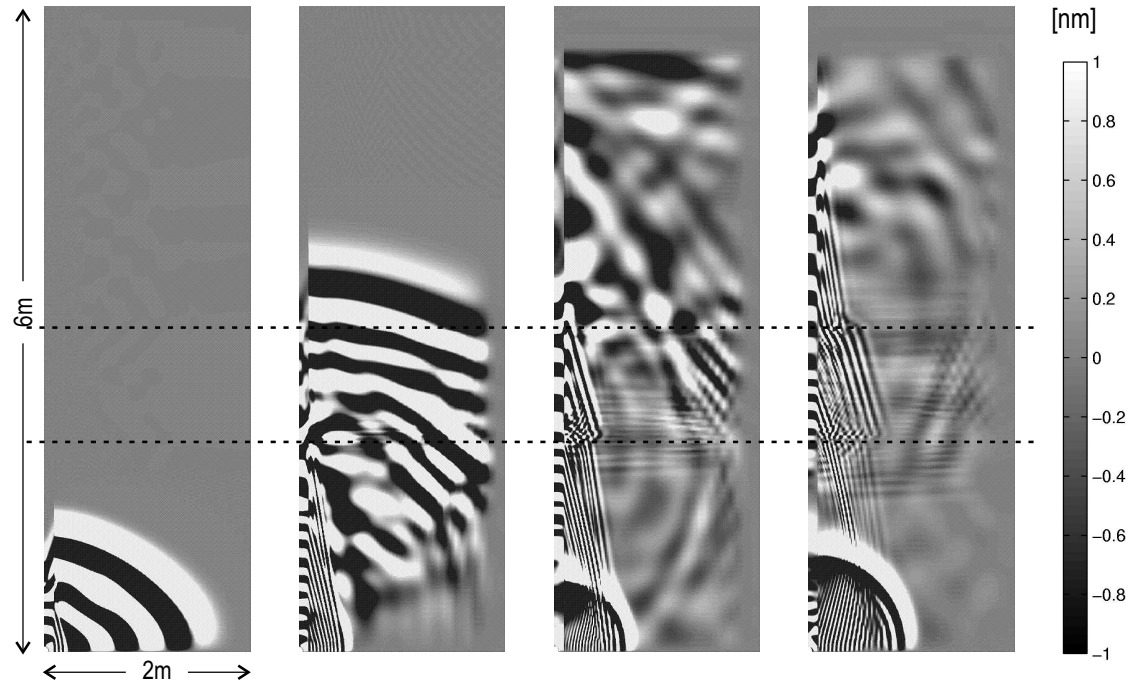

Figure 5.9: Diagrams showing the solid phase displacement fields at four instants in time, from left to right t=0.3ms, 0.9ms, 1.5ms and 2.1ms. The simulation uses a layered formation and a high frequency source of 12kHz. The higher porosity layer ($\phi = 0.2$ between the dotted lines) is marked by a change in wave speed. Note the short wavelength Biot slow wave, which is taking energy from the Stoneley wave into the formation.

detector logs (Fig. 5.8) there is no significant compressional-associated potential, but the strongest signal is the Stoneley-related (streaming) potential. As in the pressure plots, this wave is attenuated as it propagates up the borehole. In Fig. 5.8 the propagating wave, or initial burst, is seen at all detectors at around 0.1ms. It decreases in amplitude with distance.

This example shows two principal ways in which the output from the model may be viewed and analysed, either visualising the entire domain at a particular stage during the simulation, or presenting the detector logs in such a way as the travelling nature of the wave modes can easily be appreciated. In addition to the pressure and potential, each detector also records the vertical and horizontal displacements and velocities of both the fluid and solid phases, giving a total of 10 fields immediately available. The electric field can easily be calculated, subtracting the potential at one detector from the potential at another and dividing by the distance between them. Similarly, the velocity differences which are key in Eq. 5.24 can be calculated by appropriate manipulations of the velocity components which are output.

In a fourth example the results of a simulation using a layered formation and a source frequency of 12kHz are shown. Fig. 5.9 displays the whole domain at four stages during the simulation, after 0.3ms, 0.9ms, 1.5ms and 2.1ms. The layer, which lies between 2 and 3 metres above the source (total domain height 6m), has a higher

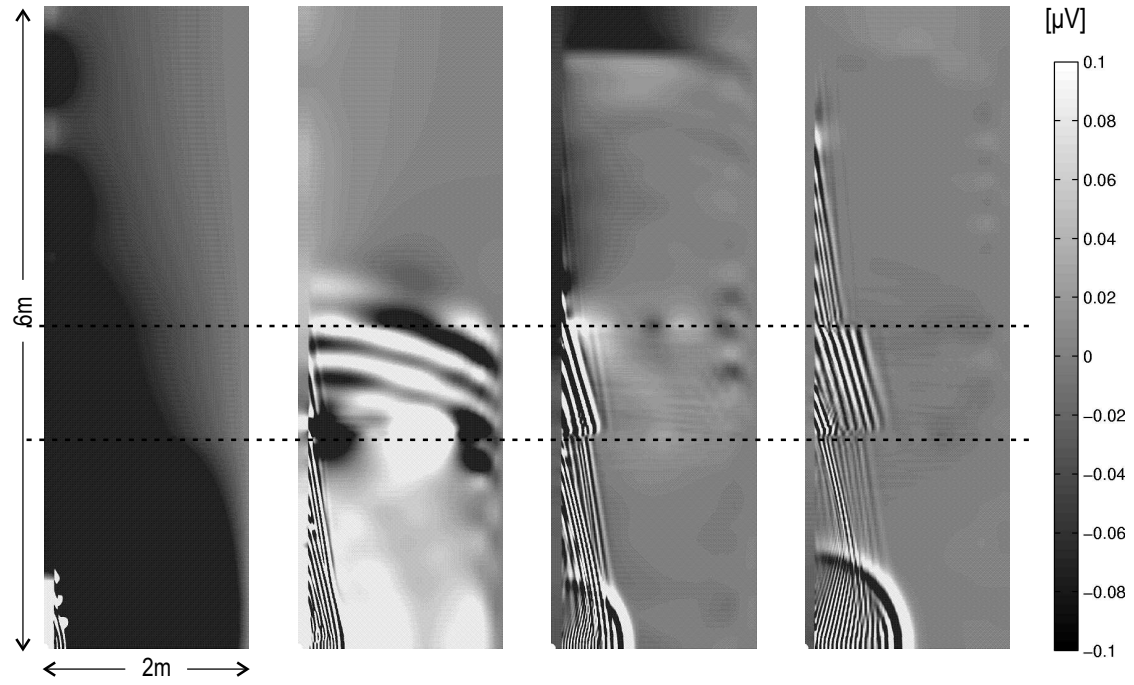

Figure 5.10: Diagrams showing the potential field at four instants in time, from left to right t=0.3ms, 0.9ms, 1.5ms and 2.1ms. The simulation uses a layered formation (higher porosity between the dotted lines) and a high frequency source of 12kHz. The major source of potential in this example is the short wavelength Biot slow wave seen also in Fig. 5.9.

porosity of 20% than the rest of the formation where the porosity is 10%. In the later slides in Fig. 5.9 this layer is identifiable by the change in wave speed which alters the angle of the propagation wave 'arc'. The high permeability throughout the entire domain of 50D (5e-11 m^2) allows the Biot slow wave to be visible, moving out from the borehole and dispersing the energy of the Stoneley wave. After 1.2ms the slow wave has travelled approximately 50cm from the borehole, giving a phase speed of around 400m/s. The wavelength is estimated at around 5cm. The potentials generated during this simulation example can be seen in Fig. 5.10, with each slide corresponding in time to those in Fig. 5.9. As in the earlier example (Fig. 5.6), the compressional wave has a small potential associated with it, but the main potential contribution is related to the Stoneley wave. However, in this case the potential does not propagate significantly into the borehole, but remains close to the slow waves in the formation. This is evidently a result of the unrealistically high permeability used in this example, which means that the fluid is moved much deeper in the formation and is not confined to the near-borehole region.

Through these examples it has been shown that seismic waves excited in a borehole generate electric potentials in the surrounding formation, which can be measured by instruments in the centre of the borehole. For a reasonable maximum source displacement of one micron our model predicts potentials of the order of millivolts or in some cases tens of millivolts, which is likely to be a suitable magnitude for most logging tools,

even in the presence of background noise. With this new model, the gap between analytical solutions and field results can be bridged, and such investigations made in an efficient manner.

5.6 Key indicators

The Stoneley wave is expected to be the main source of information for determining the properties of the formation. This is because of the way that the Stoneley wave travels up the borehole, oscillating laterally while losing energy by conversion to slow waves in the formation. Thus, compared to the other waves modes, the Stoneley wave has the greatest interaction with the region of the formation which is to be characterised. Most importantly, it is hoped that the permeability of the formation will be an important influence on the behaviour of the Stoneley wave, governing both its attenuation and the electrokinetic conversion.

The other principle wave modes, the compressional (p-wave) and shear (s-wave), are not expected to be dependent on permeability, but rather on the porosity of the formation. It is possible that other measurements will not resolve the permeability of the formation independent of the porosity, but instead give a value dependent on a simple porosity-permeability relation. Eliminating the uncertainty of the porosity through measuring the velocity and attenuation of the p- and s-waves may allow the permeability to be specified with suitable accuracy. While the propagation of these two waves through the formation is expected to produce an electric field, it will be small in magnitude compared to the Stoneley-related electric field.

5.7 Conclusions

In this chapter a numerical method for solving the poroelastic Biot equations coupled to a simplified form of Maxwell's equations is developed. It is shown how the equations are solved, using a mixed finite-element formulation, and how the variables and parameters which are required for the solution are calculated from the material properties of the solid, the fluid, and the porous formation. Numerical techniques for coping with oscillations and spurious wave modes have been described, and further techniques to enable the model to be run on large fully 3-dimensional meshes have been suggested. To illustrate the performance of the model, a set of simulations have shown the expected acoustic waves in and around a borehole, and that the Stoneley wave in particular has a streaming potential associated with it as it travels up the borehole. The mechanism by which the Stoneley wave loses energy into the formation has been shown, namely the Biot slow wave, and a comparison has been made between the results of the model and an existing analytical solution. The model results show electrical potentials of the order of millivolts, or tens of millivolts for a maximum source displacement of 1μm. This size of signal would make such investigation viable in the field. The data from the model has also enabled interpretation of the initial propagating electromagnetic wave known as the 'initial burst'. There is versatility in the model building in terms of the material properties and positioning of detectors within either the borehole or

the formation, which is a great advantage when using the software for future data analysis and interpretation. The current numerical model MAPEK may prove to be an important tool in understanding and predicting electroseismic phenomena. Modelling results shown here and presented in the literature offer encouragement for the viability of electroseismic formation characterisation methods.

Chapter 6

Borehole Electroseismics - Modelling of homogeneous formations

6.1 Introduction

Many authors have discussed ways in which permeability may be determined from acoustic logs, most using a Stoneley wave-related method. The calculation of relative permeability using Stoneley wave velocity, attenuation and dispersion has been shown by Burns (1991), Cheng et al. (1987) and Winkler et al. (1989), but determining absolute permeability using these methods would require knowledge of fluid compressibility and viscosity and the intrinsic attenuation of the formation. Methods focusing on the detection of fractures using full-waveform logs (Mikhailov et al., 2000; Paillet, 1991) were tested in granitic formations with very low matrix porosity. Fracture detection is interpreted as equivalent to permeability characterisation in these works, but the applicability of these methods to porous, fluid-bearing formations where porosity and permeability are less necessarily correlated is not obvious. Similarly the model of Tang et al. (1991) considering dynamic permeability also only discussed fracture permeability, and found that the model differed from the full 'Biot-Rosenbaum' theory in formations in which the solid compressibility was important. It is believed that by combining the electrical signals generated through electrokinetic coupling with the usual acoustic logging data it may be possible to reduce the uncertainty in the determination of formation permeability.

6.2 Description of homogeneous formation models

To begin these investigations a series of simple formation types are modelled, with the aim of understanding the nature of the data obtained, and perhaps to determine the effects of changing formation parameters on the

data. The details of the 24 models are displayed in Table 6.1. In each of these models the domain (quarter-space) measures 2m horizontally by 6m vertically, with a borehole of radius 0.1m. The fluid filling the borehole and the porous rock is water, with a conductivity $\sigma = 1S/m$ in all cases, except for model 12 in which $\sigma = 0.01S/m$. The values of porosity (from 10 to 30 %) and permeability (from 0.01mD to 1D) cover most reasonable and probable combinations. At the extreme of these values, with low porosity $\phi = 0.1$ and high permeability $k = 1$D, the critical frequency separating viscous and inertial flow is of the order of kHz (Pride, 1994). This may not be a realistic combination of parameters for the reservoir environment however, and so the full treatment of frequency-dependent material properties is left for future work. The source function for these cases is the 'short' source, given by equation 5.27, with the amplitude adjusted so as to give a maximum displacement of 1mm. The source itself is modelled as a quarter circle (to represent a spherical source in 3 dimensions) with radius 5cm. Detectors are positioned both in the borehole at 50cm intervals, and in the formation. A time-step of 1μs was used, short enough to resolve the source functions well, with the total duration of each model being 3ms.

6.3 Preliminary Findings and Results

Figs. 6.1 and 6.2 show typical borehole logs for hydraulic pressure and potential from the preliminary modelling, in this case from model 5. The distances in the legend refer to the position of the detectors above the source in the borehole. Thus, travelling waves are seen moving diagonally up and right. The principal feature in both sets of logs is the Stoneley wave, which dominates over the other wave modes, moving with a velocity of around 1300m/s. We can also make out the very small p-wave in Fig. 6.1, arriving at the topmost detector after around 1.25 ms, and the s-wave which comes between the p- and Stoneley waves. However, neither of these two modes have a significant electric counterpart in Fig. 6.2, so while they may be of interest in examining the acoustic properties of the formation, for our electroseismic investigations we focus on the Stoneley wave.

6.3.1 Normalised Stoneley amplitude versus permeability

As described above, the Stoneley wave is expected to be an important source of information and it is hoped that it may give significant clues as to the nature of the formation surrounding the borehole. In a first test the peak amplitude of the Stoneley wave is measured in both the electric field and the acoustic pressure field at detectors in the borehole for each of the 24 models described in Table 6.1. The electric field at a detector $D1$ is calculated by subtracting the potential at detector $D1$ from that at $D2$ and dividing by the distance between $D1$ and $D2$, where $D2$ is the nearest detector below $D1$ (i.e. nearer the source) in the borehole:

$$E_{D1} = \frac{\psi_{D2} - \psi_{D1}}{|\mathbf{z}_{D2} - \mathbf{z}_{D1}|}. \tag{6.1}$$

Model No.	Porosity ϕ (%)	Permeability k (mD)	Source Frequency (kHz)
1	10	1	1
2	10	1	10
3	10	100	1
4	10	100	10
5	30	1	1
6	30	1	10
7	30	100	1
8	30	100	10
9	10	0.1	1
10	10	0.01	1
11	30	1000	1
12*	30	100	1
13	20	0.01	1
14	20	100	1
15	20	1000	1
16	30	0.1	1
17	10	10	1
18	20	10	1
19	30	10	1
20	10	10	10
21	20	10	10
22	30	10	10
23	20	1	1
24	20	0.1	1

Table 6.1: Model properties for the preliminary modelling stage, in which a homogeneous formation surrounds the borehole. Full details can be found in the main text. * Model number 12 uses a low fluid conductivity.

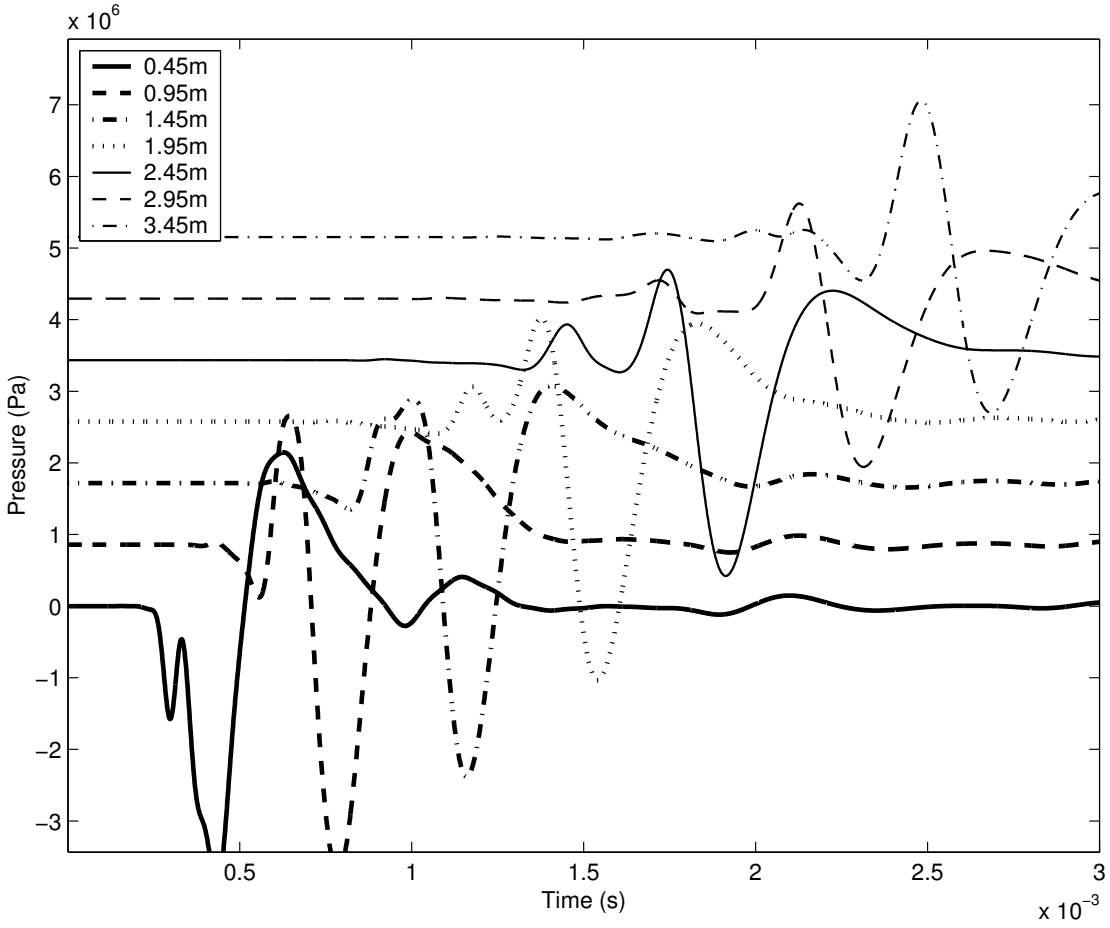

Figure 6.1: An example of the acoustic logs. The legend refers to the position of the detector above the source, in the borehole. The Stoneley wave can be clearly seen, reaching the detector at 3.45m around 2.5ms after the initialisation of the source.

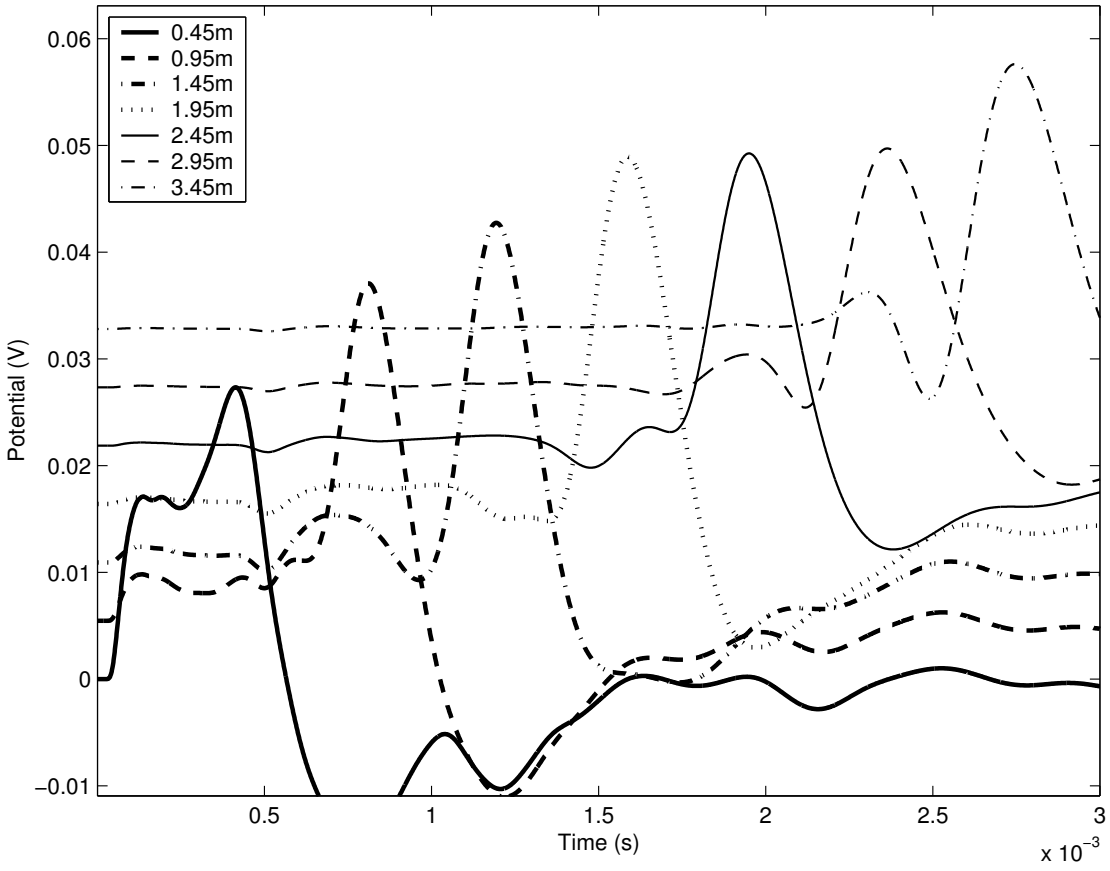

Figure 6.2: An example of the potential logs. The legend refers to the position of the detector above the source, in the borehole. The Stoneley wave can be clearly seen, reaching the detector at 3.45m around 2.5ms after the initialisation of the source.

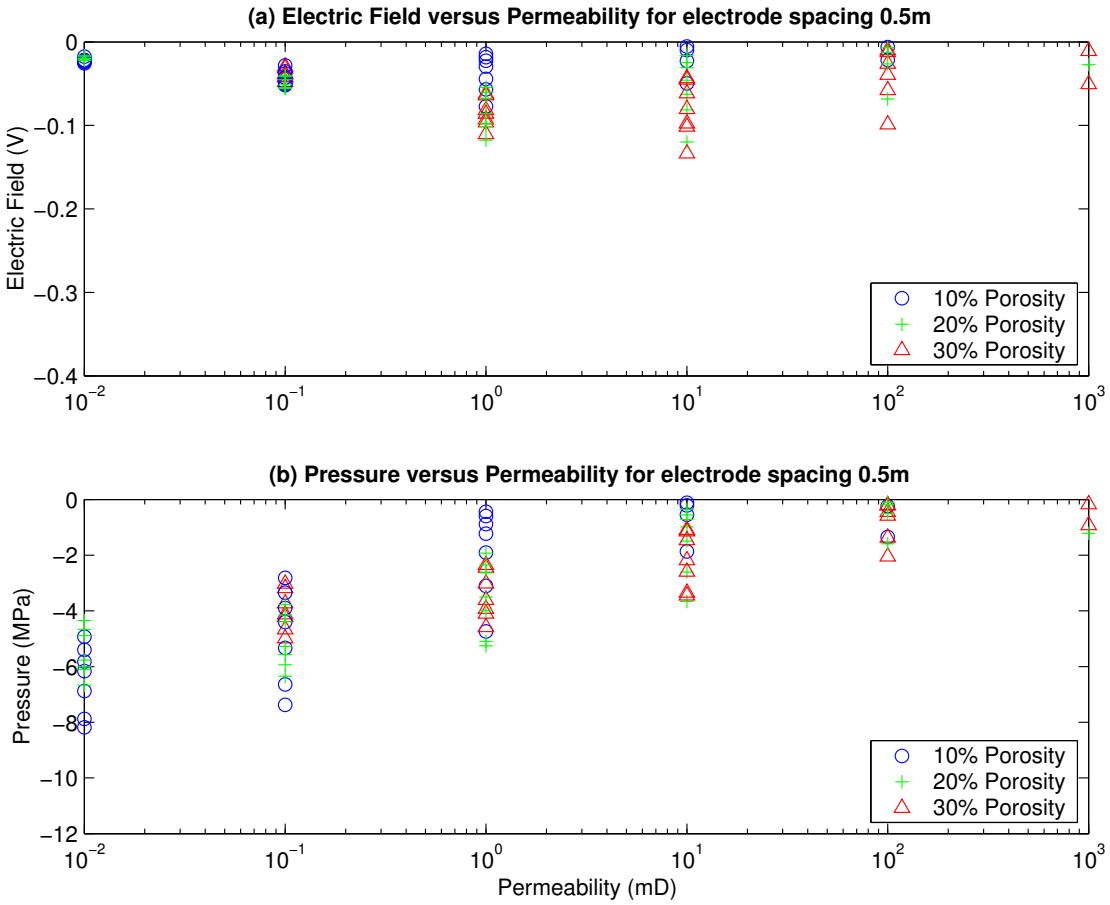

Figure 6.3: The relation of (a) electric field and (b) pressure to permeability as measured by detectors in the borehole. Data from all of the models using a 1kHz source are plotted (see Table. 6.1), at each of seven detectors in the borehole, where the Stoneley wave was well defined.

This approximation to the electric field is used in preference to the potential since this can reduce the effect of background noise, and is the measurement which would be made in the field. Fig. 6.3 shows the electric field and pressure peak values plotted individually. Several values are plotted for each porosity and permeability combination, corresponding to the various measurements at each borehole detector.

The electric field data show two interesting features. First a decrease in amplitude both at high and low permeabilities, which is explained by a severe limiting of relative phase movement at low permeabilities, and the dominance of k in the denominator on the right hand side of Eq. 5.24 when the permeability is high. Second, in the mid-permeability range, an increase is seen in the value of the electric field with porosity. This is due to the increase in fluid-solid surface contact area which means that more ions are moved per unit volume of the porous formation, a fact reflected in the presence of ϕ in the numerator on the right hand side of Eq. 5.24.

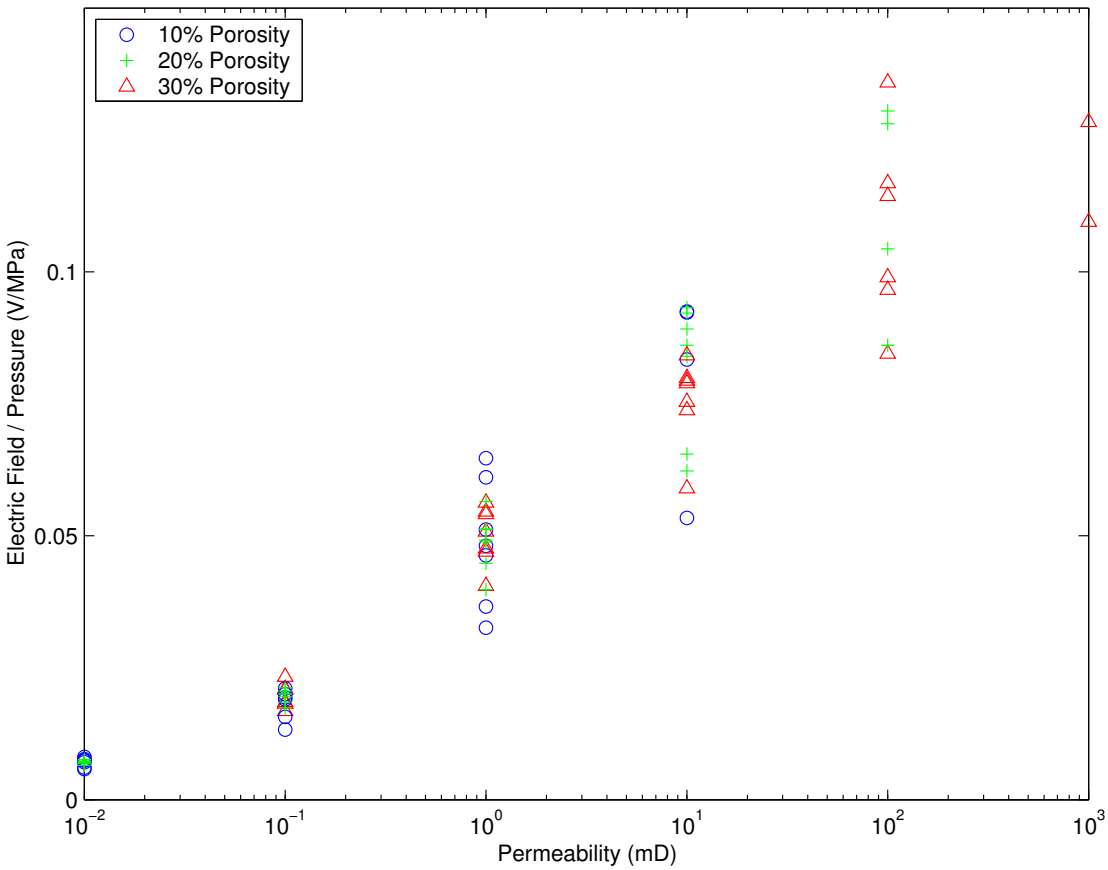

Figure 6.4: The relation of normalised electric field to permeability as measured by detectors in the borehole. Data from all seven detectors along the borehole are included where the Stoneley wave is clear, hence the several values plotted for each formation model. The roughly linear increase with the log of permeability is encouraging, as it indicates the Stoneley wave is strongly affected by the permeability of the formation.

The pressure measured in the borehole decreases with increasing permeability. This is as expected, since with greater permeability more energy is transferred from the borehole fluid to the formation fluid and the rock. At low permeabilities, the formation fluid is not easily moved, and so a greater proportion of the Stoneley wave energy remains in the borehole. The electric field amplitude is then divided by the pressure amplitude to find a normalised Stoneley-related electric field (NEF) and plotted against the model permeability in Fig. 6.4. It was not possible in all cases to pick the peak of the Stoneley wave in either the electric field or pressure fields. Only those cases where the Stoneley peak was unambiguous are plotted. The main advantages of using this NEF are that is it no longer necessary to know the initial amplitude of the source signature, or even to maintain this amplitude at a constant value from one set of borehole logs to another, and that as the Stoneley wave is attenuated along the length of the borehole the detectors far from the source can still be used.

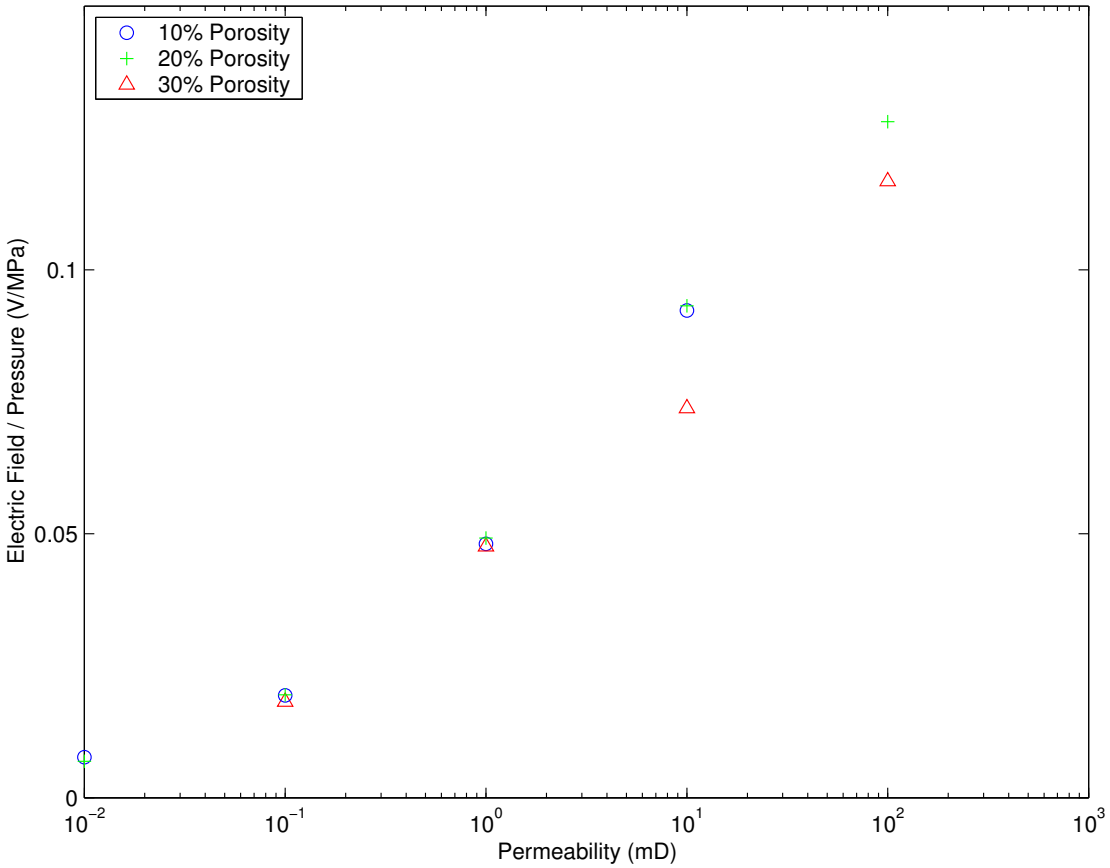

Figure 6.5: Values of the normalised electric field measured at 2m, showing that a measurement using a single receiver position is still indicative of formation permeability.

It might be, however, in a simple experimental set up that a single receiver array is used, consisting of an electrode dipole and a hydrophone at a fixed distance from the acoustic source. The values of the NEF for a fixed distance of 2m between the source and the hydrophone are plotted in Fig. 6.5. The strong increase of NEF with permeability is maintained, confirming that is would not be necessary to use a large number of receiver positions to measure the effect of permeability on the Stoneley wave. A measurement of NEF using a single receiver position is still indicative of formation permeability.

It is important to understand how the permeability dependence of the NEF arises. In steady-state flow in a homogeneous formation, the NEF would be equal to the coupling term L_x/σ_f, since $\dot{\mathbf{u}} = 0$ and the pressure $p = \frac{\eta\phi}{k}\dot{\mathbf{U}}$ in Eq. 5.24. In this modelling $\dot{\mathbf{u}} \neq 0$ and so the movement of both phases must be accounted for, and the way which this is influenced by the permeability. The following interpretation is proposed:

At high permeability the pore fluid is easily moved, and thus can transport much of the energy of the borehole fluid into the formation. The solid phase is less easily moved than the pore fluid due to its greater

inertia and stiffness, and so solid displacement is relatively small. At low permeability the pore fluid can no longer move so easily relative to the solid phase. In this case, a larger reflection of energy back into the borehole is expected, and also a larger solid displacement than at high permeability as the solid moves *with* the fluid, reducing the relative movement of the phases and so the potential. The increased pressure in the borehole (from reflection) and the decrease in potential and thus in electric field result in a lower normalised electric field at low permeabilities, as seen in Fig. 6.4. As the solid density increases, we expect the solid displacement to be further reduced, giving a better approximation of the zero-solid-displacement model, and therefore a convergence of the NEF on the value of the coupling coefficient. Fig. 6.6 shows the NEF plotted against permeability for two grain densities, $\rho_s = 2650\text{kg/m}^3$ as above and $\rho_s = 7500\text{kg/m}^3$, where all other parameters remain unchanged ($\phi = 0.3$). Using a higher grain density reduces the effect of the permeability, and the data points begin to converge on the value of the coupling coefficient $L_x/\sigma_r = C = 1.573 \times 10^{-2}$ V/MPa, marked by a horizontal line.

These results suggest that it is possible to use the acoustic and electrical signals associated with the Stoneley wave to make a determination of the permeability of the formation surrounding the borehole, given other information about the rock and fluid including densities, velocities and porosity. In particular, the normalised amplitude of the Stoneley-related electric field increases with permeability through the range of reasonable values. In addition, there appears to be no clear correlation between the NEF and porosity. We note that Mikhailov et al. (2000) find that the NEF does depend on porosity, although their model takes into account neither the movement of the solid phase nor the permeability of the fractured rock as distinct from the porosity. This second omission may be valid in fractured granite, where the matrix permeability is negligible, but in a sedimentary rock where permeability exists both in fractures and through well consolidated pore spaces, it may be useful to distinguish between permeability and porosity. Further discussion of the comparison between the theory presented here and that described by Mikhailov et al. (2000) can be found in section 7.2.

6.3.2 Initial burst

In addition to the electric fields associated with the various travelling wave modes, also visible at around 0.04ms in Fig. 6.2 is a propagating electromagnetic signal which arrives almost simultaneously at all detectors. This is caused by the first arrival from the source hitting the borehole wall immediately next to the source, and as such could reveal something about the nature of the nearby formation. Fig. 6.7 shows the width-at-half-height of this initial peak measured by a detector 5cm above the source in the borehole, against permeability. The width is in terms of time rather than space, and so could be measured directly from a borehole log taken in the field. There is an evident decrease in the width of the initial burst with increasing permeability, The relationship is weak, however, and perhaps too weak to be distinguished in real data amongst the noise.

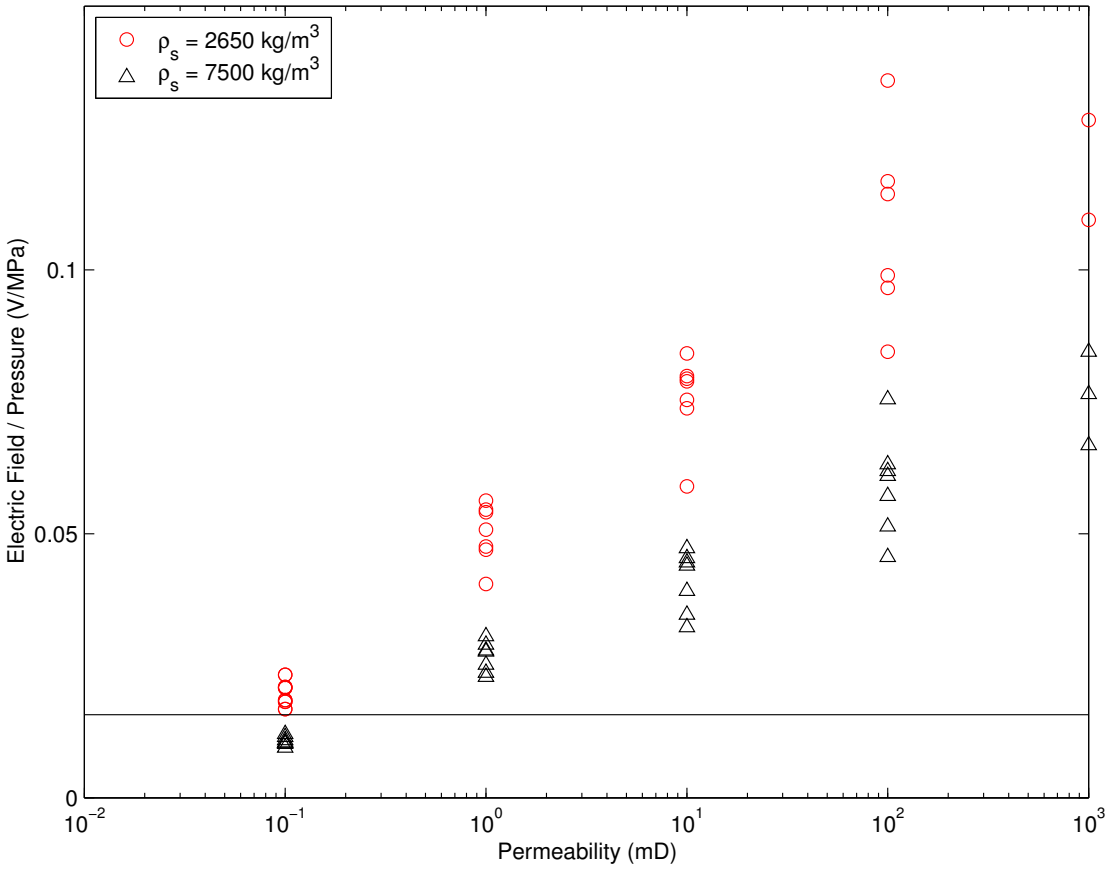

Figure 6.6: Normalised electric field versus permeability for two grain densities: $\rho_s = 2650\text{kg/m}^3$ and $\rho_s = 7500\text{kg/m}^3$. Porosity $\phi = 0.3$ in both models. Increasing the grain density reduces the effect of the permeability, and the data points converge on the value of the coupling coefficient $C = 1.573 \times 10^{-2}$ V/MPa, shown by the horizontal line. Data are plotted from each of seven detectors disposed in the borehole, between 0.45m and 3.45m from the source.

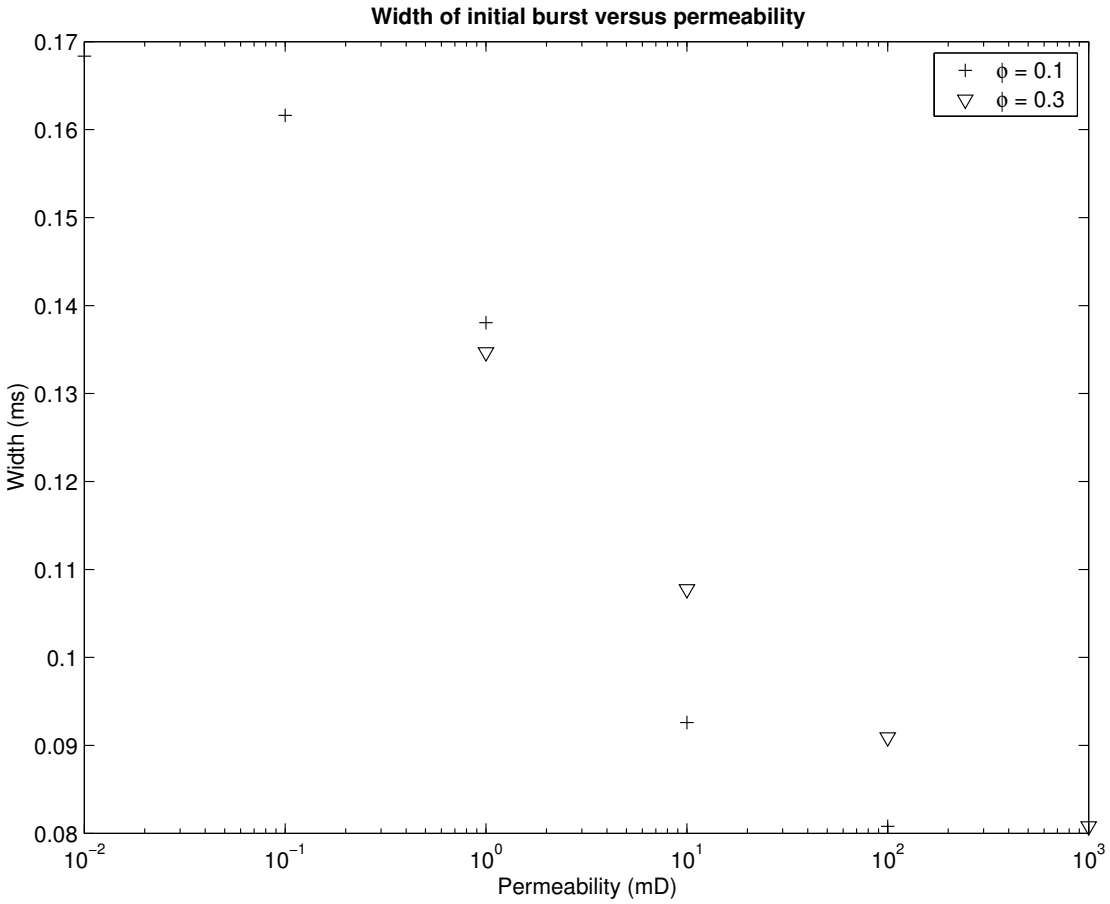

Figure 6.7: The width-at-half-height of the initial electrical signal measured by a detector 5cm above the source in the borehole, versus the permeability of the formation.

6.3.3 Depth of investigation

Since the aim of the present work is to determine the properties of the formation surrounding the borehole, it is important that the method is capable of gathering information about that formation up to a reasonable depth away from the borehole, and is not too concentrated on the very near-borehole regions. To investigate this, a series of models have been set up in which the coupling between the phase displacements and electric potential is only non-zero beyond a certain distance d into the formation. Potentials measured in the borehole are a sum of all potentials generated everywhere, and so by eliminating those potentials generated in the first $d$cm in the formation, the proportion of the total signal being generated beyond that distance can be found. Figs. 6.8 and 6.9 show this information, where the reference signal is the peak of the Stoneley wave and the peak of the initial burst, respectively. For both the Stoneley and initial burst it is clear that by far the majority of the signal received in the borehole is generated in the first centimetre of the formation, even for high porosity and permeability where the greatest transmission of energy into the formation would be expected. This is not ideal, especially as features such as the mudcake will be important over that region. This will clearly be an important issue to address once modelling includes the mudcake effects.

One means by which the depth of investigation might be extended is to alter the frequency of the source. At low frequency, the longer wavelength should increase the penetration of acoustic waves into the formation. To see what effect changing the source frequency has on the results, the model with the best penetration at 1kHz (run 7: $\phi = 0.3$, k=100mD) is repeated at 250Hz and 10kHz. The results are plotted in Fig. 6.10, and show that the depth of investigation does improve at lower frequency. At 1kHz about 35% of the potential measured in the borehole is generated beyond 2cm into the formation. At 250Hz this increases to almost 50%, while at the higher frequency of 10kHz only around 25% of the signal comes from beyond 2cm. Low frequencies favour the Stoneley wave, in that the Stoneley wave is the dominant wave mode seen in the wave train at frequencies around 1kHz. These results suggest that even lower frequencies than 1kHz may be used to maximise the penetration into the formation.

6.3.4 Effect of varying borehole radius

The effect of altering the radius of the borehole on the Stoneley wave characteristics and on the initial burst is now investigated. In the previous section a radius of 0.1m was used, which is fairly typical for both oil field and near-surface boreholes. A borehole would not normally be expected to have a radius as large as 0.20m (7.9in), unless there had been significant damage done to the borehole wall, and the minimum size is limited to that which will accommodate a sonde which may have a radius of around 0.05m.

Cheng & Toksöz (1981) note that the presence of a solid tool in the borehole effectively reduces the radius of the borehole, when looking at the dispersion characteristics of the Stoneley wave. At low frequencies (less than 10 kHz) a larger effective radius of the borehole results in a higher phase velocity for the Stoneley wave.

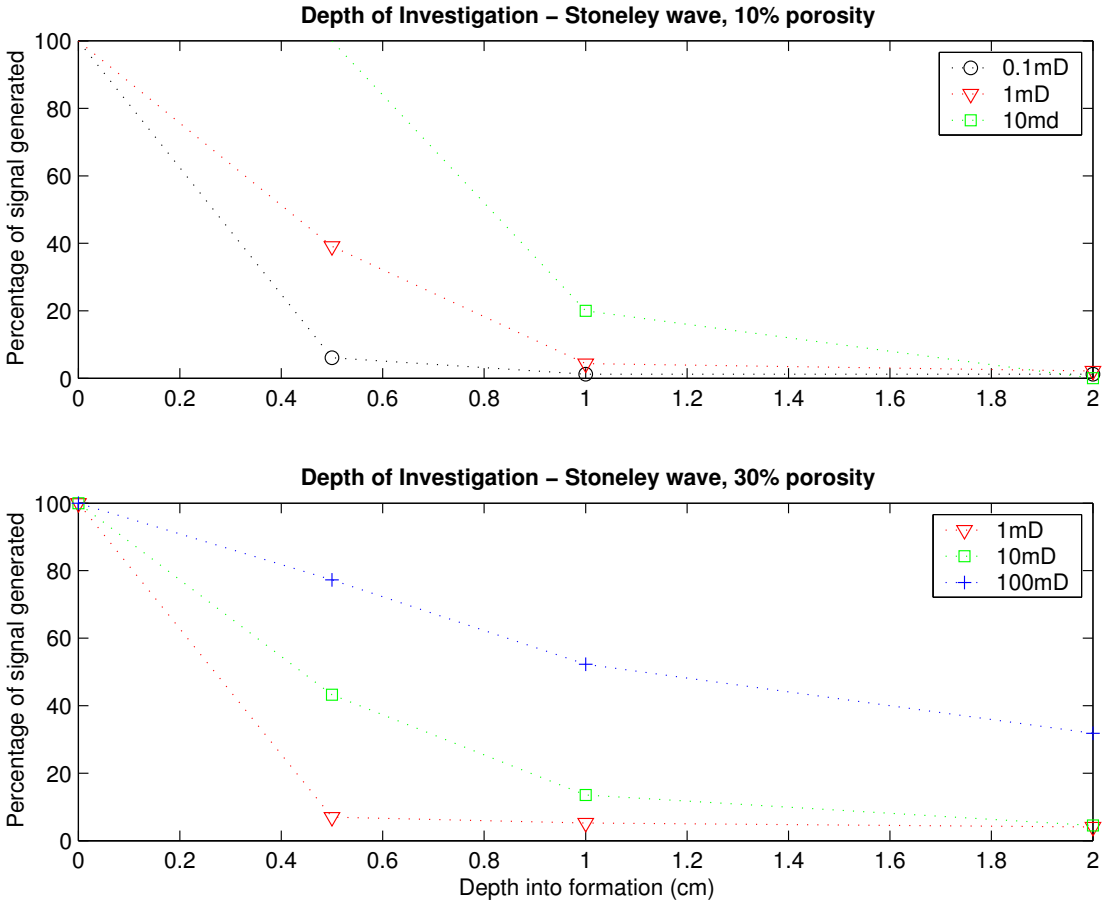

Figure 6.8: Graphs showing the depth of investigation of the Stoneley wave for (a) a formation with ϕ=10%, and (b) ϕ=30%, as measured by a detector 2.5m from the source in the borehole. The percentage of the Stoneley wave-related electric signal measured in the borehole which is generated beyond a certain distance into the formation is plotted. A higher percentage at 2cm therefore indicates superior penetration into the rock. (Note in a) for the 10mD model the data at 0.5cm was greater than 100%. This is probably due to wave mode interference.)

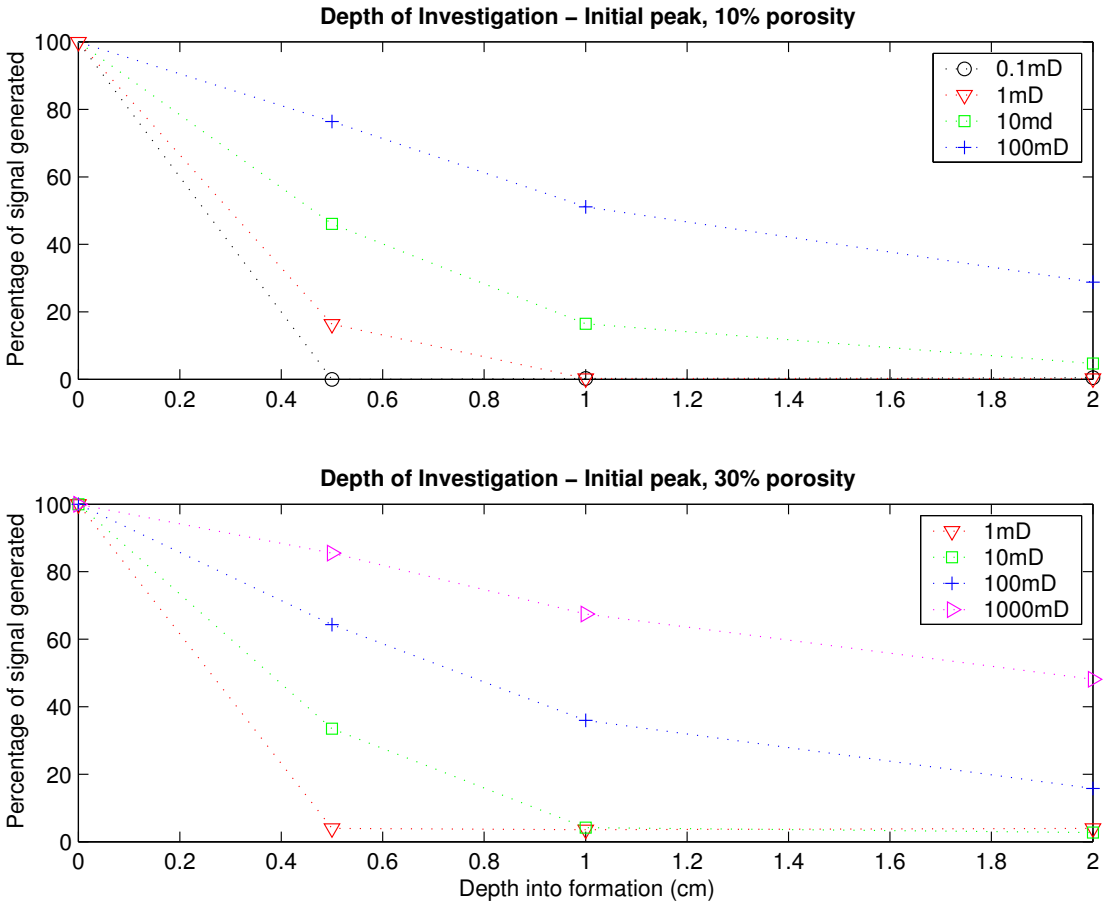

Figure 6.9: Graphs showing the depth of investigation of the initial burst for (a) a formation with ϕ=10%, and (b) ϕ=30%. As with Fig. 6.8 the percentage of the electric signal generated beyond a given distance into the formation is plotted. Data as measured by a detector 5cm from the source in the borehole.

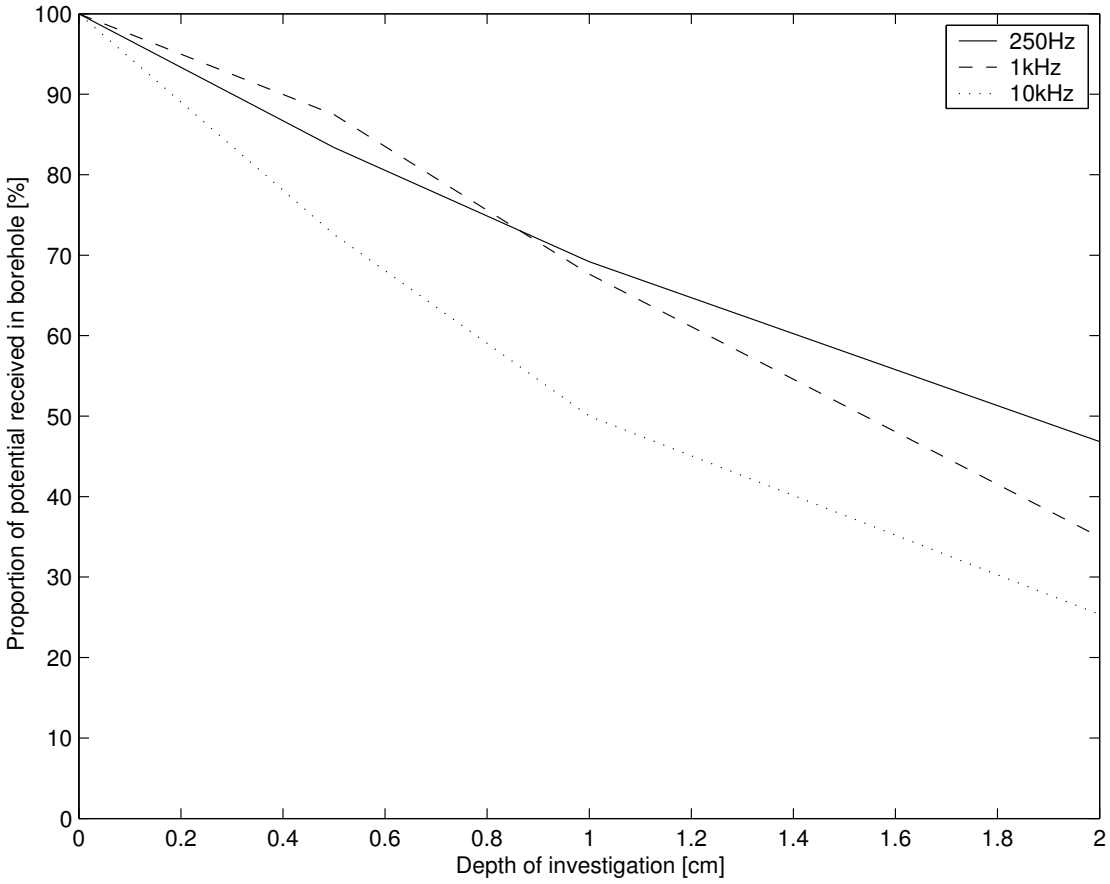

Figure 6.10: The depth of investigation of the Stoneley wave at 250Hz, 1kHz and 10kHz. At 250Hz nearly 50% of the Stoneley-related electric signal is generated beyond 2cm into the formation. The measurements were made by the detector at 2.45m above the source in the borehole.

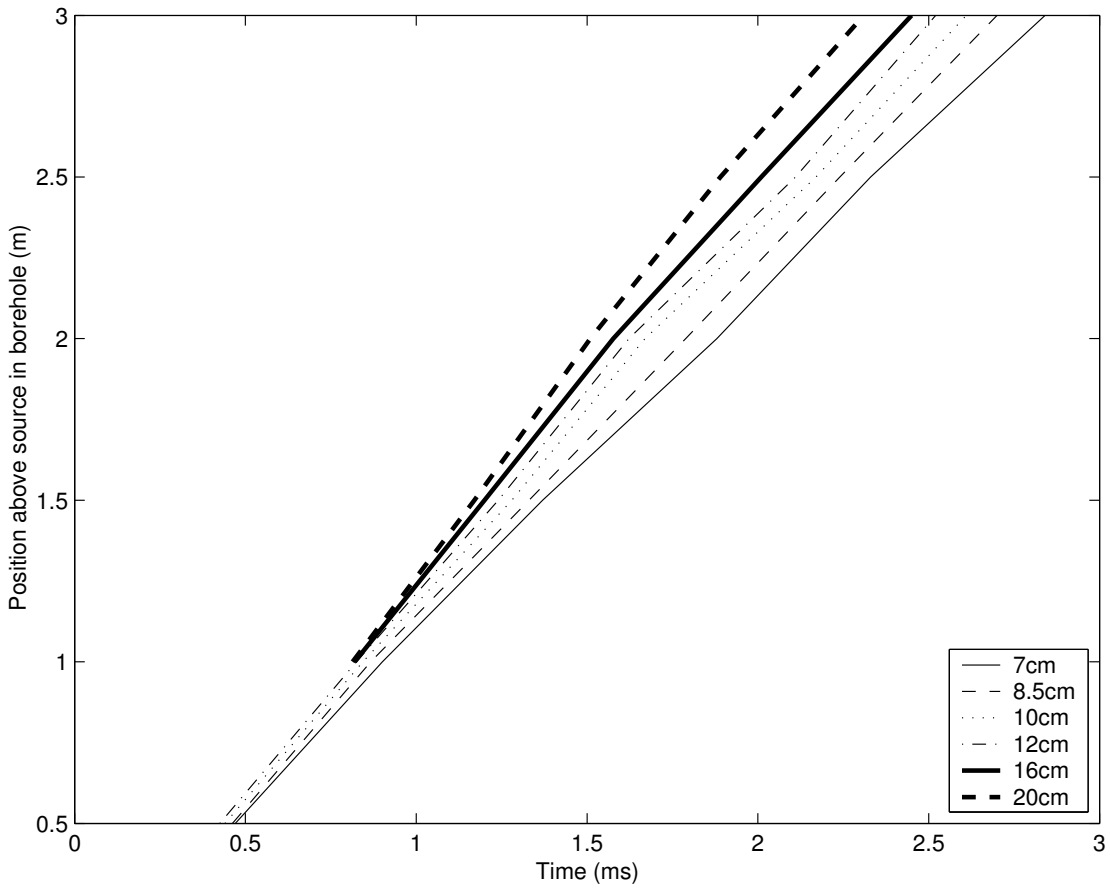

Figure 6.11: Arrival times for the Stoneley wave at detectors placed every 0.5m along the borehole. There is a small increase in Stoneley phase velocity with increasing borehole radius.

Similarly, using the definition of the Stoneley wave-number κ_z given by Tang et al. (1991) which is, to a first approximation, inversely proportional to the borehole radius, the Stoneley phase velocity $V_{st} = \omega/\Re(\kappa_z)$ will increase slightly as the radius increases. Fig. 6.11 shows the results from modelling with MAPEK, where the arrival time of the Stoneley wave at the detectors in the borehole is plotted, for 6 different borehole radii (ϕ=0.3, k=100mD). Increasing the radius of the borehole is seen to increase the phase velocity of the Stoneley wave.

In Fig. 6.12 the normalised Stoneley-related electric field versus permeability is shown, for models with borehole radii varying between 0.07m and 0.16m. In Fig. 6.4 the values of NEF at all detectors for each model are plotted. For clarity, the mean value for all seven detectors is drawn as a single point. The models included are runs 1 (ϕ=0.1,k=1mD), 7 (ϕ=0.3,k=100mD), 17 (ϕ=0.1,k=10mD) and 19 (ϕ=0.3,k=10mD). Data from models with the same borehole radius and the same porosity (e.g. runs 1 and 17 or runs 7 and 19) are joined by a dotted line.

The characteristics of the initial burst, shown in Fig. 6.13, change mostly as expected when the radius of

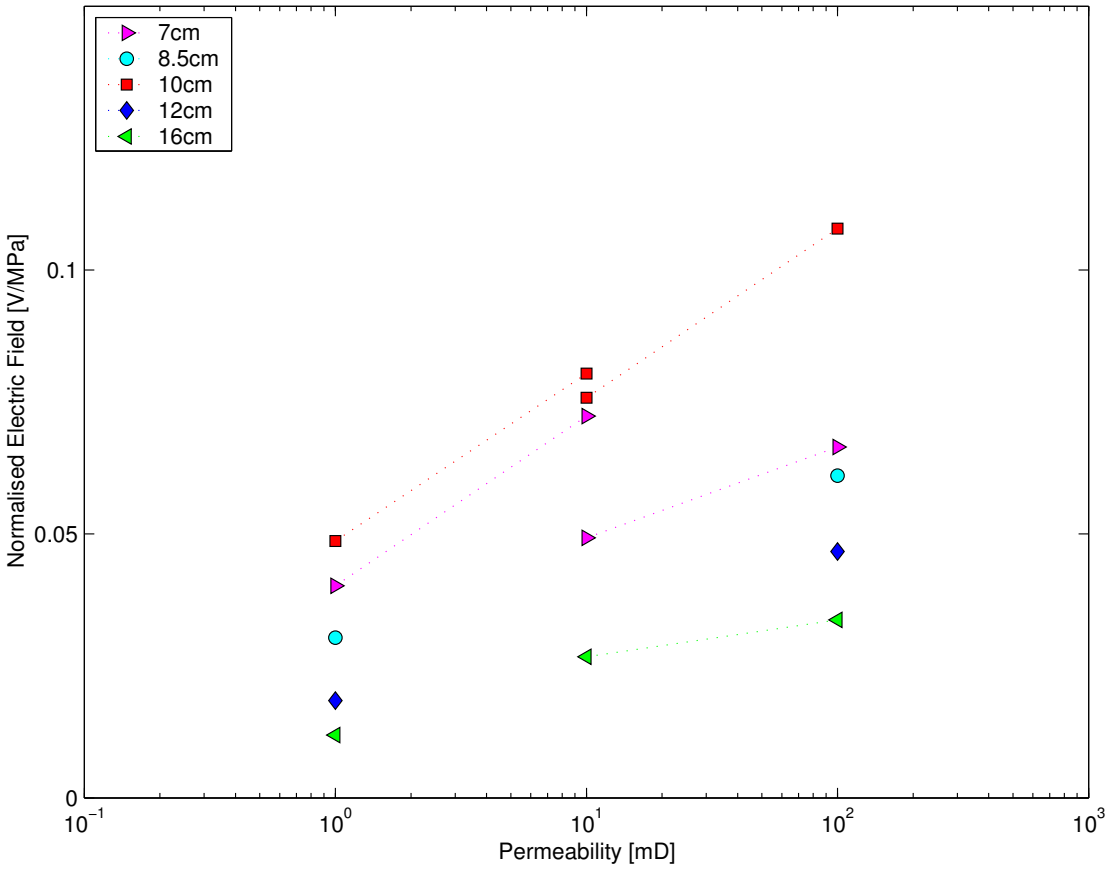

Figure 6.12: The variation of the normalised electric field with borehole radius. Models included are runs 1 and 17 (with ϕ=0.1), and 7 and 19 (with $\phi = 0.3$). The values plotted are the mean value of normalised electric field at all seven borehole detectors. Models with the same porosity are joined by a dotted line.

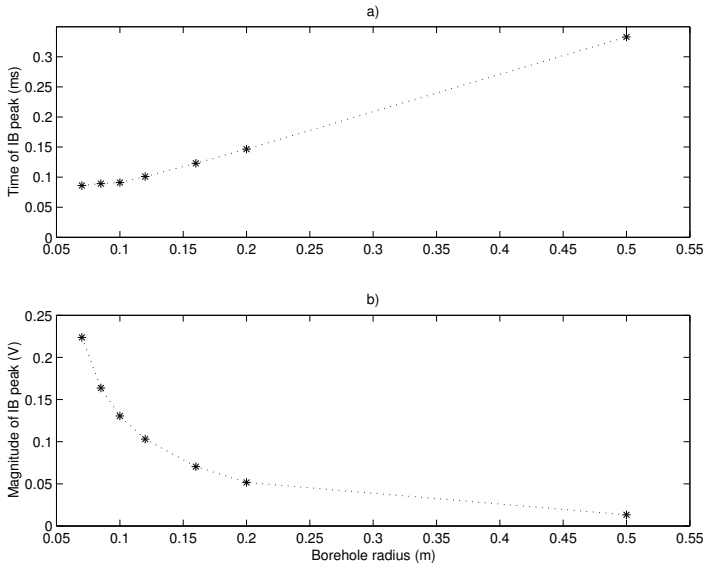

Figure 6.13: Analysis of the initial burst characteristics for varying borehole radius, as measured by an electrode centralised in the borehole, 5cm above the source: a) Time of the initial burst peak, and b) Magnitude of the initial burst peak.

the borehole is altered: the increased travel time of the fluid wave to the borehole wall is reflected in the arrival times of the initial burst peak which increase approximately linearly with radius, and the increased distance over which the potential must propagate to the borehole detectors is shown by the roughly $1/radius$ behaviour of the initial burst peak magnitude.

6.3.5 The borehole wall exclusion zone

Due to inherent inaccuracies in the numerical modelling, it is necessary to make a small adjustment to the material properties immediately around the borehole wall. Fig. 6.14 shows the nodes in the FE mesh across the borehole wall. Since the material properties used in finite-element modelling are assigned to the nodes themselves, the definition of the borehole wall is not precise, but occurs as a linear interpolation between adjacent nodes, one in the borehole, the other in the formation. Due to the discontinuity in material properties over this boundary, there is often a numerical error in the values of displacement and velocity assigned to the first line of nodes in the formation. The electrokinetic equation (Eq. 5.24) converts this difference in phase velocities into a potential. This error is solved by setting the coupling coefficient to zero along this line of nodes, and by refining the mesh around both sides of the borehole wall. As shown in Fig. 6.14, the minimum element size along the borehole wall is less than half a millimetre. A trade-off can then be made between improving the accuracy of the solution by decreasing the width of these nodes, and the computational expense that this incurs. In light of the results from the 'depth of investigation' experiments above, it is clearly important that the

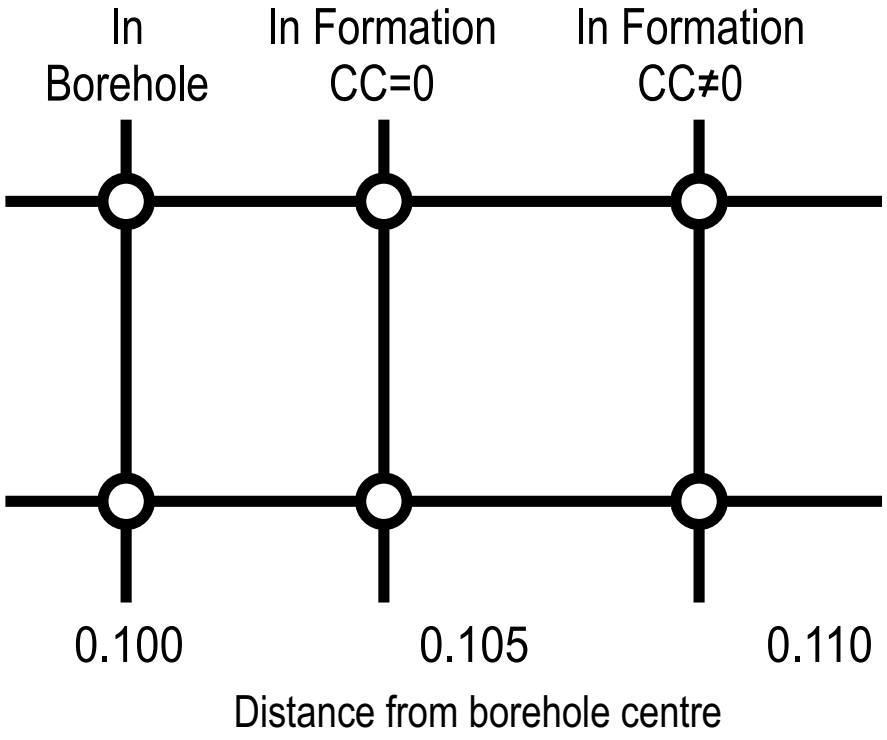

Figure 6.14: A diagram showing the nodes around the borehole wall. Nodes at 0.1m from the central symmetry axis of the borehole are designated as in the borehole. The adjacent line of nodes are assigned the properties of the formation, with the exception of the electrokinetic coupling coefficient. This is set to zero here to eliminate erroneous potentials due to small numerical inaccuracies. Nodes beyond this point are assigned the properties of the formation, including the correct coupling coefficient.

exclusion zone should not eliminate a significant portion of the potential generated either by the initial burst or by the Stoneley wave. To check this the results of simulations with different exclusion zones are compared, the first with a width of 0.5mm as used in the modelling above and as depicted in Fig. 6.14, and the second with a width of 0.1mm. Fig. 6.15 shows the potential logs from detectors in the borehole surrounded by a formation with ϕ=0.1, k=1mD. Similarly, Fig. 6.16 shows the potential logs from detectors in the borehole surrounded by a formation with ϕ=0.3, k=100mD. It can be seen that the effect of narrowing the exclusion zone is greatest at low porosity and permeability, which reflects the results from section 6.3.3.

6.4 Conclusions

Preliminary modelling of idealised, homogeneous formations has shown that the Stoneley-related electric field is sensitive to formation permeability up to values around 1D. It is believed that this relationship results from the full consideration of the poroelastic theory, including displacements of the solid phase. With knowledge of the other parameters and formation properties, permeability may be determined either using a simple graph such as that shown in Fig. 6.4 and reading off the permeability for a given value of the NEF, or by a more sophisticated approach such as an iterative inversion procedure. The initial burst may also contain permeability-sensitive information, but is more difficult to measure in practice than the Stoneley wave. Interference from an electrically driven source, which would be necessary in deep boreholes, would probably overwhelm the initial burst signal. The depth of penetration of the method is small, but improves slightly when lower frequencies are used. This may have consequences when more realistic borehole models including mudcake are used. In addition, the 'normalised electric field' method is sensitive to the radius of the borehole, with the strongest permeability dependence when the borehole radius is equal to 10cm.

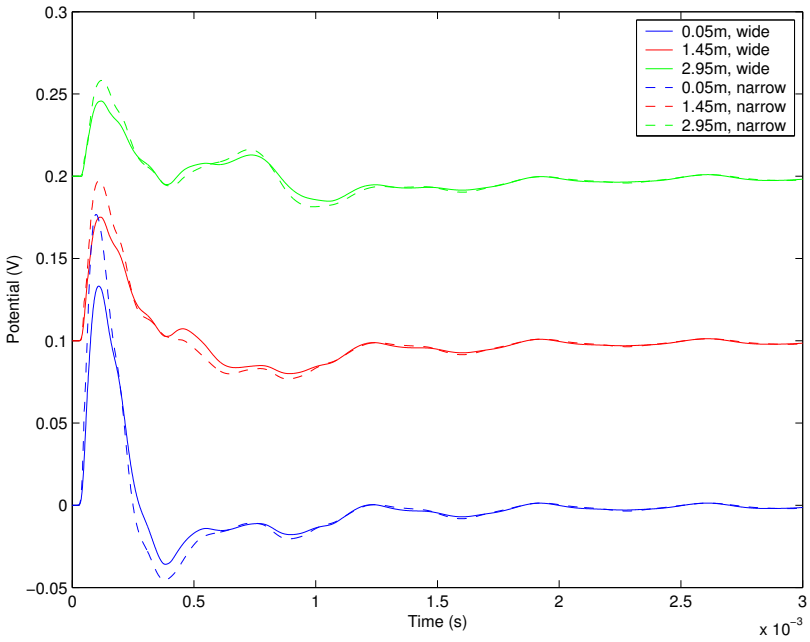

Figure 6.15: A graph showing the potential logs measured in the borehole for the two different exclusion zone widths. In the 'wide' runs the exclusion zone is 0.5mm thick, and in the 'narrow' runs it is 0.1mm thick.

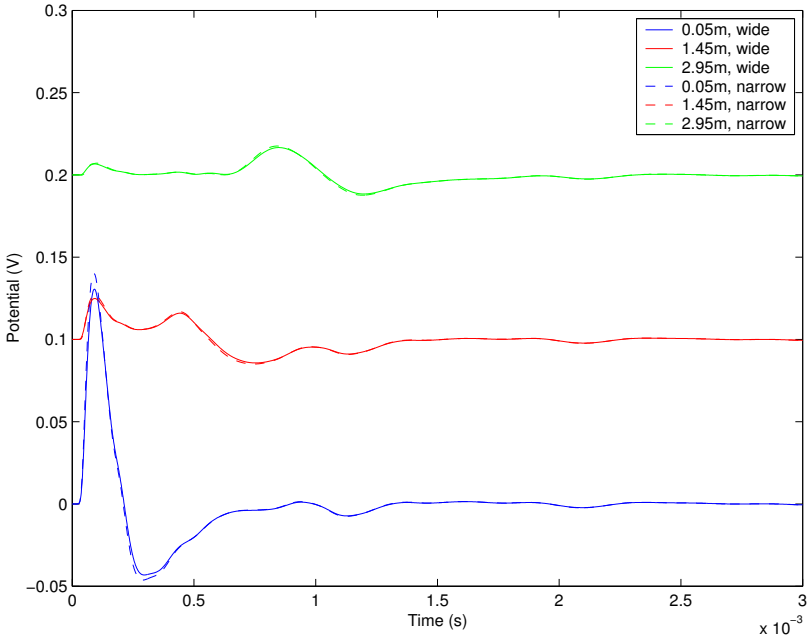

Figure 6.16: A graph showing the potential logs measured in the borehole for the two different exclusion zone widths. In the 'wide' runs the exclusion zone is 0.5mm thick, and in the 'narrow' runs it is 0.1mm thick.

Chapter 7

Borehole Electroseismics - Layering and Mudcake

7.1 Introduction

In the previous chapter the focus was the behaviour of seismic waves in a highly idealised environment, that of a homogeneous porous formation. In such an environment it was found that it may be possible to determine the properties of the formation through a combination of acoustic and electric data readings. In the real world an assumption of homogeneity is unlikely to be a reasonable one, except on small scales. In a hydrocarbon reservoir environment, the vertical heterogeneity is likely to be significant and, indeed, is an important motivating factor for the development of a characterisation tool. In this chapter layered formations are considered, and the behaviour of the measurement techniques used previously is examined, in the presence of varying material properties. Most of the previous studies into heterogeneous formations (Mikhailov et al., 2000; Tang et al., 1991) are concerned with fractured rock rather than contrasting layers of porous, fluid-bearing rock. Biot theory is, however, well designed to model the propagation of waves through coherent strata as the formation may be considered to be homogeneous on a scale larger than that of the pore-structure. In the modelling described in section 7.2 the ability of the NEF method to locate and characterise a contrasting layer intersecting the formation is investigated. The practical consideration of the optimum location of the hydrophone in relation to the electric dipole is also considered in relation to this modelling of layered formations.

In a hydrocarbon reservoir environment the realities of the drilling process must be considered, and in particular the mudcake layer which resides on the wall of the borehole. The mudcake acts as an impedance layer, reducing the communication between the fluid in the borehole and the formation. A numerical representation of mudcake in the context of the Biot theory of wave propagation in porous media was first described by

Rosenbaum (1974), who introduced the concept of a surface impedance to relate the fluid flow velocity into the pores to the pressure difference on either side of the borehole wall. Liu & Johnson (1997) generalised this approach to include a description of the mudcake as a finite or zero thickness membrane, and Brie et al. (2000) computed the effect of mudcake on Stoneley wave slowness and attenuation in an attempt to reduce the uncertainty surrounding permeability characterisation which arises through lack of knowledge of the mudcake stiffness. The formulation of the mudcake stiffness parameter and its physical relevance is discussed in section 7.3, and the effect of the mudcake both on the propagation of the Stoneley wave along the borehole and on the initial burst is studied.

As mentioned previously, several studies into the effects of a fracture on the Stoneley wave and the associated electrokinetic phenomena have been carried out (Haartsen & Pride, 1997; Mikhailov et al., 2000; Pride & Morgan, 1991; Tang et al., 1991; Zhu et al., 1999). The general findings were that the fracture causes reflection of the seismic waves, including compressional, shear and Stoneley waves, and also the generation of an electromagnetic wave associated with the arrival of the Stoneley wave at the fracture opening, which propagates at light speed and is thus seen at all detectors in the borehole simultaneously. The applicability of the present model to fractured porous media is discussed in section 7.4. The acoustic problem, involving wave transmission and reflection at the fracture boundary, is adequately treated by the model. The electric problem by contrast is not well described by the finite-element implementation of the streaming potential equation (Eq. 5.24). The necessary adjustments to the Biot equations for an (admittedly crude) approximation to the behaviour of a fractured porous medium are described, and the implications for the NEF method in the light of this modelling are discussed.

7.2 Layered Porous Media

In section 6.3.1 it was found that the normalised electric field (NEF) was dependent on permeability, but that no clear porosity dependence was evident, a finding which contradicts the conclusions of Mikhailov et al. (2000) who find that porosity, and not permeability, is the critical parameter. The limitations of the model used by Mikhailov et al. have already been described (zero solid displacement and no consideration of permeability as distinct from porosity), but so far the results presented here have not been compared directly with those of Mikhailov et al. The NEF data resulting from a large number of individual, homogeneous models have been presented, whereas Mikhailov et al. make their conclusions based on the varying Stoneley wave in a single, layered formation model. In this section layered formation models are used to compare the two theories and, more generally, to investigate the effects of changing material properties on the Stoneley wave.

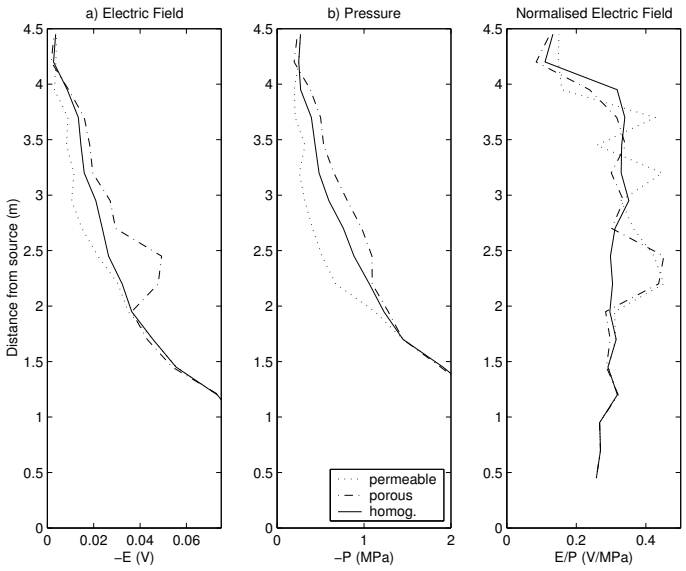

Figure 7.1: (a) Electric Field, (b) Pressure and (c) Normalised Electric Field for models including a contrasting layer between 2 and 2.5 metres above the source (see main text for details). These results may be compared to those of Mikhailov et al. (2000) who find that the normalised electric field is dependent on porosity.

7.2.1 Effect of a contrasting layer on the Stoneley wave

Two models are set up to investigate the effects of formation layering. In both cases the majority of the formation has a porosity of 10% and a permeability of 1mD, as in run 1 of the standard cases (see Table 6.1). Each model also has a contrasting horizontal layer, 0.5m thick, intersecting the borehole between 2 and 2.5m above the source. In the first case this layer has a higher permeability of 10mD (ϕ=10%), while in the second case the layer has an increased porosity of 30% (k=1mD). Fig. 7.1 shows the Stoneley-related maximum electric field magnitude E, maximum pressure magnitude P and NEF E/P measured along the borehole for these two cases, and with data from the homogeneous run 1 for comparison. The detector spacing is reduced to 0.25m to improve the resolution.

In the first model, with a high permeability layer, the electric field and pressure both drop as the Stoneley wave passes the layer, due to the increased fluid flow into the formation and resulting loss of energy in the borehole. The NEF, however, increases at this point as expected from Fig. 6.4, before returning to approximately the value of the homogeneous case higher in the borehole. Due to the increased attenuation of the Stoneley wave through the highly permeable layer, the peak amplitudes in both electric field and pressure are small, causing the seemingly erratic behaviour of the NEF far from the source.

In the second model, with a highly porous layer, the responses of the electric field and the pressure differ as the Stoneley wave passes the layer. Fluid flow remains largely unchanged, as shown by the small deviation of the pressure data from the homogeneous case. The electric field is significantly increased in the neighbourhood

of the layer, reflecting the larger fluid/solid contact area and therefore the greater amount of charge moved. Note that if the model is simplified and zero solid displacement is assumed in the formation, the fluid flow velocity is inversely proportional to the porosity for a given pressure gradient. However, Eq. 5.24 contains a further second power of the porosity due to Archie's Law, and thus the given pressure gradient induces a larger electric field. Similar to the first case, the NEF is increased as the Stoneley wave passes the porous layer, in this case by a similar amount as in the first model.

In both of these models the increase in the NEF is restricted to the neighbourhood of the contrasting layer. Below and above the layer the NEF is consistent with the homogeneous case. This suggests that this technique can be used to determine porous or permeable inhomogeneities along the length of a borehole. It is not clear at this point, however, how a distinction may be made between a porous or a permeable layer, although since the two are often related, such a distinction may not always be necessary.

An important factor in the technique of using the NEF, E/P, as above is the way in which the electric field E is calculated. The definition above (Eq. 6.1) does not strictly give the electric field at detector $D1$, but is an approximation of the electric field at the midpoint between $D1$ and $D2$. Having electrodes close enough together to measure the electric field accurately at a point may make surveying an entire borehole unfeasible, or make unreasonable demands on the data recording equipment. The main disadvantage of using spaced electrodes is that the thickness of the thinnest resolvable layer will be dependent on the electrode spacing. Figs. 7.2 and 7.3 show the results of tests designed to investigate this dependency. In each model a contrasting layer was positioned within a homogeneous background formation. The thickness of the layer was 0.1m, 0.5m, 1m or 2m, always positioned so that the bottom of the layer was 1.5m above the source, and the detector spacing in the borehole was 0.5m. The data from a homogeneous formation model has been included for comparison in each model.

In the first model (background: ϕ=10%, k=1mD; layer: ϕ=30%, k=100mD; Fig. 7.2) the 0.5m, 1m and 2m layers are picked out well by the NEF, and as before, above the layer the values are similar to those from the homogeneous model. The 0.1m layer does not make a significant difference to the NEF. The layer appears 0.5m above its true position, a result of the electrode spacing and the method for calculating the electric field E as described above.

In the second model (background: ϕ=30%, k=100mD; layer: ϕ=10%, k=1mD; Fig. 7.3) the definition of the 0.5m layer by the NEF is less clear than before. The 1m and 2m layers are depicted by a drop in NEF over the relevant interval, and again the 0.1m layer does not feature significantly. These results suggest that the minimum layer width resolvable by this technique is approximately equal to the electrode spacing, although resolution may be better where the layer is more permeable and porous than the background and less accurate where it less so.

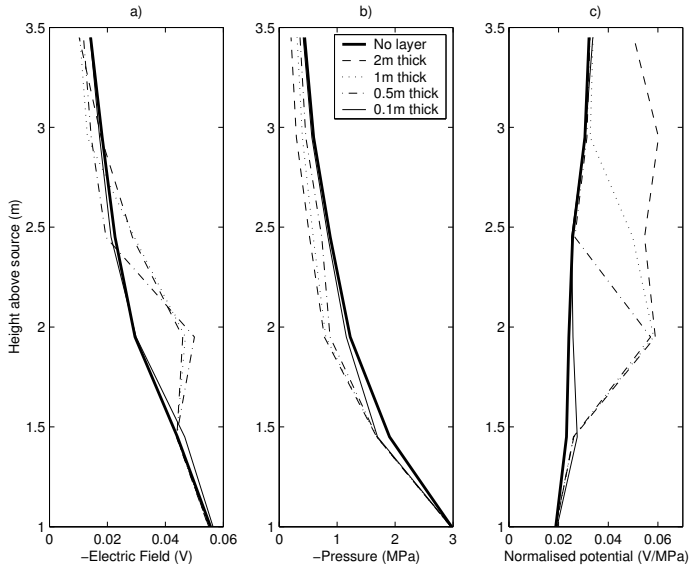

Figure 7.2: Graphs showing the behaviour of the Stoneley-related (a) electric field, (b) pressure and (c) normalised electric field for models with a contrasting layer of varying widths intersecting the borehole. The bottom of the layer is 1.5m above the source. Detector spacing: 0.5m. Background formation: ϕ=10%, k=1mD; Layer: ϕ=30%, k=100mD.

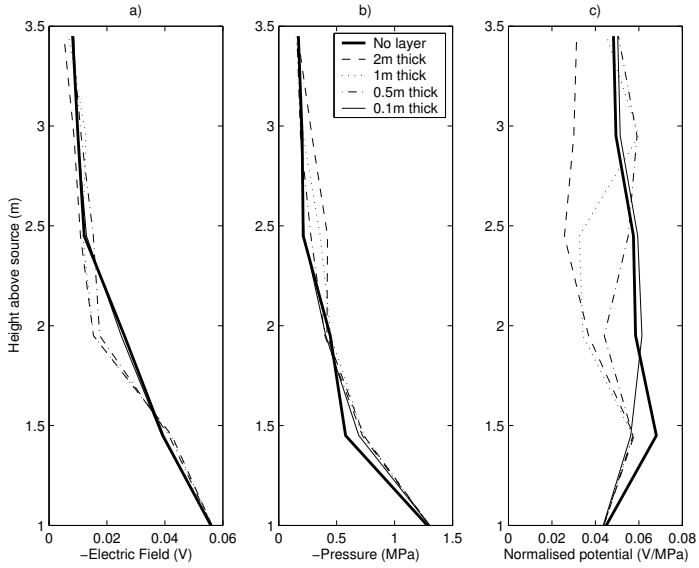

Figure 7.3: Graphs showing the behaviour of the Stoneley-related (a) electric field, (b) pressure and (c) normalised electric field for models with a contrasting layer of varying widths intersecting the borehole. The bottom of the layer is 1.5m above the source. Detector spacing: 0.5m. Background formation: ϕ=30%, k=100mD; Layer: ϕ=10%, k=1mD.

7.2.2 Moving the array past a contrasting layer

Having established that the NEF method is sensitive to changes in porosity and permeability along the length of a borehole, here a study is made of what might be seen in a real borehole logging experiment. The main difference is that the electrode and hydrophone array is now fixed at a certain distance from the source and this combination is moved past a single layer in the formation.

The properties of the background formation are $\phi = 0.3$, k=1mD, contrasting with the layer (0.5m thick) which has a higher permeability of k=100mD, and the same porosity. The electrode pair used for this modelling are positioned closer together than before to improve the resolution of the measurements. The lower electrode is 2m above the source in the borehole, with the upper electrode 30cm higher up. The 'short' source is used once again, at a frequency of 1kHz, and the peak amplitudes of the Stoneley-related electric field and pressure are measured. The electric field, pressure and NEF are plotted against the position of the lower electrode with respect to the layer, in Fig. 7.4. Three hydrophone positions are used: coincident with the lower or upper electrode and at the dipole mid-point, which are plotted as 'near', 'far' and 'mid', respectively in Fig. 7.4. Using these three positions allows examination of which one gives the best indication of the thickness and location of the embedded layer. In Fig. 7.4c the values of the normalised electric field measured in a homogeneous formation with ϕ=0.3, k=100mD are plotted, with solid green, blue and red lines corresponding to the near, middle and far hydrophone positions, respectively. An important aspect of the NEF method is that in a contrasting layer the value of the NEF should be close to that for a homogeneous formation of the same material properties. This would allow an easier interpretation of the NEF in terms of permeability.

The profiles given by using each of the three hydrophone positions in the calculation of the NEF are substantially different from each other. Positioning the hydrophone at the level of the lower electrode, nearest the source, has only a small effect on the NEF as the receiver array passes the layer. This is because, looking at Figs. 7.4a and b, the electric field and pressure curves are very similar in shape, resulting in a ratio which remains mostly unchanged. The NEF curve also fails to reach the value corresponding to a homogeneous formation with the properties of the layer, plotted by the green solid line. Therefore it does not seem that this position is useful in this method. Using a hydrophone at the mid-point position, 2.15m above the source, shows a clear change in NEF, and defines both the location and thickness of the layer with increased accuracy. The three points at which the NEF rises to around 0.05V/MPa correspond to the hydrophone being opposite the layer. Again, however, the peak of the curve does not reach the value appropriate to the embedded layer. This hydrophone position, therefore, is capable of locating, but not accurately characterising the layer. Using a hydrophone positioned by the upper electrode, furthest from the source, the electric field and pressure curves are different in shape: the pressure begins to fall when the lower electrode is still 0.5m beneath the bottom of the layer whereas the array must be moved up another 0.5m before the electric field responds. The resulting NEF, however, shows a large change in amplitude moving past the layer but is not well defined in terms of locating

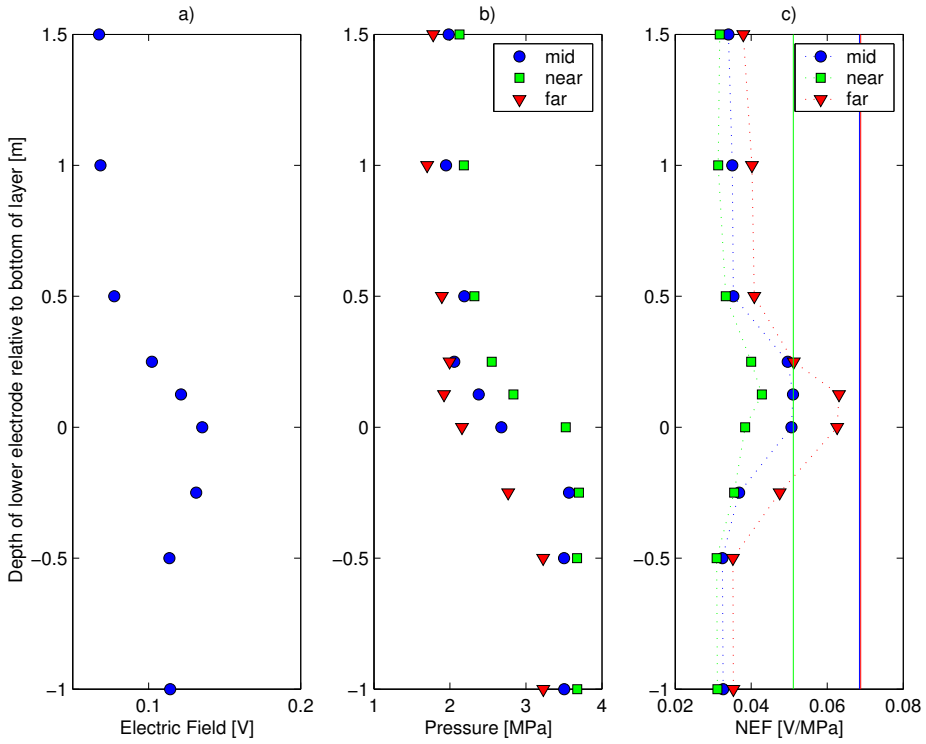

Figure 7.4: Results from an experiment mimicking the movement of the receiver array past a contrasting layer in the formation: a) the amplitude of the Stoneley-related electric field using a 30cm dipole with the lower electrode 2m above the source, b) the Stoneley-related pressure amplitude using three hydrophone positions, and c) the normalised electric field measurements. Also plotted are values of the normalised electric field for a homogeneous formation with ϕ=0.3, k=100mD, for each of the hydrophone positions. The vertical axis shows the position of the lower electrode with respect to the bottom of the layer. Therefore the lower electrode is opposite the layer between 0m and 0.5m in this diagram.

the thickness of the layer. It might seem that the layer extends over more than 0.5m and, from the shape of the curve, that the permeability was highest in the centre of the layer rather than being uniform throughout. The peak value of this curve does approach the value appropriate for the layer however, so it would seem that this hydrophone position is suitable for characterising, if not accurately locating the contrasting layer.

The success of any such experiment will, of course, depend on the nature of the formation and the geometry of the tool. A tool with a narrow-spaced dipole used in with high spatial resolution along the length of the borehole will clearly characterise layers better than a wide-spaced dipole tool used with large intervals between shots. This examination shows that positioning the hydrophone mid-way between the electrodes may enhance the ability of the NEF method to locate heterogeneities in the formation, while positioning the hydrophone by the upper electrode enables characterisation of such heterogeneities.

7.3 Mudcake

7.3.1 Theory of mudcake

Mudcake, or filter cake, results from the drilling process. The pressure in the borehole fluid during drilling is maintained at or slightly above the expected hydrostatic pressure at depth, by adding clay minerals to the water. While the overpressure causes water to move from the borehole into the formation, the clayey mud is filtered by the porous rock and is left as a deposit along the borehole wall. Eventually this mudcake is removed by the pressure of the pore fluid during production, but shortly after drilling the presence of the mudcake complicates acoustic logging as it inhibits the 'natural' flow of fluids into and out of the formation. Mudcake is most commonly modelled as a membrane-like layer with zero thickness which can be assigned a certain stiffness W_{mc} (Liu & Johnson, 1997; Brie et al., 2000) governing the extent to which the mudcake can flex in and out of the pores of the formation. The volumetric approximation $\hat{W}_{mc}$ to the surface parameter W_{mc} is included in Eq. 5.1. For explanation of this relationship, see Pain et al. (2005). Low stiffness values approximate the open hole case, in which the fluid and solid phases move as if there were no mudcake present. High stiffness values transfer more of the energy from the borehole fluid to the solid phase, and less to the pore fluid phase, reducing the effects of the formation permeability. As $W_{mc} \rightarrow \infty$ the closed hole case is approximated in which the borehole fluid cannot communicate with the pore fluid at all, as would be the case were the borehole cased or otherwise sealed with a solid material. Stiffness is measured in GPa/cm, with reasonable values ranging from 0 to 10 GPa/cm (Tang, 1994; Liu & Johnson, 1997).

7.3.2 Modelling results

First, the influence of the mudcake on the effective permeability of the formation must be established. Ideally, the presence of mudcake would not drastically influence the propagation of the Stoneley wave for all

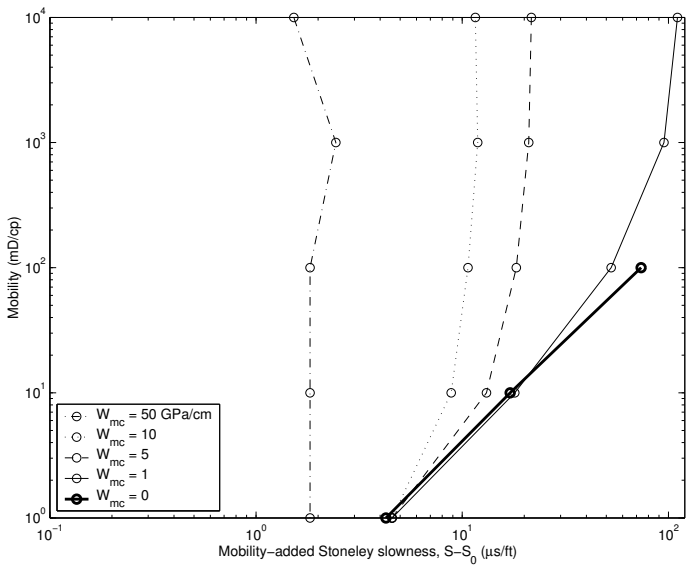

Figure 7.5: The added slowness due to mobility of the Stoneley wave for models with varying mudcake stiffnesses. The Stoneley slowness is compared to that in a model with permeability $k = 0.01$ mD. These results are similar to those given by Brie et al. (2000), showing that the mudcake only affects the Stoneley wave when the mudcake has high stiffness and when the formation is highly permeable.

but the highest stiffness values. Indeed, Liu & Johnson (1997) state that 'this mechanism reduces, but does not eliminate, the effects of formation permeability on the tube wave'. Brie et al. (2000) find that their analytical solution gives just this result: that the Stoneley wave 'mobility-added slowness' is not greatly affected for low stiffness mudcake, and that for stiffness values at the top of the expected range, 10 GPa/cm, there is little effect while the mobility remains less than 100mD/cp. In Fig. 7.5 the results of modelling using MAPEK are presented. The results are very similar to those of Brie et al. (2000), despite the differences in the source frequency (here a 1 kHz source is used) and in the properties of the rock and fluid. It is important also to note that in this model the mudcake is represented as a zero-thickness membrane which contrasts with the finite-thickness elastic mudcake used by Brie et al. The present model is therefore able to represent the effect of mudcake accurately.

Next the effect of the mudcake on the NEF E/P is investigated. In section 6.3.1 the NEF, in the absence of mudcake, was found to increase with permeability but, as mentioned above, including the mudcake can reduce the effect of high permeabilities, especially when the mudcake is stiff. Fig. 7.6 shows the NEF versus permeability including a mudcake membrane with stiffness W_{mc}=1GPa/cm.

The values of NEF are reduced slightly from the non-mudcake case, even at low permeabilities. At high permeabilities, values above 10mD, the NEF no longer increases with permeability. Using a much stiffer mudcake with W_{mc}=10GPa/cm the reduction in NEF is even greater. Fig. 7.7 shows that with such a stiff

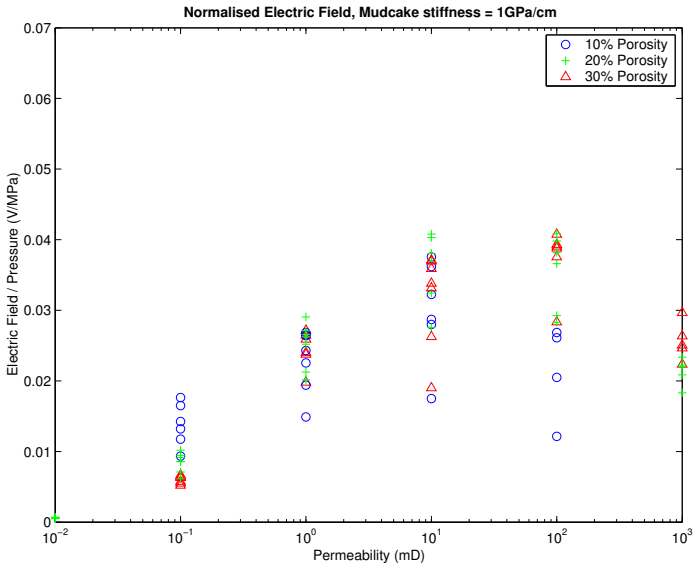

Figure 7.6: The relation of normalised electric field to permeability as measured by detectors in the borehole, with a flexible mudcake (W_{mc}=1GPa/cm) lining the borehole. The effect of the highest permeabilities is reduced by the presence of mudcake, but the normalised electric field still increases with permeability for $k \lesssim$10mD. Compare with Fig. 6.4 in which W_{mc}=0.

mudcake there is no evident relationship to the permeability.

Given this evidence, it would be necessary to minimise the stiffness of the mudcake in order to use the NEF method for formation permeability characterisation. However, the composition of the drilling mud is constrained by other factors, and thus it would probably not be feasible to alter the mud for the purposes of the NEF method. As an alternative to minimising the mudcake stiffness, early investigations (J. Singer, private communication) suggest that the effect of the mudcake may vary with frequency. By changing the frequency of the acoustic source the mudcake stiffness could perhaps be deduced, and thus eliminated as an unknown.

7.4 Fractures

An interface created by a fracture is expected to alter the nature of the transmitted wave, as well as causing a reflection dependent on the angle of incidence. Here a simple fracture is modelled intersecting the borehole perpendicular to the borehole axis, and the way in which the results found for the homogeneous formations are changed by the presence of a fracture is studied.

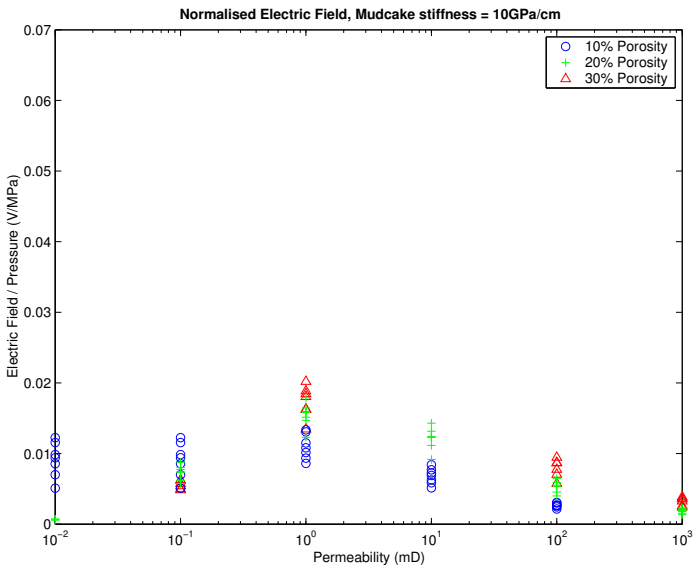

Figure 7.7: The relation of normalised electric field to permeability as measured by detectors in the borehole, with a stiff mudcake (W_{mc}=10GPa/cm) lining the borehole. The stiff mudcake reduces the effect of permeability so that the normalised electric field is no longer indicative of formation permeability. Compare with Fig. 6.4 in which W_{mc}=0.

7.4.1 Fracture modelling methods and considerations

Numerical modelling of a rock fracture may be achieved through a variety of means; a boundary condition may be enforced along the fracture, perhaps similar to that which used to model the mudcake, a material may be substituted which averages the behaviour of the fracture over a small area (although this would probably require anisotropic material properties), or the fracture may be explicitly modelled as a thin layer of fluid between the porous rock layers. Here the fracture will be modelled explicitly, exploiting the natural versatility of finite elements, which with an adaptive mesh could be used to model wave propagation in a formation with an arbitrary fracture distribution.

For the acoustic problem, explicit modelling of the fracture provides the necessary interface in the formation to split the energy of a propagating wave into reflected and transmitted parts. The contrast in material properties (density and velocity) between the porous formation and the fracture fluid will govern the proportion of energy that is reflected (Telford et al., 1990, pg. 155). Retaining focus on the Stoneley wave, in Fig. 7.8 the amplitude of the (acoustic) Stoneley wave is plotted as it travels along the borehole, passing a fracture at 1.95m. The fracture is 1mm wide, and is modelled by including a layer in the formation which is filled with fluid identical to the borehole fluid. Amplitudes from runs 1 (ϕ=0.1, k=1mD), 5 (ϕ=0.3, k=1mD) and 7 (ϕ=0.3, k=100mD) are shown, and it can be seen that the nature of the formation has a strong effect, not only on the attenuation of the Stoneley wave with distance, but also on the change in amplitude at the fracture and on the strength of

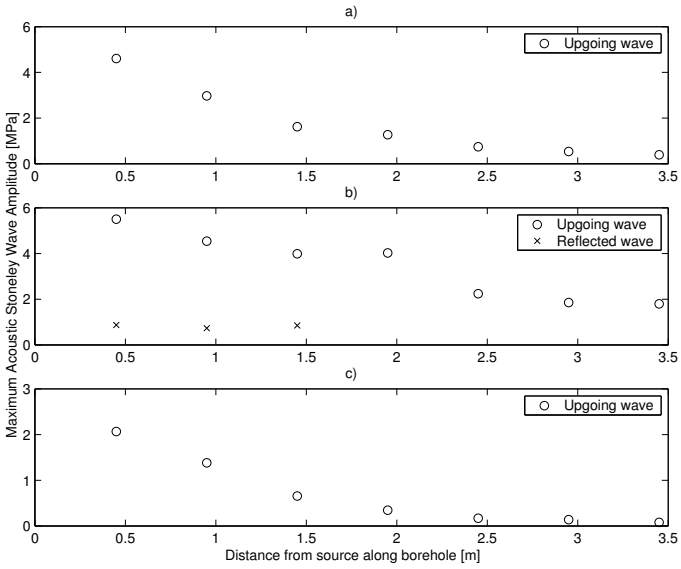

Figure 7.8: Stoneley wave amplitudes measured by detectors along the borehole for a) model 1, b) model 5 and c) model 7, with a 1mm fracture positioned 1.95m from the source. In model 5 a sharp reduction is seen in the amplitude of the transmitted wave (continuing to the right) at the fracture, and a significant reflected Stoneley wave is also present (moving left).

the reflected Stoneley wave. In runs 1 and 7 (Fig. 7.8a and c) there is very little change in the amplitude of the Stoneley wave, other than the expected attenuation for an unfractured formation. There was no discernible reflected Stoneley wave in either of these cases, although the low amplitude of any reflected wave that might be present would probably mean it would be indistinguishable amongst the other various signals in the borehole. Some formal wave-form processing would be helpful in finding the reflected waves in these cases. In run 5 by contrast, the fracture has a large effect on the Stoneley wave. The amplitude measured at 2.45m is a little over half that measured by the detector opposite the fracture at 1.95m, and the reflected Stoneley wave measured at 1.45m has over 20% of the amplitude measured at the same detector.

For the electric problem, modelling the passage of a Stoneley wave past a fracture is more complicated. In reality, a fracture offers a large surface area of mineral in contact with mobile fluid, and thus has the capacity for large electrokinetic effects. In finite-element numerical modelling, material properties are assigned to the nodes of the mesh and (linearly) interpolated between the nodes. Therefore the precise edge of a physical feature is not clearly defined, but occurs over the width of an element in the mesh. In the case of the boundary of a fracture, one node would be ‘in the formation’ while the adjacent node would be ‘in the fracture fluid’. The boundary of the fracture, on which resides this large accumulation of surface charge, cannot be represented in this way, and therefore the natural representation of the fracture with finite-elements may be inadequate for the electric problem. One solution may be a boundary-condition-type treatment, as was used above in the modelling of the

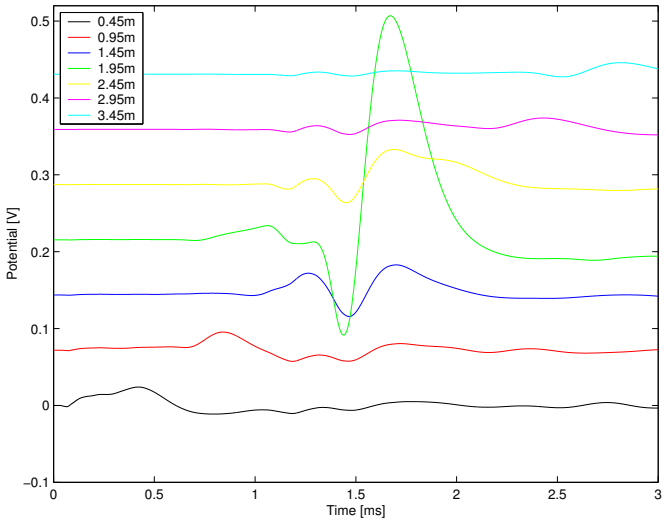

Figure 7.9: Potential logs measured in the borehole for a model including a 1mm fracture opposite the detector at 1.95m from the source. The parameter b is set to zero along the edge of the fracture, resulting in a large electrokinetic effect as the Stoneley wave passes.

mudcake, but some insight may be gained by considering the physical phenomena encountered at the fracture boundary.

The property of the fracture boundary which is not represented by the natural finite-element method, is that which allows the fluid and solid phases to move relative to one another, thus moving the charge layer next to the mineral surface. The parameter controlling the relative movement of the phases in the Biot equations (Eqs. 5.1 and 5.2) is b, the drag coefficient dependent on porosity and fluid mobility. Setting b=0 on the nodes along each side of the fracture boundary, both in the porous formation and in the fluid, allows the two phases to move increasingly out of phase. Admittedly, this is not a rigorous treatment of fracture modelling by any means, especially as the poroelastic equations become poorly defined with b=0 in the fluid, both sides of Eq. 5.1 being equal to zero. However, it might allow some of the nature of Stoneley wave behaviour around an open fracture to be captured.

Fig. 7.9 shows the potential logs measured at the detectors in the borehole, for a formation with a 1mm fracture positioned at 1.95m from the source. In comparison with Fig. 6.2, which shows the potentials measured in the borehole with a homogeneous unfractured formation, the major feature is the potential measured at the detector opposite the fracture, and associated with the arrival of the Stoneley wave. The potential propagates throughout the domain, and is measured at all detectors, most noticeably at the detectors immediately above and below the fracture, at 2.45 and 1.45m from the source, respectively. The amplitude of this potential, around 300mV, is considerably larger than that of the Stoneley waves measured elsewhere in this model, which are of

the order of a few tens of millivolts. If this were an accurate representation of the behaviour of the Stoneley wave at a fracture, then monitoring the electrical signals associated with the Stoneley wave would clearly be an excellent way of detecting large open fractures. Indeed, Garambois & Dietrich (2001) and Mikhailov et al. (2000) measure propagating electromagnetic signals associated with a Stoneley wave interacting with a fracture intersecting the borehole. The amplitude of the signals in both cases are of a similar magnitude to the Stoneley-related electric fields. Added together, this would roughly double the electric signal measured close to the fracture, perhaps somewhat less drastic than the large signal shown in Fig. 7.9, but nevertheless a significant feature in a borehole log.

7.5 Conclusions

The inclusion of contrasting layers into the formation model has shown that the NEF method, which was previously shown to be sensitive to permeability, can be used to locate and characterise permeable zones. Careful positioning of the hydrophone in relation to the electrodes may aid either characterisation or location of such a zone, but good measurement resolution and a reasonably narrow electrode spacing will also help considerably. Mudcake has been shown to reduce the effect of permeability on the measured data, and unfortunately may most drastically reduce the ability of the NEF method to characterise the most permeable formations, which are particularly valuable in a reservoir engineering context. The current method for modelling of fractures has limitations, particularly in adequately representing the electrical problem. By a rough approximation technique it has been shown that a propagating electromagnetic wave may be measured simultaneously by detectors along the borehole when the Stoneley traverses a fracture intersecting the borehole.

Chapter 8

Borehole Electroseismics - Field experiments and validation

8.1 The field site

In mid-June and again in mid-August 2004, field trips were undertaken to a site approximately 800m north-west of Bloreheath, Staffordshire, UK to measure pressure and electrical response to a seismic source in a borehole. The borehole known as T17 is situated in the north-west corner of a field on the south side of the B5415 (OS Grid Ref: 370515E 335550N, Lat/Long: N52:54:60 W2:26:24), as shown in Fig. 8.1, and at an elevation of approximately 105m above mean sea level. The borehole has a steel casing to a depth of 6m, and also extends 0.25m above ground. It is to this height, 0.25m above ground level, that depth measurements are referred. The borehole lies within 5m of a minor road, the B5414, and within 20m of a small stream which flows westwards into the River Tern, and on to the Shropshire Union Canal. Care was taken to avoid taking measurements which might be affected by passing traffic or occasional aircraft, and any electrical signal related to the flowing stream, or filtration into it, was expected to be constant over the period of the experiment and thus could be disregarded. The site is also more than 150m from any overhead power line or building, so it is hoped that noise in the electrical data will be small.

8.1.1 Geology and log data

The Bloreheath borehole site is located near the upper boundary of lower Triassic Bunter sandstone. The British Geological Survey (BGS) has logged the borehole on previous occasions, and this data will be used to support our findings. Fig. 8.2 shows the BGS caliper, porosity and permeability logs for T17, from which it can be seen that the borehole wall is generally well intact, except for the interval around 22.5m depth, and

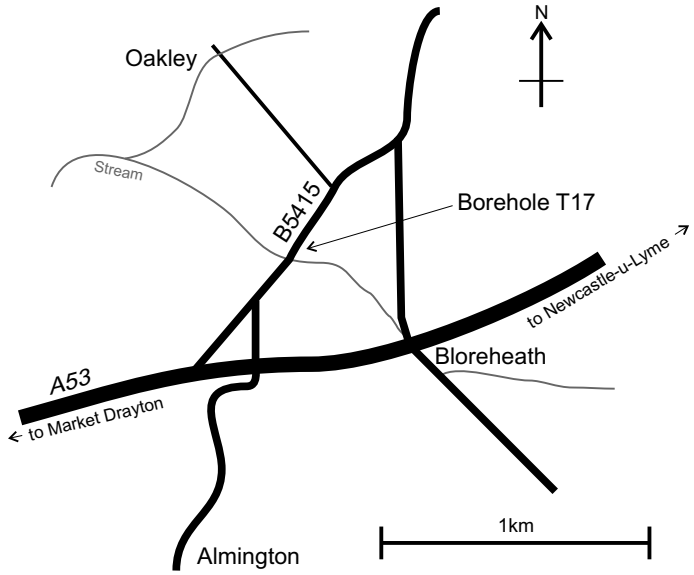

Figure 8.1: The location of the borehole T17, near Bloreheath, Staffordshire. The borehole is situated near a minor road and a small stream, but away from overhead power cables.

possible small areas of damage around 15 and 16.5m depth. The diameter of the borehole varies between approximately 16cm and 20cm, and so is similar to the borehole used in the modelling. The presence of the tool in the borehole will make the effective radius of the borehole smaller by approximately 2cm (Cheng & Toksöz, 1981), so in modelling these experiments a narrower borehole must be used. Two sets of data exist for the porosity log: a density log (assuming grain density $\rho_f = 2650\,\mathrm{kg/m^3}$ and water density $\rho_{fl} = 1000\,\mathrm{kg/m^3}$) and a neutron log. These logs are generally in agreement, although the density shows more variation in the lower half of the borehole. Horizontal and vertical permeability logs (made from core samples), although only sparsely populated, show values in the range 5-8900 mD, with the horizontal permeability consistently higher than the vertical.

8.1.2 Experimental set up

8.1.2.1 The sonde and hammer

For this experiment a simple sonde was designed (see Fig. 8.3), consisting of two hydrophones and two electrodes attached to a length of plastic tubing and suspended by ropes in the borehole. The electrode dipole separation was 0.3m, with a hydrophone positioned 0.1m above the upper electrode and attached to the supporting rope. A second hydrophone positioned at the bottom of the sonde, 90cm below the upper hydrophone, would allow calculation of the speed of the Stoneley, compressional and shear waves. Stiff plastic strips attached to the tubing ensured that the sonde remained centralised in the borehole, and pebbles in the lower end

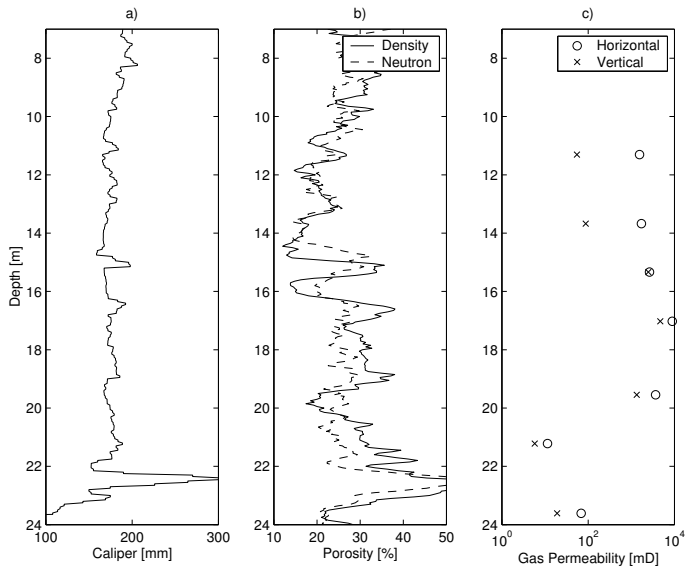

Figure 8.2: Data taken from BGS logs of borehole T17: a) a caliper log showing substantial damage to the borehole wall at 22.5m depth and possible minor damage around 15-17m, b) porosity logs from density and neutron surveys and c) horizontal and vertical gas permeability logs.

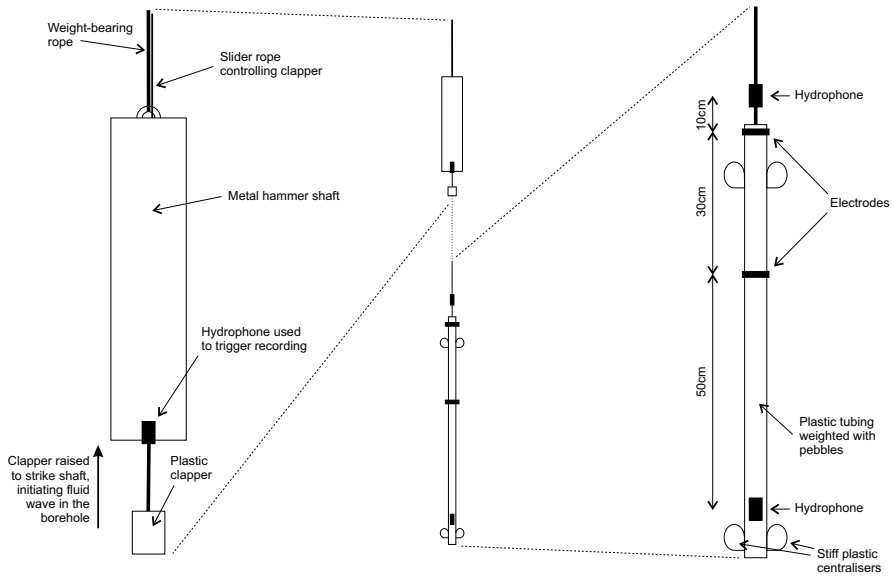

Figure 8.3: Diagram of the sonde designed for the Bloreheath borehole logging experiment. The sensor array consists of two hydrophones and an electrode dipole, attached to a length of plastic tubing. The seismic source is a slide hammer positioned above the array in the borehole. The array section is centralised using stiff plastic strips, and both sections are suspended by ropes.

of the tubing added weight to the whole array to help it descend easily. A slide hammer was used as the seismic source, and suspended above the sensor array in the borehole. This was operated manually by a tug on the slide rope. A hydrophone attached to the hammer was used to trigger the acquisition system, described below.

The borehole was logged from bottom to top as this would improve confidence that the sonde and hammer were at the correct depths. For the first shots the top electrode depth was 22.24m, and the hammer depth 19.86m, so that the initial spacing between the base of the hammer and the top electrode was 2.38m. The hammer was first raised by 0.5m, a new set of measurements were made, and then the sonde was raised by 0.5m to restore the original spacing, and so on. The final measurements were taken with the hammer at 7.36m depth and the upper electrode at 10.24m, giving a total of 50 logs, 25 using a spacing of 2.38m and 25 using a spacing of 2.88m.

8.1.2.2 Data acquisition system

The data acquisition system consists of a 100kHz analogue-to-digital converter which is read over three channels and displayed on a laptop computer. The three channels used in the A/D converter are each sampled at a frequency of 32.768kHz. By recording over 1 second (and therefore using 32,786 sample points), the Fourier transform of any one channel for analogue data will have a 1Hz resolution.

Each of the three analogue channels going into the A/D converter has different amplification and also some low-pass filtering in order to prevent the aliasing effect of sampled signals. The cut-off frequency of each of these is approximately 6kHz. Channel 1 of the system is the electrical signal channel, carrying the signal from the electrodes. It has a variable amplification range including x1, x10, x100, x1000 and x10000. The amplification of channels 2 and 3, which carry the upper and lower hydrophone signals respectively, are fixed at approximately 23dB (x14.1).

Downhole and on board the tool, the only active element in the electronics is a pre-amplifier stage which amplifies the electrical signal from the electrodes. Its gain is selectable to either x10 or x100. Being the most important signal, the electrical signal will typically have two sets of amplifiers, one downhole and one at the surface. This is necessary given the attenuation characteristics of the cable used. A significant amount of noise can also be coupled into the signal leads of these cables, which makes having an amplifier at the surface with a good signal-to-noise ratio even more important. The system is triggered to measure the analogue signal variation over all three channels, for a specified amount of time, using a hydrophone mounted opposite the striker on the hammer. At each depth six shots were recorded, with occasional extra shots required to compensate for temporarily noisy or otherwise obviously erroneous data.

8.1.2.3 Typical hydrophone log

A typical hydrophone log is shown in Fig. 8.4, along with the Fourier frequency analysis of the signal. The

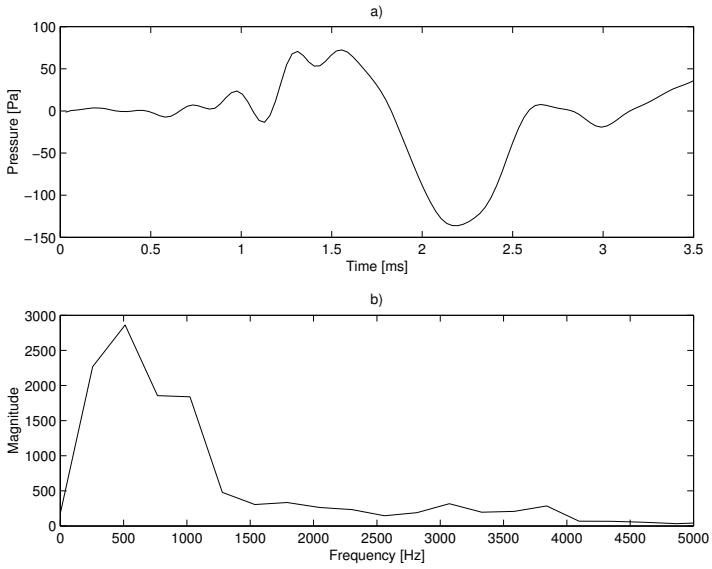

Figure 8.4: A typical hydrophone log using the manual hammer source: a) the log showing the Stoneley wave passing at around 2-2.5ms, and b) the Fourier frequency analysis of the log. The core frequency is shown to be in the region of 500Hz.

Stoneley wave is seen clearly, passing at 2-2.5ms and preceded by a number of smaller amplitude waveforms. The dominant frequency is shown to be around 500Hz, although the Stoneley wave frequency is slightly higher, at approximately 700Hz.

8.2 Analysis of logs from T17

The data gathered from logging borehole T17 can be separated into two parts, each relating to a separate part of the wave train. The first is the compressional wave velocity, measured between the upper and lower hydrophones positioned at either end of the sonde (see Fig. 8.3). This data can be combined with other logs to build a model of the borehole, in particular relating to the compressional and shear velocities of the formation and the rock grains. The second part is the Stoneley wave-related data, both acoustic and electrical which are compared with the results of modelling.

8.2.1 Velocity analysis of borehole logs

Compressional (p-wave) velocities are calculated by picking the arrival of the compressional wave at the upper and lower hydrophones. The identity of the wave-arrival was confirmed by raising the sonde and hammer into the steel casing, wherein the compressional velocities measured converged to the velocity of the casing. The p-wave was, however, not always clearly evident and so the profile is not densely populated. To improve the

reliability and repeatability of the measurements, measurements using both a 2.38 and 2.88m hammer-sonde separation were included.

The principal reason for gathering this information is so that a realistic profile of the borehole can be reconstructed for use in modelling. If the correct formation velocities and grain densities are used, then it is possible to have added confidence in analysis and modelling of the borehole Stoneley wave and the related electric field. From the compressional velocity data the compressional velocity of the rock grains c_s^p and the shear velocity of the formation c_f^s can be calculated via the velocity ratio $\alpha = c_s^p/c_f^s$. Two formulae which are commonly used for water-filled porous rocks and which are particularly suited to soft formations are used here, namely

$$c_s^p = \frac{c_f^p}{1 - 1.5\phi}, \tag{8.1}$$

which gives the grain compressional velocity in terms of the formation compressional velocity and the porosity (Raymer et al., 1980), and

$$\alpha = 1.6 + 0.0017A(\frac{1}{c_f^p} - \frac{1}{c_s^p}) + 0.0001A(\frac{1}{c_f^p} - \frac{1}{c_s^p})^2. \tag{8.2}$$

Here the velocity ratio is calculated using the grain and formation velocities (Brie et al., 1995). It has been recast in units of m/s (rather than μs/ft) and so includes the conversion factor $A = 10^6 \times 0.3048$.

The measured and calculated velocity data are shown in Fig. 8.5. In calculating the grain velocity c_s^p the porosity data used is from the density log. The grain compressional velocity recovered lies between approximately 2.5 and 4km/s along most of the borehole, increasing toward 6km/s right at the bottom. This increase is likely to be due to the high porosity related to the damaged area of the borehole wall rather than a real increase in the grain compressional velocity. The calculated formation shear velocities lie between 1 and 1.5km/s.

8.2.2 Stoneley wave acoustic and electrical data

The Stoneley wave data is measured by the upper hydrophone and by the electrode dipole. As in chapter 6, the peak amplitude of the Stoneley wave is recorded where possible, and the electric field measured by the dipole divided by the pressure to obtain a normalised electric field. (The 'electric field' is here calculated as the potential difference $\psi_{E1} - \psi_{E2}$ between the upper and lower electrodes $E1$ and $E2$ respectively.) Previously it was found that the normalised potential increased with the permeability of the formation for $0.1\text{mD} \lesssim k \lesssim 1\text{D}$, and then dropped slightly above this range (see Fig. 6.4). The logs from T17 show permeability values from around 5mD up to nearly 10D, so a considerable variation may be expected in the normalised electric field. From the diagram showing the sonde (Fig. 8.3) it can be seen that in any one log the hydrophone is positioned above the electrode dipole. Ideally, the hydrophone should be aligned with the mid-point of the dipole, so in calculating the normalised electric field the logs are re-aligned so that the hydrophone and electrode data are recorded, as much as possible, at the same depth.

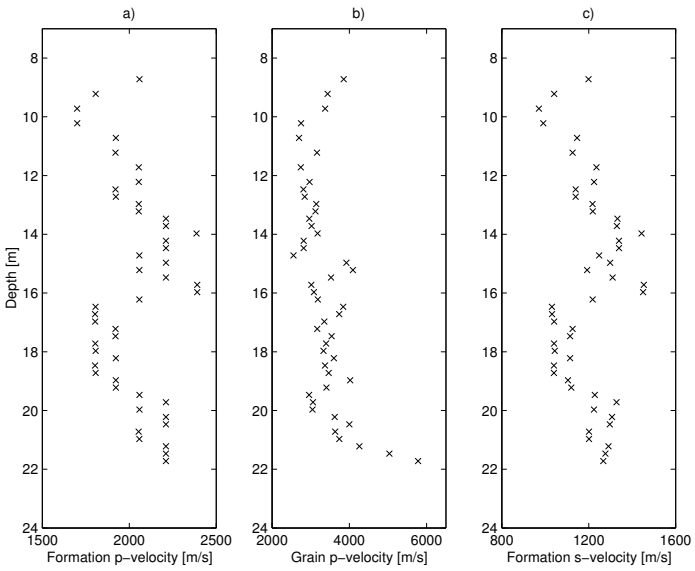

Figure 8.5: Measured and calculated compressional and shear velocities from borehole T17: a) the formation compressional velocity measured using the upper and lower hydrophones, b) the compressional velocity of the rock grains calculated from the measured velocities with Eq. 8.1, and c) the formation shear velocity calculated from the compressional velocities with Eq. 8.2.

Since the borehole was visited twice, two sets of data exist for T17. The Stoneley-related pressure, electric field and normalised electric field data from the first visit are plotted in Fig. 8.6. The pressure data correlates reasonably well with the porosity log: moving down from the top of the borehole the porosity decreases and the pressure amplitude increases; and below 17m the sharp rise in porosity is accompanied by a significant drop in pressure amplitude. In the electric field data we see the opposite relationship, with the electric field falling where the porosity is low, but showing the largest amplitudes in the middle region of the borehole where the permeability is highest.

The results from the second logging visit are shown in Fig. 8.7, where the depth interval between shots is reduced to 0.25m. This time the logging continues up into the casing, where the pressure increases and the electric field drops as expected. Around 9 metres a small rise in the electric field accompanied by a low pressure measurement leads to a large normalised electric field reaching 5V/MPa at its peak. The lower regions of the logs are similar to those from the previous visit, showing values of normalised electric field of around 1-2V/MPa.

The normalised electric field measurements from both visits (using the 2.38m separation log from visit 1) are plotted in Fig. 8.8a, and the normalised electric field from the second visit is plotted with the formation (density) porosity and permeability in Figs. 8.8b and c respectively. The two normalised electric field logs are in agreement along much of the borehole, showing the good repeatability of the experiment. The only

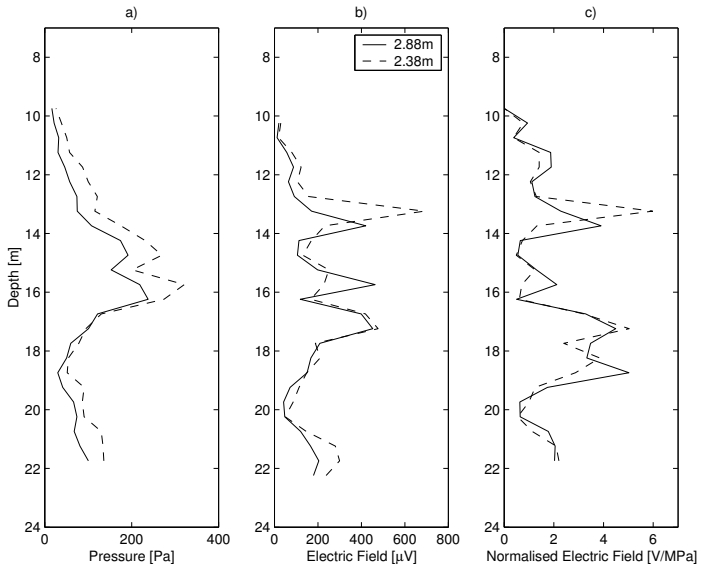

Figure 8.6: Measurements of the acoustic and electric amplitude of the Stoneley wave in borehole T17 for the two hammer-source separations, mid-June log: a) the raw pressure data from logging which will be influenced by the strength of the initial hammer blow, b) the electric field amplitude showing considerable variation along the length of the borehole, and c) the normalised electric field which is independent of the strength of the hammer blow.

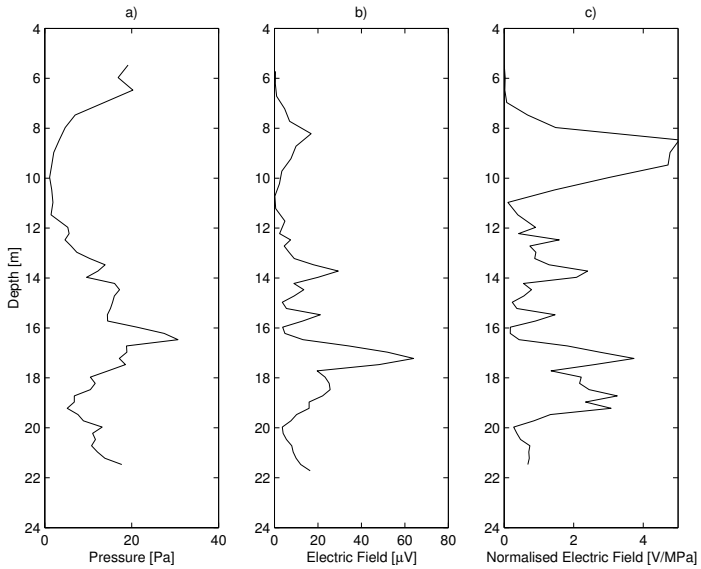

Figure 8.7: Measurements of the acoustic and electric amplitude of the Stoneley wave in borehole T17, mid-August log: a) the raw pressure data, b) the electric field amplitude, and c) the normalised electric field.

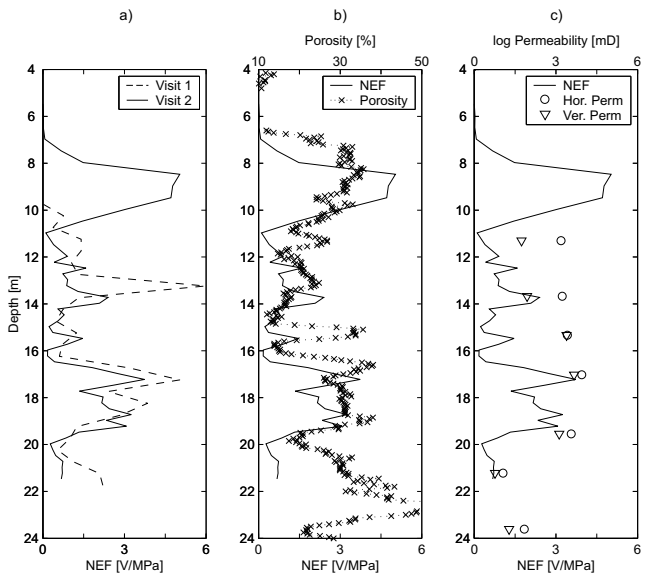

Figure 8.8: a) Normalised electric field logs from the two visits to T17, b) the normalised electric field and porosity logs and c) the normalised electric field with horizontal and vertical permeability logs.

significant difference between the logs is the peak between 13 and 14m in the first log. In Fig. 6.4c a lower value is recorded at this depth with the 2.88m separation, so it may be concluded that the large peak shown in Fig. 8.8a may be an overestimate of the normalised electric field. Also note that during the first logging episode a significant electric field associated with the Stoneley wave was measured in the casing, while there was no significant electric field measured the second time. The reason for this is not clear, but possibly lies either in the design of the steel hammer, which was insulated in plastic tape for the first experiment but left uninsulated for the second, or in the repositioning of the pre-amplifier unit on the rope above the sonde rather than within the plastic tubing. In any case, there should be no Stoneley-related electric field measured in the casing due to the minimal relative fluid-solid movement in the formation behind the casing and the high conductivity of the casing and the hammer. Thus the measurements from the second visit are used to compare with porosity and permeability logs from borehole T17. The porosity log shows a reasonable correlation with the normalised electric field, in particular high values in the intervals 8-10m and 15-19m and low values between 10 and 15m. The zones of the borehole in which it is believed damage has occurred, at 15m and 22-23m, and which appear in the porosity log are not evident in the normalised electric field log. Excluding these points, a roughly linear increase in normalised electric field with porosity exists. The permeability logs (plotted here on a logarithmic scale) are admittedly sparse, but do correlate to a degree with the normalised electric field. Interestingly, it is the vertical permeability which shows better correlation than the horizontal permeability, with both giving a high value near the damaged zone at 15m depth. This may suggest that the characteristics of the Stoneley wave are dependent on the vertical permeability to a greater extent than on the horizontal permeability, but with so

little permeability data to work with it would be difficult to draw any firm conclusions.

8.2.3 Porosity/Permeability correlations

In order to interpret these results in the light of the conclusions from chapter 6, and in particular given the lack of substantial permeability data from T17, it is necessary to discuss the relationship between formation porosity and permeability. In this modelling these two important parameters have been treated as being independent of one another, in order to establish the influence each has individually, on the acoustic and electrical propagation characteristics of the Stoneley wave. In practice there is likely to be some degree of correlation between porosity and permeability such that they cannot truly be considered as independent. If the formation in question is unfractured but porous, then as the porosity increases the connectivity of the pores will also increase, in turn facilitating fluid flow through the pores and thus increasing permeability. Alternatively, if the formation is non-porous, but has open fractures, then the permeability profile will most likely resemble the porosity profile. For sandstones and chalks which may be both porous and fractured increases in porosity may be expected to be accompanied by a corresponding increase in permeability. Of course, lithology (e.g. shale/marl layers) and fracture aperture will both be important for any individual formation layer, but averaging over intervals of the order of a metre it may be reasonable to assume that increases in porosity may indicate permeable zones. Indeed, Leary & Al-Kindy (2002) find that porosity and permeability are 'closely linked rock properties', and present core data with a linear relationship between porosity and log(permeability), as well as noting that the strength of the correlation depends on the averaging length-scale. In relation to the results from borehole T17 shown so far therefore, the good correlation of the normalised electric field with porosity may well also indicate a correlation with permeability, and would therefore be in agreement with our earlier findings from chapter 6.

8.3 Modelling of T17 experiment

8.3.1 Model description and borehole logs

To further substantiate our conclusions, the finite-element model, MAPEK, is used to simulate the experiments described above. A 15m length of the borehole, between 10m and 25m depth, is divided into overlapping sections each 6m long, which can be modelled separately. In each case the source is positioned at the top of the section, with the upper electrode $E1$, hydrophone and lower electrode $E2$ 2.38m, 2.55m and 2.68m below the source respectively. (A hydrophone positioned between the electrodes is used to simulate the 'adjusted depth' measurements discussed in section 8.2.2.) The source frequency used is 0.6kHz, with a total duration of the 'extended' source of 1.8ms. The porosity and permeability logs from T17 are discretised into 0.5m sections with (5-point) average values assigned to each section. These discretised logs are plotted in Fig. 8.9a and b. In Fig. 8.9c the normalised electric field obtained from the visit to borehole T17 are plotted, with the values of

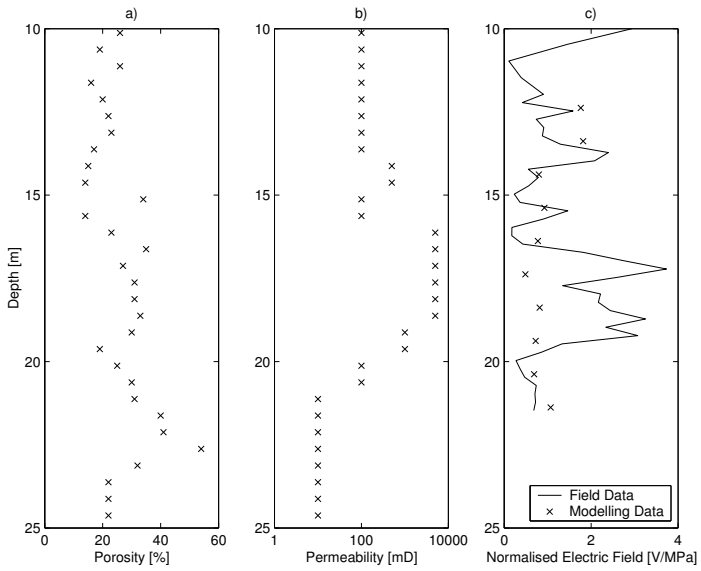

Figure 8.9: The synthetic model for T17: a) and b) porosity and permeability logs, respectively, used for modelling of experiment in borehole T17. These discretised logs are based on the logs shown in Fig. 8.2, and allow us to model the formation in discrete layers with the material properties averaged over a small interval. c) The normalised electric field from the field experiment plotted with values from the modelling.

normalised electric field from the modelling also marked. For each of the 10 data points from modelling, the electric field is calculated as the difference in potential $\psi_{E1} - \psi_{E2}$ between the upper and lower electrodes $E1$ and $E2$, as in the field experiment described above.

8.3.2 Interpretation of results

For the most part, there is good agreement between the values of the normalised electric field found in the field experiment at borehole T17, and the values found in modelling. Each of the model data points between 12 and 17m depth, and below 20m lies close to the field values. The fact that the NEF curve does not reflect the permeability profile may be due to the high values of permeability; in Fig. 6.4 it was seen that for permeabilities in the range 0.01-100mD the NEF increased with permeability, while above this range the increase was less clear. The range of permeabilities used in the earlier modelling was chosen to encompass the range likely to be found in the porous formations of a hydrocarbon reservoir. Therefore this problem of overly-high permeabilities may not persist in deep well applications.

In the range 17-20m, however, the high normalised electric field values recorded in the field are not replicated by modelling. In fact, from the modelling data it would not be apparent that this region had significantly different permeability or porosity values from the rest of the borehole, despite the very high permeabilities in the synthetic borehole log. In section 7.4 it was found that a wide, open fracture may cause an electric po-

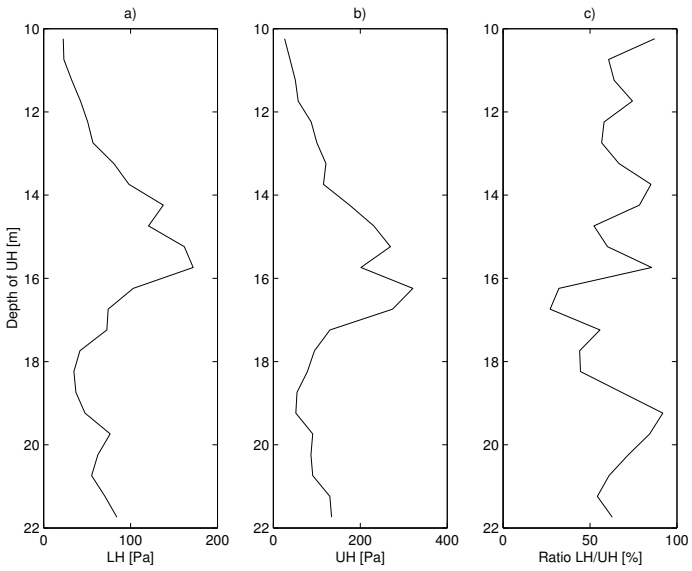

Figure 8.10: The amplitude of the the Stoneley wave as measured by a) the lower hydrophone and b) the upper hydrophone. The ratio of these amplitudes is plotted in c), showing a larger decrease in amplitude in the region 16-18m depth, and thus supporting the hypothesis that the formation is significantly fractured in this interval.

tential of several times the normal Stoneley-related magnitude to be measured at the nearby electrodes. Such a fractured zone would also result in a drop in pressure when the fractures lay between the acoustic source and the hydrophone. The hydrophone log shown in Fig. 8.7b does indeed show that when the source and hydrophone straddle this potentially fractured zone, i.e. when the hydrophone is at about 19m depth (and therefore the source is at 16.6m depth), the recorded peak pressure amplitude of the Stoneley wave is relatively small compared to the 5m section immediately above. In addition, such a fractured zone would cause a larger than normal drop in the amplitude of the Stoneley wave measured by the upper hydrophone and the lower hydrophone, positioned 90cm lower in the borehole. Fig. 8.10 shows the pressure amplitude of the Stoneley wave along the borehole as measured by both the upper and lower hydrophones on the first visit, and the ratio of the measurements as a percentage. Along the majority of the borehole, the lower hydrophone records an amplitude of 60-90% of that recorded at the upper hydrophone. When the upper hydrophone is positioned between 16 and 17m however, this falls to around 25%, suggesting that there is significant fracturing between 17 and 18m depth, leading to a loss of energy in the Stoneley wave. A similar process may be at work at the top end of the borehole, between 8 and 10m depth, where even smaller pressure amplitudes were recorded. The combination of the increased electric field and the lower pressure would increase the NEF, perhaps to the values seen in Fig. 8.7c.

8.4 Conclusions

In this field work it has been demonstrated that electrokinetic signals, in particular those related to the Stoneley wave, can be measured in the borehole. The recorded data show good qualitative similarity to the simulated borehole logs produced by the numerical model, and for the most part, good quantitative agreement as well. This confirms that the values used in the modelling for the coupling coefficient are appropriate for use in the field. Where the field data does not agree with results from subsequent modelling, there is reason to believe that the formation may be substantially fractured, which could explain high values of the normalised electric field.

Chapter 9

Conclusions and suggestions for further research

In this thesis four electrical methods for characterisation of geological formations have been discussed. A method for formulation of appropriate constraints to add model covariance to anisotropic resistivity inversion has been presented, along with a technique for calculating the optimum magnitude of these constraints for any resistivity inversion problem. Examples of inversion of synthetic and field data have shown that such constraints based on the known structure of the domain can significantly improve the accuracy of the inversion model, reduce susceptibility to common resistivity inversion problems, and improve the correlation of the inversion model with other geophysical data. This technique may be further improved by full implementation of the available covariance possibilities in the model, including independent constraining of the three eigenvalues and the three Euler rotation angles, and the use of adaptive meshing to improve the spatial resolution of small features in the model.

Two methods for identifying fluid distributions in a hydrocarbon reservoir have been investigated. Using the electrokinetic potentials generated by fluid moving through porous formations, it has been shown that an approaching water front may be detected before it reaches the production well. In conjunction with a current injection method, which measures the resistivity of the surrounding formation, it may be possible to use this information to regulate the production along the length of the borehole, thereby minimising water production and maximising the productivity of the reservoir as a whole. Such an 'Intelligent Well Technology' would have environmental as well as economic advantages, as the efficiency of production would be improved and the need for additional boreholes to be drilled reduced. A method remains to be developed for optimisation of the production regime given the electrokinetic or resistivity measurement, and considerable further work remains in investigating the behaviour of the coupling coefficient and zeta potential under two-phase conditions and for

a given lithology.

A field experiment was conducted to measure the SP response to water being pumped through a fractured chalk formation. A clear response to the commencement of pumping was seen in the electrical data, which was interpreted as being due to electrokinetic potentials. To correlate the results of modelling with those recorded in the field, it was necessary to use a much smaller coupling coefficient than that which was thought to be appropriate for a sandstone formation, based on published values.

Modelling of the borehole electroseismic experiment using the MAPEK finite-element model has provided extensive insight into the behaviour of the Stoneley wave and other wave modes. To investigate the dependence of Stoneley wave characteristics on parameters such as porosity and permeability, a method was used which required calculation of the normalised electric field (NEF). This method was found to have two principal advantages, first that the normalisation of the electric field by pressure allows measurements to be compared independent of the original acoustic source strength or the distance from the source to the electrodes or hydrophone. The second advantage is that this measurement is easily obtained in the field, using a pair of electrodes and a suitably positioned hydrophone.

Using this method it has been found that the NEF is sensitive to formation permeability, particularly in the range 0.01 to 100mD. The increasing trend of the NEF with permeability continues above this range for formations with high porosity (around 30%); lower porosity values make it difficult to distinguish the Stoneley wave clearly in the wave train. For a single formation with varying material properties it has also been found from modelling that the NEF is sensitive to both porosity and permeability. An increase in porosity of 10% has a similar effect on the NEF as an increase in permeability of one order of magnitude. Measurements made by an electrode pair and a hydrophone are diagnostic of the formation properties local to the array, as long as the Stoneley wave retains sufficient strength to be well-defined. The NEF method characterises the first few centimetres of the formation, with the exact distance dependent on frequency. Lower frequencies penetrate further, with up to 40% of the potential measured in the borehole being generated beyond 2cm into the formation at 250Hz.

The NEF method may be used to locate and characterise contrasting layers intersecting the borehole. Provided the vertical logging resolution and the electrode spacing are reasonably small, a moving source-receiver array may be used to characterise the changing permeability profile along the length of a borehole. Alternatively, a series of receivers positioned along the sonde may be used to characterise such layers with the NEF method, since the NEF has been shown to relate to the local properties of the formation. The presence of mudcake at the borehole reduces the effect of permeability on the NEF, but does not eliminate it entirely except for when the stiffness is at the top end of the proposed appropriate range. Taking measurements using a varying frequency at the source and calculating the ratio of the measurements between high and low frequency may provide a means by which the mudcake stiffness can be eliminated as a source of uncertainty in permeability characterisation, since the effect of mudcake has been seen to vary with frequency. For the purposes of validat-

ing the modelling, further determination of the properties of the mudcake and its effect on the propagation of both acoustic and electrical signals in the borehole will be important. Fractures cause reflections of the Stoneley wave to be seen in the borehole. Modelling shows an electrical event associated with the arrival of the Stoneley wave at the fracture, but it is not yet clear how realistic this model is. For this environment, it may be restated that further characterisation of the coupling coefficient and zeta potential is certainly required, particularly exploring the effects of the extreme environment found in a deep production well. The influence of temperature, salinity, conductivity and the presence of two distinct fluids on these electrical parameters may be critical in the evaluation of the viability of the NEF method in the oil field. Inclusion of the frequency-dependence of material properties including permeability and the coupling coefficient will be also be important, to enable accurate modelling of higher frequency experiments. For full generalisation of the method, an implementation of Maxwell's equations would be desirable to enable modelling of source frequencies up to and beyond the MHz range.

Field experiments in Totford and in Shropshire, and subsequent modelling, have shown considerable support for the conclusions drawn from preliminary modelling, which state that permeability may be diagnosed by the NEF method. Some features of the field logs remain to be fully explained, and sparse permeability logs do not enable accurate recreation of permeability profiles in synthetic models. However, the excellent agreement in magnitude of the NEF shows that the values used in modelling for the coupling coefficient are appropriate, and that both electrode and hydrophone logs from modelling are very similar to those obtained in the field. Analysis of the initial burst from modelling showed some variation with permeability, but it has not yet been possible to measure such a clear trend in field data.

Inversion of field data using an adjoint method would allow formation properties to be diagnosed using a few times the computational effort of a single forward model. Given that many of the important parameters including velocities, densities and especially porosity may be known at the outset, and given the sensitivity to permeability shown by the model, such an inversion procedure could converge quickly on a solution. Successive iterations of the inversion method would aim to minimise the difference between model output and the original data, using a conjugate gradient algorithm for example. Comparison could be made of logs recorded by electrodes and hydrophones in the borehole. Model accuracy would be improved by use of a large number of detectors, and also by incorporation of smoothness constraints which could be based on other log data from the borehole. Alternatively, a neural network approach could be used to automate the process of generating a permeability log from data measured in the borehole using a simpler 'look-up' method, and would be a fast method of doing this, something which may be important in practical well-logging situations. An adjoint method of inversion may be preferable to a neural-network approach however, as the latter would rely on a vast repository of model data including models with varying porosity, permeability, mudcake stiffness, borehole radii, layering etc to achieve an acceptable degree of accuracy. Optimisation of the various parameters involved in the model, including solver tolerances and time-stepping, along with the necessary alterations to allow the

code to run on many parallel processors could easily reduce the duration of the whole procedure, incorporating inversion calculations and forward modelling, to a few hours. Such an improvement in the performance of the method would make deployment in the field feasible, where it might be used for fast characterisation of reservoir formations.

Appendix A

Papers resulting from the work in this thesis

Saunders, J.H., Herwanger, J.V., Pain, C.C., Worthington, M.H. & de Oliveira, C.R.E., 2005. Constrained Resistivity Inversion Using Seismic Data, *Geophys. J. Int.*, published online Feb 28 2005.

Pain, C.C., Saunders, J.H., Worthington, M.H., Singer, J.M., Stuart-Bruges, W., Mason, G. & Goddard, A., 2005. A mixed finite element method for solving the poroelastic Biot equations with electrokinetic coupling, *Geophys. J. Int.*, **160**, 592-608.

Pain, C.C., Herwanger, J.V., Saunders, J.H., Worthington, M.H. & de Oliveira, C.R.E., 2003. Anisotropic resistivity inversion, *Inverse Problems*, **19**, 1081-1111.

Bibliography

Arfken, G. & Weber, H., 1995. *Mathematical Methods for Physicists*, Academic Press, 4th edition.

Armstrong, A.C.C. & Jackson, M.D., 2001. Management of Water Breakthrough Using Intelligent Well Technology, *Offshore Technology Conference*, 13284.

Astbury, S. & Worthington, M.H., 1986. The analysis and interpretation of full waveform sonic data. Part I: dominant phases and shear wave velocity, *First Break*, **4**, No.4, 7-16.

Beamish, D., 1999. Characteristics of near-surface electrokinetic coupling, *Geophys. J. Int.*, **137**, 231-242.

Beamish, D. & Peart, R.J., 1998. Electrokinetic geophysics - a review, *Terra Nova*, **10**, 48-55.

Bernabé, Y., 1998. Streaming potential in heterogeneous networks, *J. Geophys. Res.*, **103**, No.B9, 20827-20841.

Biot, M.A., 1956. Theory of propagation of elastic waves in a fluid-saturated porous solid. I. Low frequency range, *J. Acoust. Soc. Am.*, **28**, No.2, 168-178.

Biot, M.A., 1962. Mechanics of Deformation and Acoustic Propagation in Porous Media, *J. Appl. Phys.*, **33**, No.4, 1482-1498.

Biot, M.A. & Willis, D.G., 1957. The Elastic Coefficients of the Theory of Consolidation, *J. Appl. Mech.*, **24**, 594-601.

Bourbié, T., Coussy, O. & Zinszner, B., 1987. *Acoustics of Porous Media*, Gulf Publishing Co., Houston, Texas, 49-75.

Brie, A., Pampuri, F., Marsala, A.F. & Meazza, O., 1995. Shear Sonic Interpretation in Gas-Bearing Sands, SPE Annual Technical Conference and Exhibition, Dallas USA, Paper SPE 30595.

Brie, A., Endo, T., Johnson, D.L. & Pampuri, F., 2000. Quantitative Formation Permeability Evaluation from Stoneley Waves, *SPE Reservoir Eval. & Eng.*, **3**, No.2, 109-117.

Burns, D.R., 1991. Predicting Relative and Absolute Variations of in-situ Permeability from Full-Waveform Acoustic Logs, *The Log Analyst*, May-June 1991, 246-255.

Bryant, I.D., Chen, M.-Y., Raghuraman, B., Schroeder, R., Supp, M., Navarro, J., Raw, I., Smith, J. & Scraggs, M., 2002. Real-Time Monitoring and Control of Water Influx to a Horizontal Well Using Advanced Completion Equipped with Permanent Sensors, *SPE Annual Technical Conference*, San Antonio, Texas, SPE 77522.

Chapman, C.H. & Pratt, R.G., 1992. Traveltime tomography in anisotropic media - I. Theory, *Geophys. J. Int.*, **109**, 1-19.

Cheng, C.H. & Toksöz, M.N., 1981. Elastic wave propagation in the fluid-filled borehole and synthetic acoustic logs, *Geophysics*, **46**, No.7, 1042-1053.

Cheng, C.H., Toksöz, M.N. & Willis, M.E., 1982. Determination of In Situ Attenuation From Full Waveform Acoustic Logs, *J. Geophys. Res.*, **87**, No.B7, 5477-5485.

Cheng, C.H., Jinzhong, Z. & Burns, D.R., 1987. Effects of in-situ permeability on the propagation of Stoneley (tube) waves in a borehole, *Geophysics*, **52**, No.9, 1279-1289.

Donea, J. & Huerta, A., 2003. *Finite Element Methods for Flow Problems*, John Wiley & Sons, Chichester, UK.

Fagerlund, F. & Heinson, G., 2003. Detecting subsurface groundwater flow in fractured rock using self-potential (SP) methods, *Environmental Geology*, **43**, 782-794.

Fitterman, D.V., 1978. Electrokinetic and magnetic anomalies associated with dilatant regions in a layered earth, *J. Geophys. Res.*, **83**, 5923-5928.

Garambois, S. & Dietrich, M., 2001. Seismoelectric wave conversions in porous media: Field measurements and transfer function analysis, *Geophysics*, **66**, No.5, 1417-1430.

Golub, G.H. & van Loan, C.F., 1989. *Matrix Computations*, 2nd Edition, John Hopkins University Press, Baltimore, MD.

Gresho, P.M. & Sani, R.L., 1998. *Incompressible Flow and the Finite Element Method, Advection-Diffusion and Isothermal Laminar Flow*, John Wiley & Sons Ltd, Chichester, UK.

Guichet, X., Jouniaux, L. & Pozzi, J-P., 2003. Streaming potential of a sand column in partial saturation conditions, *J. Geophys. Res*, **108**, No.B3, 2141, 10.1029/2001JB001517.

Haartsen, M.W. & Pride, S.R., 1997. Electroseismic waves from point sources in layered media, *J. Geophys. Res.*, **201**, No.B11, 24745-24769.

Haartsen, M.W., Dong, W. & Toksöz, M.N., 1998. Dynamic streaming currents from seismic point sources in homogeneous poroelastic media, *Geophys. J. Int*, **132**, 256-274.

Haber, E. & Oldenburg, D., 1997. Joint inversion: a structural approach, *Inverse Problems*, **13**, 63-77.

Hämmann, M., Maurer, H.R., Green, A.G. & Horstmeyer, H., 1997. Self-Potential Image Reconstruction: Capabilities and Limitations, *Journal of Environmental and Engineering Geophysics*, Vol.2, issue 1, 21-35.

Hampson, G.J., 2000. Discontinuity surfaces, clinoforms, and facies architecture in a wave-dominated, shoreface-shelf parasequence, *J. Sedimentary Res.*, **70**, No.2, 325-340.

Herwanger, J.V., 2001. *Seismic and Electric Crosshole Tomography for Fracture Detection and Characterization*, PhD thesis, Imperial College of Science, Technology & Medicine, London, UK.

Herwanger, J.V., Worthington, M.H., Lubbe, R., Binley, A. & Khazanehdari, J., 2004. A comparison of crosshole electrical and seismic data in fractured rock, *Geophysical Prospecting*, **52**, No.2, 109-121.

Herwanger, J.V., Pain, C.C., Binley, A., de Oliveira, C.R.E. & Worthington, M.H., 2004. Anisotropic Resistivity Tomography, *Geophys. J. Int*, **158**, 409-425.

Jackson, P.S., Earl, S.J. & Reece, G.J., 2001. 3D resistivity inversion using 2D measurements of the electric field, *Geophysical Prospecting*, **49**, 26-39.

Jennings, A. & McKeown, J., 1992. *Matrix Computation*, John Wiley and Sons, Chichester, 2nd edition.

Jiang, Y.G., Shan, F.K., Jin, H.M., Zhou, L.W. & Sheng, P., 1998. A method for measuring electrokinetic coefficients of porous media and its potential application in hydrocarbon exploration, *Geophys. Res. Lett.*, **25**, No.10, 1581-1584.

Jouniaux, L. & Pozzi, J-P., 1995. Permeability dependence of streaming potential in rocks for various fluid conductivities, *Geophys. Res. Lett.*, **22**, No.4, 485-488.

Jouniaux, L., Bernard, M.L., Pozzi, J.P. & Zamora, M., 2000. Electrokinetic in Rocks: Laboratory Measurements in Sandstone and Volcanic Samples, *Physics and Chemistry of the Earth (A)*, **25**, No.4, 329-332.

Jupp, D. & Vozoff, K., 1975. Stable iterative methods for the inversion of geophysical data, *Geophys. J. R. Astr. Soc.*, **42**, 957-976.

Kaipio, J.P., Kolehmainen, V., Vauhkonen, M. & Somersalo, E., 1999. Inverse problems with structural prior information, *Inverse Problems*, **15**, 713-729.

Kennett, B.L.N., Sambridge, M.S. & Williamson, P.R., 1988. Subspace methods for large inverse problems with multiple parameter classes, *Geophys. J. Int.*, **94**, 237-247.

Leary, P.C. & Al-Kindy, F., 2002. Power-law scaling of spatially correlated porosity and log(permeability) sequences from north-central North Sea Brae oilfield well core, *Geophys. J. Int.*, **148**, 426-442.

LeVeque, R.J., 2002. *Finite Volume Methods for Hyperbolic Problems*, CUP, Cambridge, UK.

Li, S.X., Pengra, D.B. & Wong, P.Z., 1995. Onsager's reciprocal relation and the hydraulic permeability of porous media, *Physical Review E*, **51**, No.6, 5748-5751.

Lines, L.R., Schultz, A.K. & Treitel, S., 1988. Cooperative inversion of geophysical data, *Geophysics*, **53**, No.1, 8-20.

Liu, H-L & Johnson, D.L., 1997. Effects of an elastic membrane on tube wave in permeable formations, *J. Acoust. Soc. Am.*, **101**, No.6, 3322-3329.

Marquis, G., Darnet, M., Sailhac, P., Singh, A.K. & Gerard, A., 2002. Surface electric variations induced by deep hydraulic stimulation: an example from the Soultz HDR site, *Geophys. Res. Lett.*, **29**, No.14, 1662.

Maurer, H. & Holliger, K., 1998. Stochastic regularization: Smoothness or similarity?, *Geophys. Res. Lett.*, **25**, No.15, 2889-2892.

Meju, M.A., Gallardo, L.A. & Mohamed, A.K., 2003. Evidence for correlation of electrical resistivity and seismic velocity in heterogeneous near-surface materials, *Geophy. Res. Lett.*, **30**, No.7, 1373, doi:10.1029/2002GL016048, 2003.

Merkler, G.P., Militzer, H., Hötzl, H., Armbruster, H. & Brauns, J. (Eds), *Detection of Subsurface Flow Phenomena, Lecture Notes in Earth Sciences, 27*, Springer-Verlag.

Mikhailov, O.V., Haartsen, M.W. & Toksöz, M.N., 1997. Electroseismic investigation of the shallow subsurface: Field measurements and numerical modeling, *Geophysics*, **62**, No.1, 97-105.

Mikhailov, O.V., Queen, J. & Toksöz, M.N., 2000. Using borehole electroseismic measurements to detect and characterize fractured (permeable) zones, *Geophysics*, **65**, No.4, 1098-1112.

Musil, M., Maurer, H.R. & Green, A.G., 2003. Discrete tomography and joint inversion for loosely connected or unconnected physical properties: application to crosshole seismic and georadar data sets, *Geophys. J. Int*, **153**, 389-402.

Neev, J. & Yeatts, F.R., 1989. Electrokinetic effects in fluid-saturated poroelastic media, *Physical Review B*, **40**, No.13, 9135-9141.

Nygaard, E., Aamand, J., Jacobsen, P.R., Adar, E., Williams, A., Bloomfield, J., Reichert, B., Witthüser, K. & Nativ, R., 1998. Contaminant transport, monitoring technique, and remediation strategies in cross European

fractured chalk: First Annual Progress Report, Project funded and co-funded by the European Commission, contract ENV4-CT97-0441, *www.fracflow.dk/Results/annual-rep-98.pdf*

Paillet, F.L., 1991b. Qualitative and Quantative Interpretation of Fracture Permeability Using Acoustic Full-Waveform Logs, *The Log Analyst*, May-June 1991, 256-270.

Pain, C.C., Mansoorzadeh, S., de Oliveira, C.R.E. & Goddard, A.J.H., 2000. Numerical Modelling of Gas-Solid fluidised beds using the two-fluid approach, *International Journal of Numerical Methods in Fluids*, **36**, 91-124.

Pain, C.C., Herwanger, J.V., Worthington, M.H. & de Oliveira, C.R.E., 2002. Effective multidimensional resistivity inversion using finite-element techniques, *Geophys. J. Int.*, **151**, No.3. 710-728.

Pain, C.C., Herwanger, J.V., Saunders, J.H., Worthington, M.H. & de Oliveira, C.R.E., 2003. Anisotropic resistivity inversion, *Inverse Problems*, **19**, 1081-1111.

Pain, C.C., Saunders, J.H., Worthington, M.H., Singer, J.M., Stuart-Bruges, W., Mason, G. & Goddard, A., 2005. A mixed finite element method for solving the poroelastic Biot equations with electrokinetic coupling, *Geophys. J. Int.*, **??**, No.?, ???-???.

Park, S.K. & Van, G.P., 1991. Inversion of pole-pole data for 3D-resistivity structure beneath arrays of electrodes, *Geophysics*, **56**, No.7, 951-960.

Pinheiro, P.A.T., Loh, W.W. & Dickin, F.J., 1997. Smoothness-constrained inversion for two-dimensional electrical resistance tomography, *Measurement Science and Technology*, **8**, 293-302.

Pratt, R.G. & Chapman, C.H., 1992. Traveltime Tomography in anisotropic media - II. Application, *Geophys. J. Int.*, **109**, 20-37.

Pride, S., 1994. Governing equations for the coupled electromagnetics and acoustics of porous media, *Physical Review B*, **50**, No.21, 15678-15696.

Pride, S.R. & Morgan, F.R., 1991. Electrokinetic dissipation induced by seismic waves, *Geophys.*, **56**, No.7, 914-925.

Raymer, L.L., Hunt, E.R. & Gardner, J.S., 1980. An improved sonic transit time to porosity transform, 21st SPWLA Annual Meeting, 1-13.

Revil, A. & Cerepi, A., 2004. Streaming potentials in two-phase flow conditions, *Geophys. Res. Lett.*, **31**, L.11605, 10.1029/2004GL020140.

Revil, A., Pezard, P.A. & Glover, P.W.J., 1999. Streaming potential in porous media 1. Theory of the zeta potential, *J. Geophys. Res.*, **104**, No.B9, 20021-20031.

Revil, A., Schwaeger, H., Cathles III, L.M. & Manhardt, P.D., 1999. Streaming potential in porous media 2. Theory and application to geothermal systems, *J. Geophys. Res.*, **104**, No.B9, 20033-20048.

Revil, A., Saracco, G. & Labazuy, P., 2003. The volcano-electric effect, *J. Geophys. Res.*, **108**, No.B5, art.2251.

Revil, A., Naudet, V. & Meunier, J.D., 2004. The hydroelectric problem of porous rocks: inversion of the position of the water table from self-potential data, *Geophys. J. Int.*, **159**, 435-444.

Reynolds, J.M., 1997. *An introduction to applied and environmental geophysics*, John Wiley & Sons Ltd, Chichester, England.

Rosenbaum, J.H., 1974. Synthetic microseismograms: Logging in porous formations, *Geophysics*, **39**, No.1, 14-32.

Saenger, E.H., Gold, N. & Shapiro, S.A., 2000. Modeling the propagation of elastic waves using a modified finite-difference grid, *Wave Motion*, **31**, 77-92.

Saunders, J.H., Herwanger, J.V., Pain, C.C., Worthington, M.H. & de Oliveira, C.R.E., 2004. Constrained Resistivity Inversion Using Seismic Data, *Geophys. J. Int.*, in press.

Schiavone, D. & Quarto, R., 1984. Self-potential prospecting in the study of water movements, *Geoexploration*, **22**, 47-58.

Semenov, A.S., 1980. *Elektrorazvedka metodom Estectvennogo Elektricheskogo Polya*, Nedra, Leningrad, Russia.

Sheriff, R.E. & Geldart, L.P., 1982. *Exploration seismology, Volume 1*, Cambridge University Press, Trumpington Street, Cambridge CB2 1RP, UK.

Shima, H., 1992. 2-D and 3-D resistivity image reconstruction using crosshole data, *Geophysics*, **57**, No.10, 1270-1281.

Sprunt, E.S., Mercer, T.B. & Djabbarah, N.F., 1994. Streaming potential from multiphase flow, *Geophysics*, **59**, No.5, 707-711.

Stekl, I. & Pratt, R.G., 1998. Accurate visco-elastic modeling by frequency-domain finite differences, using rotated operators, *Geophysics*, **63**, 1779-1794.

Tang, X.M., Cheng, C.H. & Toksöz, M.N., 1991. Dynamic permeability and borehole Stoneley waves: A simplified Biot-Rosenbaum model, *J. Acoust. Soc. Am.*, **90**, No.3, 1632-1646.

Tang, X.M., 1994. Effects of mudcake on the measurement of fluid flow properties using borehole acoustic waves, *SEG Expanded Abstracts*, 64th Annual Meeting, Los Angeles, p.78, BG 3.4.

Telford, W.M., Geldart, L.P. & Sheriff, R.E., 1990. *Applied Geophysics, Second Edition*, Cambridge University Press, Trumpington Street, Cambridge CB2 1RP, UK.

Thompson, A.H. & Gist, G.A., 1993. Geophysical applications of electrokinetic conversion, *The Leading Edge*, **12**, Iss.12, 1169-1173.

Thomsen, L., 1986. Weak Elastic Anisotropy, *Geophysics*, **51**, No.10, 1954-1966.

Tsang, L. & Rader, D., 1979. Numerical evaluation of the transient acoustic waveform due to a point source in a fluid-filled borehole, *Geophysics*, **44**, No.10, 1706-1720.

Vasco, D.W., Peterson, J.E. & Majer, E.L., 1998. Resolving seismic anisotropy: Sparse matrix methods for geophysical inverse problems, *Geophysics*, **63**, No.3, 970-983.

Winkler, K.W., Liu, H-L. & Johnson, D.L., 1989. Permeability and borehole Stoneley waves: Comparison between experiment and theory, *Geophysics*, **54**, No.1, 66-75.

Wurmstich, B. & Morgan, F.D., 1994. Modeling of streaming potential responses caused by oil well pumping, *Geophysics*, **59**, No.1, 46-56.

Wyllie, M.R.J., Gregroy, A.R. & Gardner, L.W., 1956. Elastic wave velocities in heterogeneous and porous media, *Geophysics*, **21**, 41-70.

Zhang, J. & Morgan, F.D., 1997. Joint Seismic and Electrical Tomography, Proceedings of the SAGEEP 1997, Reno, Nevada.

Zhang, J., Mackie, R.L. & Madden, T.R., 1995. 3-D resistivity forward modeling and inversion using conjugate gradients, *Geophysics*, **60**, No.5, 1313-1325.

Zhu, Z., Haartsen, M.W. & Toksöz, M.N., 1999. Experimental studies of electrokinetic conversions in fluid-saturated borehole models, *Geophysics*, **64**, No.5, 1349-1356.

Zienkiewicz, O.C. & Taylor, R.L., 2000. *The Finite Element Method: Volumes 1-3*, Butterworth-Heinemann 5th edition, Oxford, UK.